NAVAL POSTGRADUATE SCHOOL

MONTEREY, CALIFORNIA

THESIS

ANALYZING UUV HULL CROSS-SECTIONS FOR MINIMIZING WAVE LOADS WHEN OPERATING NEAR SURFACE

by

Travis M. Turner

June 2018

Thesis Advisor: Joseph Klamo
Second Reader: Clifford A. Whitcomb

Approved for public release. Distribution is unlimited.

THIS PAGE INTENTIONALLY LEFT BLANK

REPORT DOCUMENTATION PAGE			*Form Approved OMB No. 0704-0188*

1. AGENCY USE ONLY *(Leave blank)*	**2. REPORT DATE** June 2018	**3. REPORT TYPE AND DATES COVERED** Master's thesis

4. TITLE AND SUBTITLE ANALYZING UUV HULL CROSS-SECTIONS FOR MINIMIZING WAVE LOADS WHEN OPERATING NEAR SURFACE	**5. FUNDING NUMBERS** R4L9H
6. AUTHOR(S) Travis M. Turner	
7. PERFORMING ORGANIZATION NAME(S) AND ADDRESS(ES) Naval Postgraduate School Monterey, CA 93943-5000	**8. PERFORMING ORGANIZATION REPORT NUMBER**
9. SPONSORING / MONITORING AGENCY NAME(S) AND ADDRESS(ES) N/A	**10. SPONSORING / MONITORING AGENCY REPORT NUMBER**

11. SUPPLEMENTARY NOTES The views expressed in this thesis are those of the author and do not reflect the official policy or position of the Department of Defense or the U.S. Government.

12a. DISTRIBUTION / AVAILABILITY STATEMENT Approved for public release. Distribution is unlimited.	**12b. DISTRIBUTION CODE** A

13. ABSTRACT (maximum 200 words)

This research considers square and rectangular cross-sectional shapes for unmanned underwater vehicle (UUV) parallel mid-bodies as a means for reducing wave-induced loads when operating near the surface. The inquiry is addressed through experimental model testing in a monochromatic wave environment with a circular cross-section model as a reference. The results suggest there is a loading difference between rectangular and circular models but little difference between circular and square cross-sections. An exponentially decaying depth dependency is observed for near-surface depths, which enables extrapolation of predicted forces and moments to other operating depths not tested. Reducing the depth further such that the distance between the surface and the vehicle center-line is less than the hull diameter exhibits a somewhat different behavior. This identifies a very-near-surface region where current modeling is inadequate. Non-circular hull designs can reduce wave-induced loads and effectively reduce operating depths for underwater vehicles. The findings support further research to determine optimal design points and to evaluate the effects of different designs on system architectures.

14. SUBJECT TERMS UUV, wave loads, hull, hull forms	**15. NUMBER OF PAGES** 135
	16. PRICE CODE

17. SECURITY CLASSIFICATION OF REPORT	**18. SECURITY CLASSIFICATION OF THIS PAGE**	**19. SECURITY CLASSIFICATION OF ABSTRACT**	**20. LIMITATION OF ABSTRACT**
Unclassified	Unclassified	Unclassified	UU

NSN 7540-01-280-5500 Standard Form 298 (Rev. 2-89) Prescribed by ANSI Std. 239-18

THIS PAGE INTENTIONALLY LEFT BLANK

Approved for public release. Distribution is unlimited.

ANALYZING UUV HULL CROSS-SECTIONS FOR MINIMIZING WAVE LOADS WHEN OPERATING NEAR SURFACE

Travis M. Turner
Lieutenant, United States Navy
BS, United States Naval Academy, 2011

Submitted in partial fulfillment of the
requirements for the degree of

MASTER OF SCIENCE IN SYSTEMS ENGINEERING

from the

NAVAL POSTGRADUATE SCHOOL
June 2018

Approved by: Joseph Klamo
Advisor

Clifford A. Whitcomb
Second Reader

Ronald E. Giachetti
Chair, Department of Systems Engineering

THIS PAGE INTENTIONALLY LEFT BLANK

ABSTRACT

This research considers square and rectangular cross-sectional shapes for unmanned underwater vehicle (UUV) parallel mid-bodies as a means for reducing wave-induced loads when operating near the surface. The inquiry is addressed through experimental model testing in a monochromatic wave environment with a circular cross-section model as a reference. The results suggest there is a loading difference between rectangular and circular models but little difference between circular and square cross-sections. An exponentially decaying depth dependency is observed for near-surface depths, which enables extrapolation of predicted forces and moments to other operating depths not tested. Reducing the depth further such that the distance between the surface and the vehicle center-line is less than the hull diameter exhibits a somewhat different behavior. This identifies a very-near-surface region where current modeling is inadequate. Non-circular hull designs can reduce wave-induced loads and effectively reduce operating depths for underwater vehicles. The findings support further research to determine optimal design points and to evaluate the effects of different designs on system architectures.

THIS PAGE INTENTIONALLY LEFT BLANK

Table of Contents

THIS PAGE INTENTIONALLY LEFT BLANK

List of Figures

List of Tables

THIS PAGE INTENTIONALLY LEFT BLANK

Executive Summary

As underwater vehicles operate near the surface, they are subjected to wave-induced loads that affect seakeeping and operation. These forces and moments decrease with depth, providing the obvious solution of operating deep enough to avoid the effects. This practice, however, limits the available operating areas for submerged vehicles and possibly precludes effective littoral operations. Expanded understanding of the effects in these shallow environments supports development of underwater vehicles capable of near-surface operation. This research considers the effects of depth and hull cross-sectional geometry on the loads experienced by shallowly-operating underwater vehicles.

There is a clear relationship between the cross-sectional geometry of a vehicle and the wave-induced loads it experiences. The differences are greatest when the horizontal dimension of the cross-section is larger than the vertical one. Measured forces and moments for this condition are significantly large compared to other geometries tested. Conversely, when the dimensional ratio is inverted the experienced loads are somewhat less than those experienced by a circular vehicle. A square cross-section is also considered which, like a circle, has a unity dimensional ratio. No significant difference is observed between circular and square geometries of nearly-identical cross-sectional areas. This suggests that the two can be used interchangeably which may provide new design options for launch and recovery systems, component selection and placement within the vehicle, storage, and other myriad system considerations.

A relationship also exists between center-line depth and the observed loading amplitudes. Theory suggests there is an exponential decay relationship between the depth and the force and moment magnitudes (Cummins 1961). This assertion is validated in this research for near-surface depths where the center-line position is at least 1.5 times as deep as the effective diameter of the hull. The data observed suggests that the exponential-decay relationship does not hold when the vehicle is very-near-surface at depth ratios one or less.

Experimental testing is used to evaluate different cross-sectional geometries and depths. Testing is conducted in a tow tank with a wedge-type wave maker. The test models are held stationary in a wave environment and the forces and moments are measured. Geometries

considered are circular, square, and horizontally- and vertically-oriented rectangles. All models have nearly-identical cross-sectional areas with targets of 16 in^2 and varying less than one percent from that value. Each has hemi-spherical or cylindrical ends with a full length of 45 inches. Depths considered are characteristic depth ratios between the center-line depth and the diameter for a circular model. The ratios observed are 1.0, 1.5, 2.0, and 3.0. A wide range of wave frequencies are considered, but the wave environments are all monochromatic with wave heights of two inches.

Force and moment data is collected for one-minute duration as the models are subjected to the wave environments. This raw data is analyzed to derive the force and moment amplitudes. Longitudinal and vertical forces and the pitching moments are the primary values of interest in this research. Appropriate corrections are made for the test setup, accounting for the test rig itself as well as the dislocation between the model center of buoyancy and the load cell used to measure the forces and moments. The summary data is then considered to evaluate the effects of geometry and depth on the vehicle.

The theoretical foundation for considering submerged bodies of revolution is detailed in Cummins' work. However, the theory does not adequately address the loading effects for other hull geometries. This theoretical base provides a means for considering non-circular cross-sectional geometries as they compare to a circle. The data is fit to the theoretical expressions for vertical forces and pitching moments to enable comparison between geometries.

The data suggest there is no significant difference between vehicles of circular or square cross-sectional geometries. Differences are noted among all geometries and the results appear to be dependent on the dimensional ratio of the cross-section. There is opportunity to further consider these effects beyond the three ratios evaluated here. Analysis of the depth dependency suggests that exponential decay is an accurate model for the relationship between depth and load amplitudes for near-surface operation. This suggests that a given model design may not need testing at a full range of operating depths, but can be tested at a single depth and the behavior at other depths extrapolated. The decay relationship does not hold for very-near-surface depths. While this research identifies a departure from the theoretical model, more testing is needed to fully understand the behavior in this region and determine the transition point between near-surface and very-near-surface depths.

This research identifies a relationship between hull geometry and wave-induced load amplitudes. Several dimensional ratios are considered, but there is room for detailed exploration of how the loads change with the ratio. The work also suggests a depth dependency for prediction of wave-induced loading beyond the previously-accepted theory. This theory appears to hold in most cases, but further study is needed to characterize very-shallow operations. Testing under more-complex wave environments and conditions is also needed to better appreciate the range of effects in an underwater vehicle's proposed operating environment. These findings are a foundation for future research and development. Greater consideration should be made for non-circular hull geometries as a means to reduce wave-induced loading.

Reference

Cummins, W.E. 1961. *Preliminary Note on the Surface Suction Force Acting on a Submarine Hovering Under Waves*. Technical Report 033445. West Bethesda, MD: David Taylor Model Basin.

THIS PAGE INTENTIONALLY LEFT BLANK

Acknowledgments

Special thanks to Professor Klamo for his mentorship and guidance through this work.

Thanks to Professor Whitcomb, who was kind enough to be my second reader.

Dan Sakoda was extremely helpful with manufacturing test-model components. Thank you for your time and assistance.

John Mobley offered his time and expertise to improve the test setup and enable this research.

Finally, a special thanks to my wife and family for putting up with me during this process.

THIS PAGE INTENTIONALLY LEFT BLANK

CHAPTER 1:
Introduction and Background

1.1 Chapter Introduction

Chapter 1 provides an overview for this thesis. A discussion of the problem provides an overview of the topic which this work aims to address. Previous work in the field is presented to give context for the research. The research objectives are stated and the methodology for achieving those objectives is described.

1.2 Problem Introduction

Unmanned underwater vehicles (UUVs) operate in a wide variety of wave conditions and depths. The wave motion on the surface causes the water below to move in kind. The subsequent water motion is greatest at the surface and decreases with depth. Consequently, as a vehicle approaches the surface, the waves invariably have an increasing effect upon it. The motion of the waves creates forces and moments that are experienced by the vehicle. If there is no compensation provided for the loads, the vehicle will undergo undesirable motions. To avoid these wave-induced forces, it logically follows that many underwater vehicles operate at deeper depths where the forces are minimal or non-existent.

An example of a vehicle which operates below the wave effects is the Mk 18 Mod 1 Swordfish UUV, also known as the Remus 100, used by the United States Navy. Its typical operating depth is about ten to forty feet (Jane's by IHS Markit 2018). The cross-sectional diameter of the vehicle, however, is only 0.19 meters, or about 0.623 feet (Jane's by IHS Markit 2018). This means the operating depth is at least sixteen times the diameter of the vehicle. A minimum depth of 10 feet restricts the usable area of the vehicle, especially in littoral environments. These minimum depths affect the operating concepts as a result. However, by developing a greater understanding of how wave-induced loading affects underwater vehicles, they can be designed such that they either minimize the effects or compensate for them.

Operating at increasingly deeper depths is not always possible. In shallow areas or littorals,

the depth of the water may not accommodate deeper operation. Shallow operating depths are also desirable for certain operational concepts. There are follow-on implications for the UUV system architecture, especially when considering how it interacts with other systems within a larger system-of-systems framework. Some specific examples of architectural items are propulsion types, communications methods, or sensor selections. Understanding these wave-induced loads enables better decision-making for the system requirements and architectural design. This has the potential to not only improve overall performance, but to inform early, system-level design decisions.

1.3 Previous Work

Numerous theoretical treatments of the problem have been offered, as well as experimental efforts. However, many of the theoretical approaches make idealized assumptions. There has also been a limited effort to experimentally demonstrate and prove these theories.

Cummins conducted extensive work on modeling the first-order forces and moments experienced by submerged bodies. Building off work done by Lagally, he derived the first-order forces and moments for a submerged body in an arbitrary, inviscid potential stream (Cummins 1953). He later adapted his work to the specific case of a slender body of revolution (Cummins 1954b). Cummins notes that his derived work for the body of revolution "may be used for other slender bodies in which the cross sections depart somewhat from circular, with the expectation that the answer will at least be correct in order of magnitude" (Cummins 1954b, 1). In a later analysis, he compares his theory to an experiment conducted at the Stevens Institute on the GUPPY Type 1 submarine (Cummins 1954a, 1). He notes that the model hull form in this experiment was "quite complex" which "precluded any theoretical treatment with methods available" (Cummins 1954a, 1). Cummins observes that the theoretical value and the experimental results for the vertical force were "relatively good" in comparison, but that "the computed pitching moment differed seriously from the experimental value" (Cummins 1954a, 1). The assumptions used in the theoretical derivation limit the applicability of the experiments. Cummins notes that his method should hold for nearly-circular cross-sections, but there is not enough detail regarding the test model to identify whether or not this experiment meets that condition. Cummins identifies and discusses a suction force experienced by submerged bodies, specifically submarines in this case, operating near the wave surface (Cummins 1961). As with much of Cummins' other

work, this is primarily theoretical work and it is not apparent whether he conducted an experimental verification. The breadth of Cummins' work provides a mathematically rigorous reference frame for considering the first-order wave-induced forces and moments on a submerged body.

Pinkster analyzed the effects of waves on semi-submersible structures. He derived theoretical expressions for the second order forces and moments acting on a body, assuming inviscid and irrotational flow (Pinkster 1981, 10–11). Beyond a theoretical treatment, Pinkster also sought to validate his models by conducting tests in a model basin. There is agreement between the experimental data and his predictive models. This suggests that both horizontal and vertical forces can be "reasonably well predicted using potential theory" (Pinkster 1981, 14).

Work conducted by Khalil measured the forces experienced by submerged cylinders subjected to surface waves (Khalil 2001) That experiment considered a circular cross-section and a square cross-section at two wavelengths and a variety of depths (Khalil 2001). The models were exposed to beam waves, that is to say perpendicular to the vehicle length. Khalil's work suggests that there is a difference between cylinders of circular and square cross-sectional geometries.

Alvarez, Bertram, and Gualdesi sought to optimize the hull form for an underwater vehicle operating near the surface. Their efforts were focused on mathematically minimizing the drag force while maintaining a constant volume (Alvarez, Bertram, and Gualdesi 2009, 105). From the perspective of lateral forces, their optimized hull design strongly suggests that the cylindrical design is sub-optimal. They did not measure vertical forces due to limitations in the test setup, however, so it is unclear what the effects are of the optimized hull on the vertical loads. While the nature of the work was limited in scope, their results make a reasonable argument that the cylindrical hull can be improved upon.

Research conducted by Ananthakrishnan and Zhang pursued the effects of sea floor and surface waves on underwater vehicles (Ananthakrishnan and Zhang 1998, 1059). They offer a theoretical treatment of the interaction forces, considering the effects of both viscous and inviscid flows. Their model showed that the flow velocity and resulting forces were dependent on the depth of the vehicle. At shallower depths, the waves had a greater influence on the flow about the hull (Ananthakrishnan and Zhang 1998, 1062–1063). This work,

however, only models the effect on a specific vehicle: the Gertler#4154 (Ananthakrishnan and Zhang 1998, 1061). Evaluating a geometrically-simplified vehicle would have allowed for comparison to other works like those of Cummins, Khalil, or Lee and Newman. Regardless, the models strongly suggest a relationship between the proximity to the boundary layers, either sea floor or wave surface, and the experienced forces on the body.

Work by Lee and Newman derives the mean vertical force and moment for a slender body (Lee and Newman 1971). In contrast to Cummins' work in which he uses the Lagally theorem to approach the first order forces, Lee and Newman used Kochin's functions to describe the forces (Lee and Newman 1971, 232). They were able to describe the first- and second-order forces and moments for a slender body with an "arbitrary sectional form" (Lee and Newman 1971, 232). They also considered the theoretical effects of cross-sectional geometry, but only analyzed these effects for deeply-submerged bodies (Lee and Newman 1971). The ratio between cross-sectional dimensions, however, must be close to one (Lee and Newman 1971, 242). This implies that their predictions only hold for nearly-circular cross-sectional shapes like ellipses or rectangles with closely-related dimensions. While they offer tables for predicting the effects of these geometric deviations, they are simply theoretical approximations. They claim to be "exact for elliptical sections, and they are in error by less than 20 percent for the rectangle and finned circle" (Lee and Newman 1971, 242). This appears to be a purely theoretical treatment, however, based only on the ratio of "the relative difference between the body and an 'equivalent' body of revolution having the same sectional-area distribution" (Lee and Newman 1971, 241–242). Their theoretical values suggest that shapes with horizontal-to-vertical dimension ratios greater than one should experience larger loads than when the ratio is one or less.

1.4 Research Objective

There is still an opportunity, however, to further consider Cummins' work and to experimentally validate his claims, particularly those regarding the effects of geometry. Khalil's research serves as a comparison point for further work and provides an experimental example to support the idea that geometry influences the induced loads. Experimental analysis of non-circular geometries would also be beneficial for either supporting or disproving the theoretical results of Lee and Newman.

The first objective of this research effort is to validate the theory for first-order loads on a body of revolution. The second goal is to validate the effects of depth on first-order loads. The final objective is to explore the effects of hull cross-section using non-body of revolution geometries. Increased understanding of this design space will facilitate better-informed trade-off analysis. It will also improve the initial design considerations and requirements determination for underwater vehicles. By minimizing the wave-induced loads experienced by the UUV, the minimum operating depths can be reduced. If the loads are not reduced by changing the hull-form, then they can possibly be predicted and minimized using control systems. In the event that there is little difference in the experienced loads between different shapes, it is possible that some shapes might be designed with greater efficiency for component placement or other packaging considerations. Minimizing wasted space inside a vehicle results in more propulsion and payload equipment. A reduced operating depth will increase the available operating area, change system architectures and operating concepts, and overall improve the capabilities of underwater vehicles.

1.5 Research Methodology

The research objectives are addressed by testing models with different cross-sections at varying depths and single wave conditions. A circular model is used as a reference and point of comparison. Non-circular shapes are subsequently compared against it. These geometries are the variables in the experiment. In all cases, the cross-sectional areas are nearly equal. The models also all have the same lengths so as to achieve nearly identical internal volumes. The length is set to achieve a length to diameter ratio of 10 for the circular hull-form. This ratio is similar to that of the Mk 18 Mod 1 mentioned previously, which has a ratio between 8.4 and 9.4 depending on the model (Jane's by IHS Markit 2018). This supports comparison of the different cross-sectional shapes with each providing similar internal volume.

1.6 Chapter Summary

This chapter discussed the effects of wave-induced loads on UUVs and notable previous works on the subject. As mentioned, there are system-level implications for these forces. The system's response to the loads affects the potential system architectures and operating

concepts. This thesis intends to increase the community's understanding of this decision space to improve system design.

CHAPTER 2:
Theory

2.1 Chapter Introduction

Chapter 2 discusses the theory relevant to the research. The governing principles and expressions are presented and described as they relate to this work.

2.2 Wave Motion

The operating environment of most UUVs is subject to the effects of surface waves, especially for those operating near the surface. An exception to this is for deep-submergence vehicles which move below the influence of the surface waves. As will be discussed, there is a dependence between the depth and the severity of surface wave effects on a submerged body. A method of avoiding these effects is to operate well-below the surface. This practice, however, can severely limit the potential operating environment of a system.

Sea waves appear irregular and are constantly changing (Lewis 1989, 3). The traditional approach is to assume the sea surface is modeled as a complex environment of many regular waves, each with its own frequency and height (Lewis 1989). This means there are many single-frequency waves constructively- and destructively-interfering within the environment. A common method of modeling the wave surface is to consider it as a oscillatory function with a single mean amplitude (Lewis 1989, 6–8).

The waves used in this research are monochromatic in nature, meaning they are of a single wave height and a single wavelength or frequency. A large set of frequencies are tested, but each is tested individually and not as a composite waveform. This allows each frequency to be evaluated independently. An example of a monochromatic wave is shown in Figure 2.1. The wave height is the distance extending between the crest and trough, indicated by the red dashed line. The wave amplitude extends from the middle position to the crest or trough, shown by the black dashed-dotted line. The wave period is the duration for one full wave cycle as represented by the magenta dotted line in the figure. Frequency is the inverse

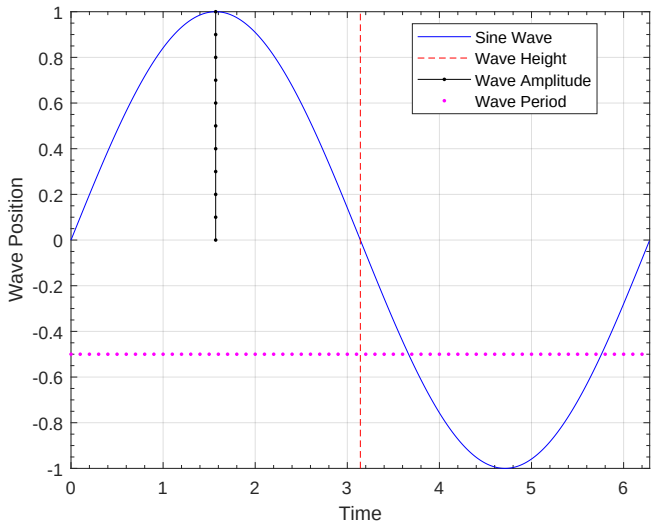

Figure 2.1. Sine Wave Cycle through One Period to Illustrate Wave Components

of the period T as shown in Equation 2.1:

$$f = \frac{1}{T}. \tag{2.1}$$

Waves acting on a surface due to a disturbance are considered dispersive. The wave environment is made of many superimposed waves with differing frequencies and velocities. According to Kundu and Cohen, these many-present wavelengths separate and disperse, resulting in a smoother wave profile with a single, dominant frequency (Kundu and Cohen 2007, 242). For a continually-driven wave train, it is expected that the initial low-frequency components will settle and the remaining wave form will resemble the driven frequency.

For dispersion waves, the first-order relationship between natural frequency ω and wave number k is described by Equation 2.2 (Kundu and Cohen 2007, 223):

$$\omega^2 = gk \tanh(kH). \tag{2.2}$$

The expression in Equation 2.2 covers waves in any water depth. The mean water depth

is represented by H which influences the particle motion according to the wavelength. Equation 2.2 correlates the wave frequency and the wave number, driven by wavelength, by accounting for the wave velocity and the depth of the medium. With this equation, the frequency can be determined according to the wave number and water depth.

The first-order relationship, however, does not account for the amplitude of the surface wave. The third-order dispersion relationship accounts for the effects of wave amplitude and provides a better calculation for the wavelength. The deep water limit form of the relationship is provided by Tucker and Pitt (Tucker and Pitt 2001, 394). The expression simplifies to

$$\omega^2 = gk\left[1 + (kA)^2\right] \tag{2.3}$$

where A is the wave amplitude. This expression captures the effects of wave height on the wavelength.

2.3 Cummins' Theory

The wave-driven motion of the water surrounding a UUV induces loads on that vehicle. For purposes of clarity, it is worthwhile to define the orientation of these forces and moments. The UUV experiences longitudinal, side, and vertical forces referred to as F_x, F_y, and F_z, respectively. Figure 2.2 shows the forces and their orientations. The vehicle also experiences roll, pitch, and yaw moments. Relative to the axes drawn in Figure 2.2, the roll is about the x-axis, the pitch is about the y-axis, and the yaw is about the z-axis. These are annotated as M_x, M_y, and M_z. These force and moment values indicate the response and performance of a given hull form, providing a means for comparison between hull designs. The values of greatest interest in this research are the longitudinal and vertical forces, as well as the resulting pitch moment. Cummins determined the net forces and moments for a submerged body of revolution with any forward speed and any relative wave heading exposed to a regular train of waves (Cummins 1954b).These expressions can be simplified for the specific application used in this experiment: that of a stationary model with head seas. Because it is a symmetric model, some of the forces and moments are not expected to be significant. With a vehicle oriented normal or perpendicular to the oncoming wave train, or head seas, there are no forces expected from the side. As it follows, the roll and yaw moments are also not expected to be of concern for this application. The resulting items of

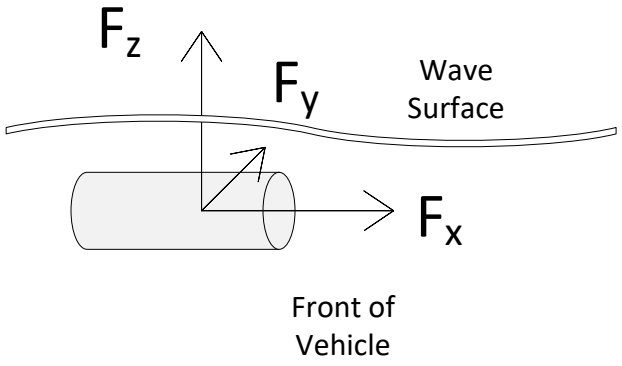

Figure 2.2. Orientation of Forces Relative to Underwater Vehicle Orientation

interest are the longitudinal force (F_x), the vertical force (F_z), and the pitch moment (M_y). The expressions for these elements are produced in the concurrent work by Turner, Klamo, and Kwon (2018). The work is unpublished at the time of this writing, but is accepted for publication in the proceedings for the American Society of Mechanical Engineers' 37th International Conference on Ocean, Offshore and Arctic Engineering in June 2018. The simplified expressions for the components of interest are (Turner, Klamo, and Kwon 2018):

$$F_x = -\frac{\pi}{2}\rho g A_o h\left(\frac{L}{\lambda}\right)\mathrm{e}^{-2\pi\frac{D}{L}\frac{L}{\lambda}} b_0 \cos(\omega_e t), \tag{2.4}$$

$$F_z = -\pi\rho g A_o h\left(\frac{L}{\lambda}\right)\mathrm{e}^{-2\pi\frac{D}{L}\frac{L}{\lambda}} b_0 \sin(\omega_e t), \tag{2.5}$$

and

$$M_y = \frac{\pi}{2}\rho g A_o L h\left(\frac{L}{\lambda}\right)\mathrm{e}^{-2\pi\frac{D}{L}\frac{L}{\lambda}} a_1 \cos(\omega_e t). \tag{2.6}$$

In these expressions, ρ is fluid density, g is gravitational acceleration, A_o is the cross-sectional area of the body, h is wave height, L is length of the body, and λ is wavelength. D is the center-line depth of the vehicle, referred to as a component of H' in the original work. The encounter frequency is ω_e and t is time. The values a_1 and b_0 are integral values

which account for the geometry of the body. After evaluating the expressions and reducing terms, the resulting simplified expressions are below (Turner, Klamo, and Kwon 2018).

$$\begin{aligned} a_1 =& 2\left(\frac{L}{D}\right)^2\left(\frac{\lambda/L}{\pi}\right)^4\left\{-\left[(\alpha-1)^2\left(\frac{\pi}{\lambda/L}\right)^2+6\right]\sin(\alpha\frac{\pi}{\lambda/L})\right. \\ &+\alpha\frac{\pi}{\lambda/L}\left[(\alpha-1)^2\left(\frac{\pi}{\lambda/L}\right)^2+2\right]\cos(\alpha\frac{\pi}{\lambda/L}) \\ &+2\left[(\alpha-1)\left(\frac{\pi}{\lambda/L}\right)^2+3\right]\sin(\frac{\pi}{\lambda/L}) \\ &\left.+2(2\alpha-3)\frac{\pi}{\lambda/L}\cos(\frac{\pi}{\lambda/L})\right\} \\ &+2\left(\frac{\lambda/L}{\pi}\right)^2\left[\sin(\alpha\frac{\pi}{\lambda/L})-\alpha\frac{\pi}{\lambda/L}\cos(\alpha\frac{\pi}{\lambda/L})\right] \end{aligned} \tag{2.7}$$

$$\begin{aligned} b_0 =& 2\left(\frac{L}{D}\right)^2\left(\frac{\lambda/L}{\pi}\right)^3\left\{-\left[(\alpha-1)^2\left(\frac{\pi}{\lambda/L}\right)^2+2\right]\sin(\alpha\frac{\pi}{\lambda/L})\right. \\ &\left.+2\sin(\frac{\pi}{\lambda/L})+2(\alpha-1)\frac{\pi}{\lambda/L}\cos(\frac{\pi}{\lambda/L})\right\} \\ &+2\left(\frac{\lambda/L}{\pi}\right)\sin(\alpha\frac{\pi}{\lambda/L}) \end{aligned} \tag{2.8}$$

α in Equations 2.7 and 2.8 is a non-dimensional term of $\frac{L/D-1}{L/D}$. Once the values for a_1 and b_0 are substituted into Equations 2.4 through 2.6, the theoretical values can be determined for a specified vehicle under given wave conditions and operating depth. The expressions for a_1 and b_0, however, are specific to a cylindrical body with hemispherical end caps.

Cummins further suggests that the forces are proportional to a depth-dependent exponential decay (Cummins 1961, 2):

$$F \propto e^{-2kD}. \tag{2.9}$$

This is the source for the exponential decay terms in Equations 2.4 through 2.6 and indicates the depth dependence. The end result is that for shorter wavelengths, the depth at which the wave-induced forces minimize are somewhat shallow. For longer wavelengths, however, the effective influence of the waves is deeper.

Cummins' work provides a theoretical reference for comparing experimental results. His work specifically concerns the forces and moments of a vehicle with an arbitrarily-varying circular cross-section. Cummins does discuss a research effort in which an attempt is made, but the scope of the effort is limited (Cummins 1954a). His theory is also meant for idealized structures, which that experimental effort did not use (Cummins 1954a). The test results can be compared to the predicted values from the theory.

2.4 Non-dimensional Parameters

This work largely seeks to present data according to certain non-dimensional parameters. The underlying physics that describes vehicle behavior is in the form of non-dimensional parameters. For a given non-dimensional value, all systems regardless of their actual parameters have the same non-dimensional response. The relationships between design parameters and environmental conditions are of interest and permit simplified scaling and application of test results. For example, the ratio between the wavelength of an incoming wave and the length of the model is more important for predicting system behavior than either of those values alone. The behavior is expected to depend on the ratio and be consistent for all vehicles with identical ratios, regardless of actual dimensions. Whether the wavelength is shorter or longer than the vehicle affects the behavior of the observed response.

A specific non-dimensional parameter used in this work is the ratio between wavelength and vehicle length as referred to above. This ratio can be written as λ/L. Another useful ratio is that of the vehicle diameter to the center-line depth of the vehicle, or d/D ratio. This value directly relates the size of the vehicle to its depth from the surface. Lastly, the final results for the research will be presented as non-dimensional coefficients which account for the unique characteristics of the test models and conditions. These were determined by dividing by the model-specific constants such as area A_o and model length L as well as water density ρ and gravity g. The coefficients for forces are described by

$$C_F = \frac{F}{\rho g A_o h} \tag{2.10}$$

and

$$C_M = \frac{M}{\rho g A_o h L} \tag{2.11}$$

describes the moment coefficients. As discussed previously, Cummins suggested an exponential relationship between the depth and the force and moment magnitudes. To evaluate this assertion, a similar approach is taken as with the non-dimensional coefficients described in Equations 2.10 and 2.11. A non-dimensional coefficient S is similarly defined but also accounts for this exponential decay. The vertical force coefficient is defined as

$$S_F = \frac{F}{\rho g A_o h \mathrm{e}^{-2\pi D/\lambda}} \tag{2.12}$$

and

$$S_M = \frac{M}{\rho g A_o h L \mathrm{e}^{-2\pi D/\lambda}} \tag{2.13}$$

describes the moment coefficient. The non-dimensional coefficients are intended to be more easily applied than values directly dependent on specific wave or vehicle conditions. The overall intent is to better enable the results presented here for use in later work.

2.5 Effective Diameter

The underlying theory governing the forces and moments acting on a body of revolution rely on the cross-sectional area of the body as seen in Equations 2.4 through 2.6. As the intent of this research is to consider the effects of shape on these loads, a reference area is necessary for comparing between shapes and also for relating to the theoretical model. The effective diameter is that which produces the equivalent area for a circular cross-section. This diameter also controls depth placement, allowing all testing at a given d/D ratio to be conducted with identical center-line depths for all models. All of the shapes considered in this research have nearly-identical cross-sectional areas and therefore have identical effective diameters.

2.6 Chapter Summary

There is adequate theory for describing the forces and moments on a body of revolution. This provides a reference for comparison against the experimental results of this research. The theoretical expressions provide a basis for validating the experimental setup. Additionally, they create a means of considering different cross-sectional hull geometries.

THIS PAGE INTENTIONALLY LEFT BLANK

CHAPTER 3:
Test Setup and Equipment

3.1 Chapter Introduction

This chapter discusses the test environment for the experiment, including the tank, the wave-generation method, and the sensors used to measure the wave environment and loads on the body. A description of the test setup for measuring forces and moments is also provided, along with a verification of the sensor.

3.2 Wave Environment

The wave environment is created using a tow tank located in Halligan Hall of the Naval Postgraduate School. The tank measures 36 feet long, three feet wide, and four feet deep with a nominal water depth of three feet. At one end of the tank is a vertical-wedge wave generator. The face of the wedge is 35° measured from vertical. It is driven up and down by a linear actuator and motor and is limited to seven inches of total vertical travel due to the structure design. The wedge is controlled by software run from a standalone computer. The software takes frequency and amplitude commands for the wedge, resulting in the necessary wedge motion to create a sinusoidal wave with those parameters. The frequencies and amplitudes are manually entered, giving the user wide flexibility in the wave environments generated.

3.3 Wave-Dampening Beach

A wave-absorbing beach was placed at the opposite end of the tank from the wave maker to minimize wave reflections. It is constructed of two parallel layers of perforated plastic and is nearly the width of the tank. The beach is suspended at the waterline with approximately equal area above and below the waterline and an orientation 12° from the surface. It is shown in Figure 3.1. By using the beach, the waves are able to travel the length of the tank, then mostly dissipate instead of reflecting.

The beach was assessed by producing single pulses of waves with five to seven cycles

Figure 3.1. Wave-Dampening Beach

each and allowing them to propagate through the tank. The amplitudes were separately determined for both the original pulse and the reflection. Figure 3.2 shows the ratios between the reflected amplitudes and the original amplitudes at different frequencies. The red Xs are the ratios determined at each sensor and the blue circles are the ratios from the average of all sensors from a single run. The data indicate that the reflections with the beach in place were generally less than one-tenth of the original amplitude. Without the beach, the reflections were significantly greater at nearly 85% the original amplitudes. The wave dampening allows for more consistent wave behavior in the tank and also allows longer test runs than would otherwise be possible.

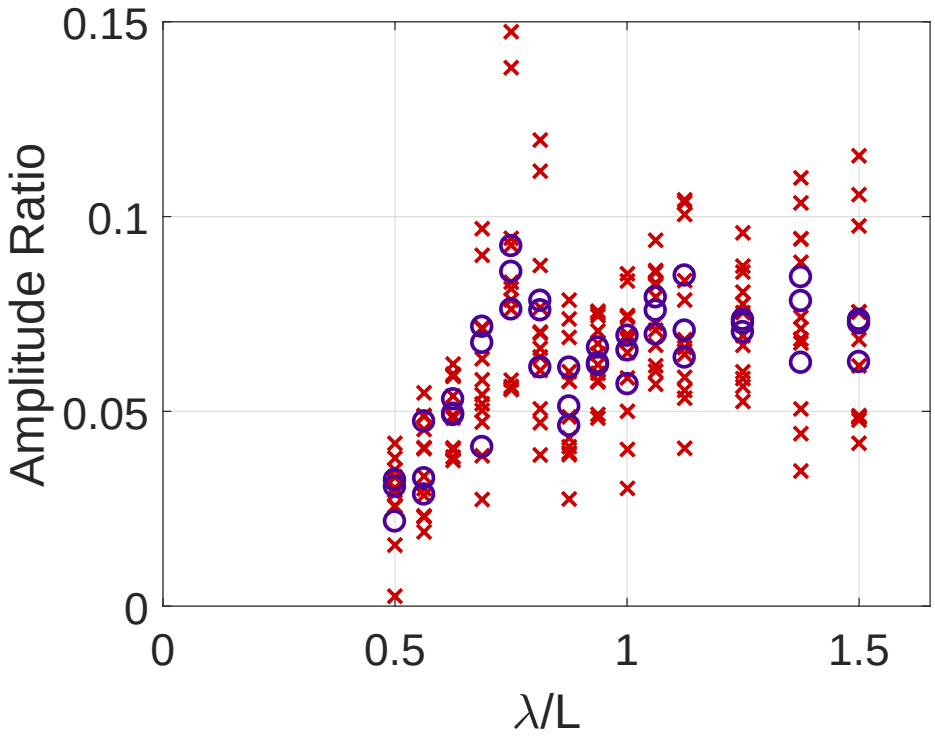

Figure 3.2. Ratio of Reflected Wave Amplitude to Original Wave Amplitude Plotted against Frequency

3.4 Sting

A sting-type setup connects the models to the U-channel and the load cell. It is oriented perpendicular to the channel and extends down into the tank. There are multiple mounting holes in the vertical sting component. This allows the precise vertical separation between model depths. The length of the sting from the center of the model to the center of the load cell is used to calculate the artificial moment caused by the separation between the model and the load cell. The vertical sting cross-section measures 1- by 1.5- inches and is made of aluminum. At the bottom of the sting is a horizontal arm which connects to the test models. The horizontal sting has a diameter of 1.25 inches and extends seven inches from the center of the vertical sting to the rear of the model. It extends another 10 inches inside the model where it connects to an internal support structure. Figure 3.4 shows the sting in its test position.

3.5 U-Shaped Channel

An aluminum channel connects the model and sting structure with the load cell. The channel is shaped like a U and is oriented horizontally with the opening facing downward. There are mounting holes for holding ultrasonic sensors. Multiple mounting positions along the channel support models of different design lengths. Each mounting position also allows testing of different yaw and pitch angles. The channel is connected at the load cell and positioned such that the center of buoyancy for each hull-form geometry is directly below the load cell. This establishes the geometric center of the model as the model origin and enables simple translation of the measured loads from the sensor origin to the center of buoyancy. The channel also extends well beyond the load cell connection and has counter-weight mounting points. Figure 3.4 shows the U-shaped channel.

3.6 Support Structure

A support structure was designed for the test setup to isolate the test models and sensors from the tank. It is built from 80/20 extruded aluminum and stands around, but does not make contact with, the tank. It is shown in Figure 3.4. Two large pieces of aluminum span the width of the tank, but attach to the top of the new structure. The load cell attaches to one of these cross-pieces, suspended beneath it. The U-channel is then suspended beneath that as shown in Figure 3.4. The wave generator motion vibrates the tank. The new setup was

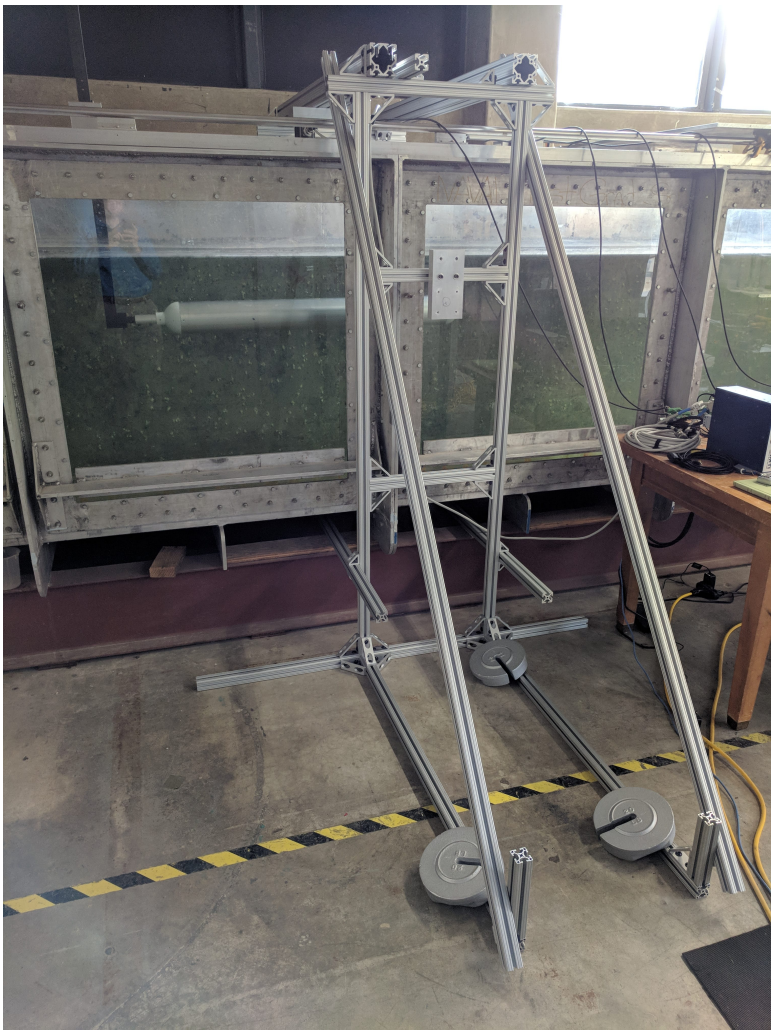

Figure 3.3. Test Support Structure Constructed of 80/20 Extruded Aluminum with Circular Model Suspended from U-Channel

seen to make a clear improvement in the data quality and considerably reduced the noise level caused by the tank vibrations.

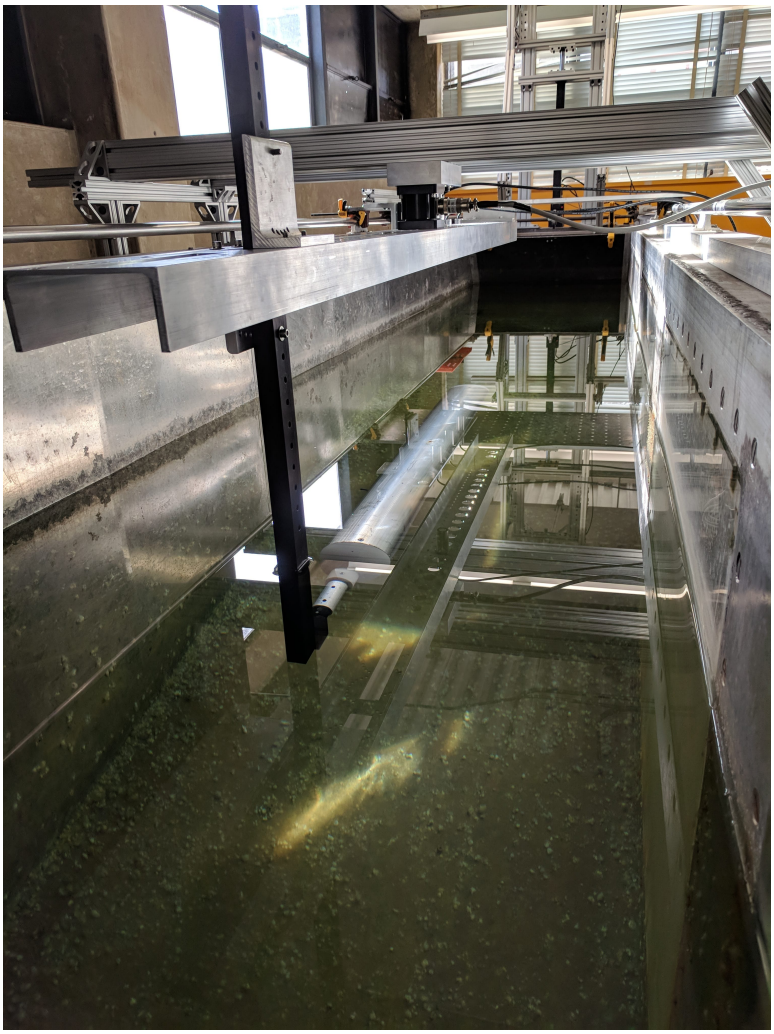

Figure 3.4. Rear View of Test Setup Showing Aluminum Cross-Beam, Load Cell, and U-Channel

3.7 Load Cell

An AMTI MC3A-500 load cell is used to measure the forces and moments in this experiment. The load cell interfaces with an AMTI Gen5 signal conditioner unit with USB computer connection. It has six independent channels, each measuring a separate force or moment. A photo of the load cell in its test configuration is shown in Figure 3.5. The load cell has a capacity of up to 500 pounds for F_z and 500 inch-pounds for M_x and M_y. The limits for F_x and F_y are 250 pounds. The maximum measurement for M_z is 250 inch-pounds (Advanced Mechanical Technology Incorporated 2000). Each channel of the load cell has

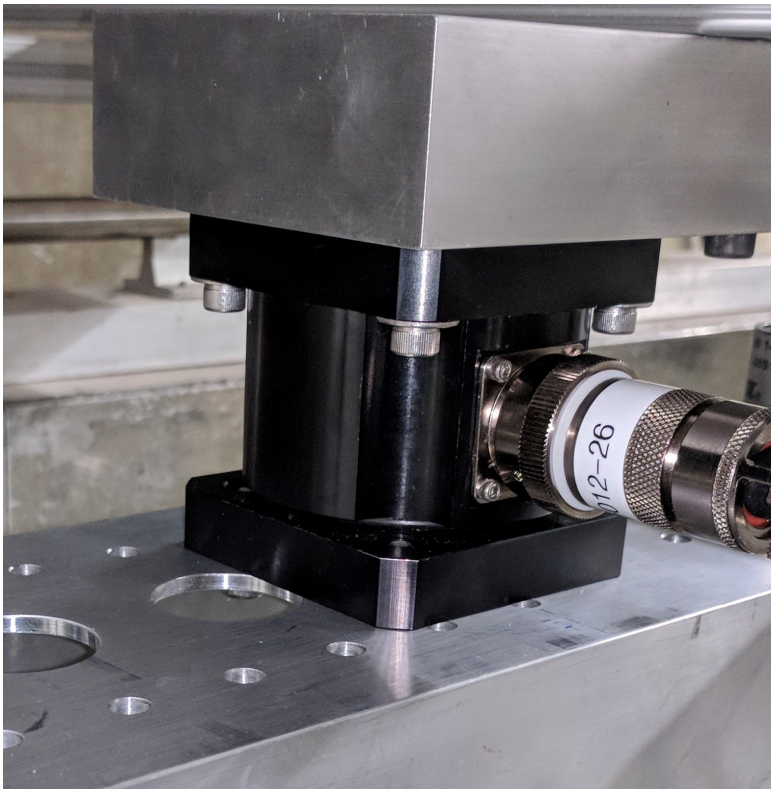

Figure 3.5. AMTI MC3A-500 Load Cell in Test Configuration

independent excitation voltage, gain, and resulting measurement ranges. Tables 3.1 and 3.2 show the configuration settings. A bench-test of the load cell was conducted to evaluate how accurately it measures forces and moments. This was achieved by first applying forces in five-pound increments up to 15 pounds in both the positive and negative directions for all three force axes. The results are shown in Figure B.1. More-precise testing was then

Table 3.1. Load Cell Configuration Force Settings

	F_x	F_y	F_z
Excitation Voltage (V)	10	10	10
Gain	4000	4000	4000
Analog Sensitivity	200	200	60
Range (lbs)	± 20.69	± 20.66	± 81.51

Table 3.2. Load Cell Configuration Moment Settings

	M_x	M_y $(d/D \geq 1.5)$	M_y $(d/D < 1.5)$	M_z
Excitation Voltage (V)	10	10	5	10
Gain	2000	500	500	4000
Analog Sensitivity	200	40	20	200
Range (in-lbs)	± 29.80	± 118.18	± 235.45	± 21.23

conducted for each of the three channels-of-interest, F_x, F_z, and M_y. These subsequent tests were conducted at 0.5-pound increments in both positive and negative directions to encompass the expected range of values during model testing. F_x is measured between negative ten and positive ten, shown in Figure B.2. The maximum measurement error for the full range of values with one replicate was under 0.09 pounds, which is within the expected tolerance. F_z spans between 20 and 40 pounds as the U-channel and model have a static weight of about 30 pounds. The data is presented in Figure B.3. The error for this axis was slightly greater at less than 0.25 pounds. The moment M_y was measured between negative- and positive-25 inch-pounds as indicated in Figure B.4 with error less than six inch-pounds. This error is likely to be a result of uncertainty in the moment-arm length. Most of the measured values were within less than two inch-pounds, especially for the smaller applied moment which were achieved using smaller and more-easily placed weights.

To validate the tolerances for F_z and M_y in the test configuration, the load cell was placed in the test setup with the circular model positioned so that the top of the hull was at the still water surface. Weights were placed on the model at 10 inches forward from the center of buoyancy using a weight pan designed and 3D printed for this purpose. The pan has a slotted base and is held in place by a screw in the top of the model. Above the base are four thin legs measuring one-sixteenth inch square, intended to displace as little water as possible and still provide strength to hold the weights in the pan. The weights started at 0.5 pounds

and incremented by the same amount up to eight pounds, resulting in expected moments ranging from five inch-pounds to 80 inch-pounds in five inch-pound intervals. The vertical forces from this verification are shown in Figure B.5 with the residuals displayed in Figure B.6. Note that the measured forces are indicated as negative values, which correlate to the negative-z direction. The measured forces matched the applied forces with the residual differences less than 0.06 pounds. The moment results are shown in Figure B.7 and the residuals are shown in Figure B.8. As with the forces, the measured moments closely matched the applied moments. Looking at the residuals, the differences were less than one inch-pound for most measurements and less than two inch-pounds for the rest. Some of the error may be due to the weight pan which displaces some water during the measurement and also distributes the applied force over the base area instead of a point. While the test setup is also intended to be rigid, there is some natural flex in the horizontal and vertical members. This causes the front of the model to submerge slightly and some water is displaced by the weight pan. Many of the moments are also created by stacking several plates, which come in 0.5-, 1-, 5-, and 10-pound increments. In light of these uncertainties in the applied moment, the load cell uncertainty verified to be within two inch-pounds. Though this is a static test, it is believed that the measured values during dynamic testing in a wave environment are not dramatically larger than these.

3.8 Ultrasonic Sensors

Senix ToughSonic 14 ultrasonic sensors are used to measure the distance to the water surface, shown in Figure 3.6. The sensors are very precise, capable of resolving measurements within four-thousands of an inch (Senix Corporation 2016, 8). The Senix sensors are factory calibrated and assume the speed of sound in the medium is known. Each sensor operates independently and can be calibrated according to the expected range of the object with a minimum threshold of four inches (Senix Corporation 2016, 8). The measured distance is output as a voltage between zero- and ten-volts. The sensors are powered by a 24V DC power supply. They are used to create a sensor array for measuring and verifying wave heights.

Once configured with identical collection settings, the sensors were analyzed to determine the possible spacing. It is desirable to have the wave probes as close together as possible to allow spatial identification of the waves. According to the manufacturer, the sensor signal

propagates in a conical shape with an angle 12°, that is 6° in either direction measured from normal to the sensor face (Senix Corporation 2016, 8). It is not apparent from the provided documentation, but this may treat the sound wave as a line source, thus cylindrical spreading, with an added consideration for diffraction at the sensor face. It was desirable

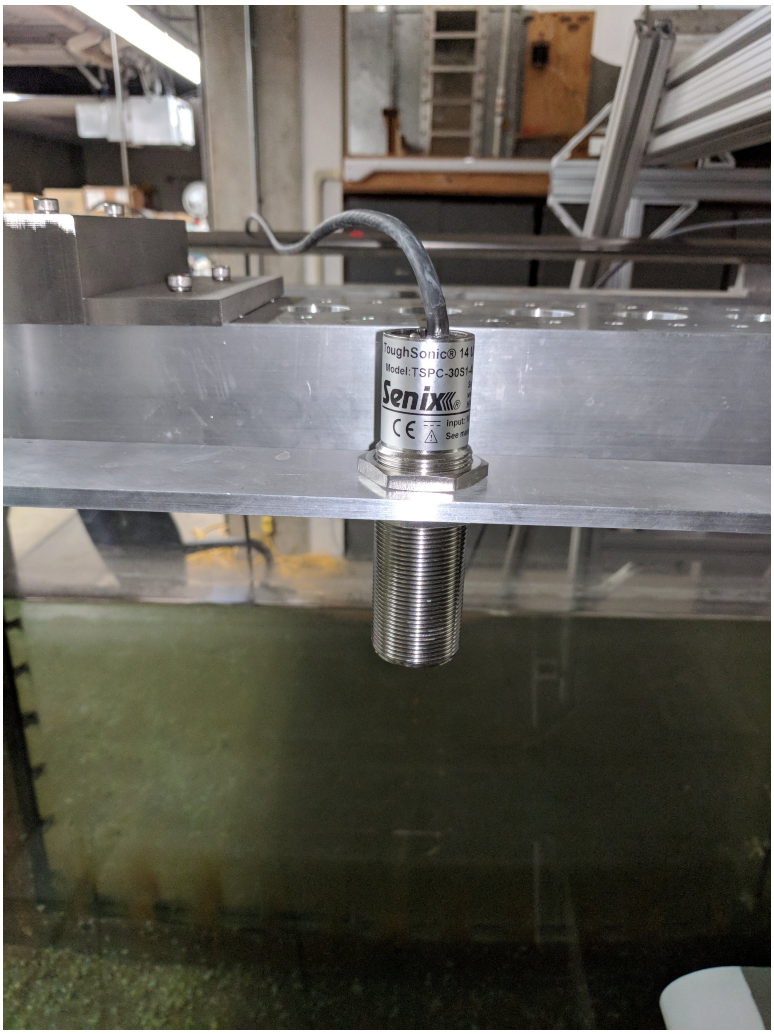

Figure 3.6. Senix 14 Ultrasonic Sensor in Test Mounting

from the outset to use multiple sensors, but there is the possibility for interference between sensors if placed too closely together. The sensors were tested under static conditions to assess the interference and determine spacing. The distance from the sensor face to the still water surface was 17.5 inches and the separation was measured from the center of each sensor. A minimum of two sensors were desired with an objective of using three or

more. A variety of separation distances with both two and three sensors were tested and observed data are shown in Table A.1. As seen in the Table A.1, the mean values were very close to 17.5 inches for all tests with two sensors. Slight variation is likely due to very low frequency, very low amplitude waves that often exist within the tank. There is also slight difference in the actual height of the sensors. The standard deviations were also very small, suggesting excellent precision from the sensors and no interference between them. When a third sensor was added, the mean distances were closely in agreement around 17.5 inches and the standard deviations were similarly small with the exception of the runs at five-inch spacing. Eight inches was determined to be adequate spacing for the sensors based on the observations. It also considers that this short experiment was conducted with a flat wave surface and accounts for greater signal scatter and errant reflection when there are actual waves propagating through the tank.

An array of three sensors was placed between the wave maker and the model with eight inches between each sensor, mounted separately from the channel. They are located 24, 32, and 40 inches forward of the center of buoyancy. A fourth sensor was placed near the load cell, eight inches forward of the center of buoyancy of the model. This sensor was mounted to the U-channel and positioned as close to the center of buoyancy as possible, thus attempting to verify the characteristics of the waves passing directly over the model. The final height of the probes during testing is approximately 12 inches and each set to measure between 5 and 15 inches.

3.9 Data Acquisition Board

A National Instruments USB-6363 data acquisition board samples the analog voltages from the sensors at a specified frequency. The board has analog coaxial inputs for all ultrasonic sensors and the six load cell channels. A 50 Hz sample frequency is used. A USB output connects to the computer which uses MATLAB to collect and store the data.

3.10 Chapter Summary

This chapter described the test environment and equipment used for this research. The sensors used were also presented along with their validations. This is the test setup for evaluating the loads on submerged bodies and facilitates this research.

THIS PAGE INTENTIONALLY LEFT BLANK

CHAPTER 4:
Test Model Design

4.1 Chapter Introduction

As mentioned in Chapter 1, the intent for the research method was to use models with nearly-identical cross-sectional areas. Simple shapes were selected for the cross-sections: circle, square, and rectangle. The circular model provides a comparison point for current hull designs. Many vehicles use circular-cross-section hulls such as the Remus (Jane's by IHS Markit 2018). The square model is a simple comparison in the sense that it is symmetrical and the ratio of cross-section dimensions is one, just as with the circle.

Rectangular models allow greater exploration of how the cross-section effects the loads experienced. Unlike the circle and square, the ratio of cross-sectional dimensions is not unity. Because of this, the rectangle can be considered from two orientations.

In all cases, the dimensions were selected to achieve nearly-identical areas. By using models of the same lengths, the internal volume of each model is also nearly identical. This is meant to facilitate comparison between the different models and limit the experimental factors to only cross-sectional shape. The vehicle volume directly contributes to payload capacity such as batteries, propulsion equipment, computers, communications equipment, and sensors. If the available volume for each model is identical, then the same theoretical payload capacity should be available.

4.2 Circular Cross-Section

By using this type of model, it is intended to represent current designs and provide a comparison for other cross-sectional shapes. This model shape also allows for direct comparison to Cummins' analytical results for a slender body-of-revolution. This model consists of a circular cylinder with hemispherical end caps. A hemi-sphere was selected because it provides a hydrodynamically smooth surface for the bow and stern. This shape also resembles the nose sections of submarines and many other underwater vehicles. The diameter of the model is 4.5 inches, providing an area of 15.9 in^2. This diameter was

selected because it most-closely matches the cross-sectional areas of other models selected from available extruded aluminum options. The other models, which are discussed below, have areas of 16 in^2. The model measures 45 inches in length, including the end caps. This achieves a length to diameter ratio of 10. The parallel mid-body of the model is made of one-eighth-inch thick extruded aluminum tubing and the end caps are printed using additive manufacturing. The end caps are made of polycarbonate with solid fill. These are connected to the mid-body using counter-sunk #10-24 screws, four per end. Bleed holes are drilled identically on four sides of the model and are each one-tenth inch diameter. They are one inch and 12 inches measured from each end, as well as the center length-wise. The outside of the mid-body is the original brushed finish from the manufacturer. This approach not only achieves a reasonably sized model for testing, but it also demonstrates the ability to prototype and test design options rapidly using the established test setup. Figure 4.1 shows the circular model.

4.3 Square Cross-Section

The second cross-section selected was the square. A four-inch square has an area of 16 in^2 and closely-matches the circle in that regard. This model uses semi-cylindrical end caps which are intended to be similar to the hemispheres of the circular model. The overall length is also 45 inches, intended to simulate a comparable design. The main length of the model is made of extruded aluminum with printed end caps. The body finish is the smooth, as-shipped finish. The end caps are polycarbonate with solid fill and are attached with the same counter-sunk screws. The bleed holes are drilled at one inch, 7.5 inches, and 12.5 inches from each end and in the length-wise center of the model. The holes are one-tenth inch diameter and arranged along the center-line of each face. Figure 4.2 shows the model.

4.4 Rectangular Cross-Section

Similar to the square model, a semi-cylinder was used as the nose piece. The model measures two inches by eight inches at its cross-section, resulting in a 16 in^2 area. It is also 45 inches long for the reasons previously identified. An advantage of this shape is that it can be considered from two orientations, with the long dimension either horizontal or vertical. This provides another element to consider. If a rectangular cross-section is used, there may be a difference in loads experienced depending on how it is oriented. As with the other

Figure 4.1. Circular Cross-Section Model

models, extruded aluminum with its original finish was used in its construction. The end caps are solid-filled polycarbonate attached with counter-sunk screws. The screws are all on the eight-inch sides, 1.5 inches inward from each edge. The bleed holes are one-eighth inch and located 0.5 inches, 2.5 inches, and 10 inches from the front and rear, oriented on the wider sides of the model. Figures 4.3 and 4.4 show the model in its horizontal and vertical orientations.

Figure 4.2. Square Cross-Section Model

4.5 Chapter Summary

This chapter explained the considerations in model design. The selected cross-sectional shapes are described and their parameters are given.

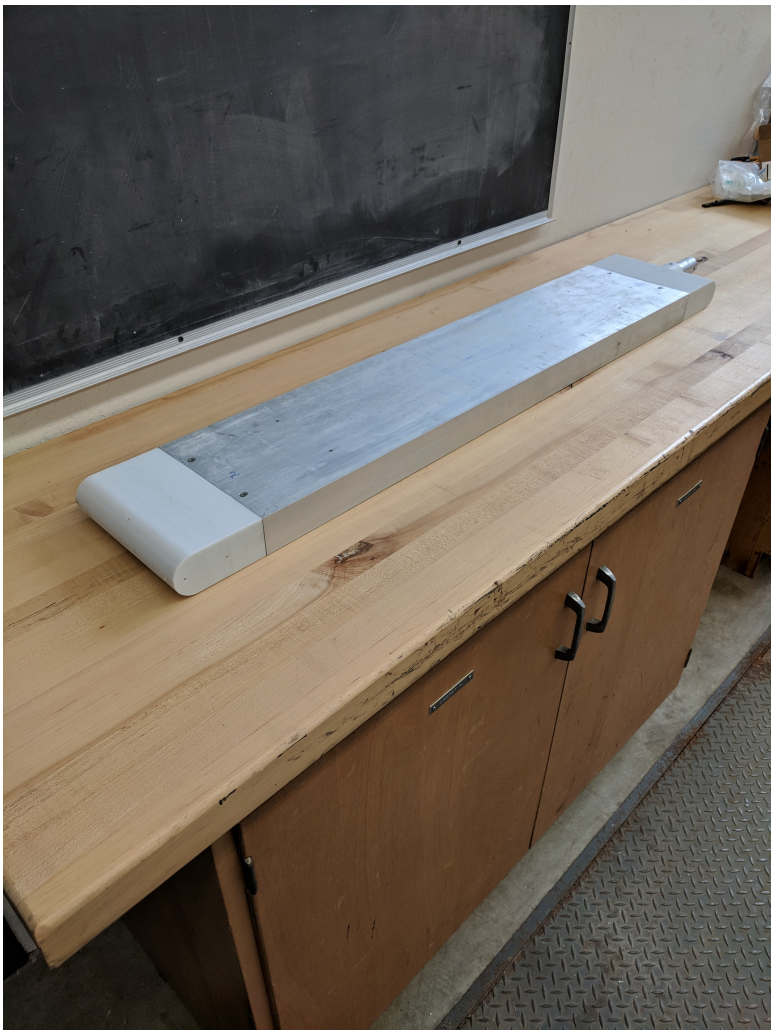

Figure 4.3. Rectangular Cross-Section Model in Horizontal Orientation

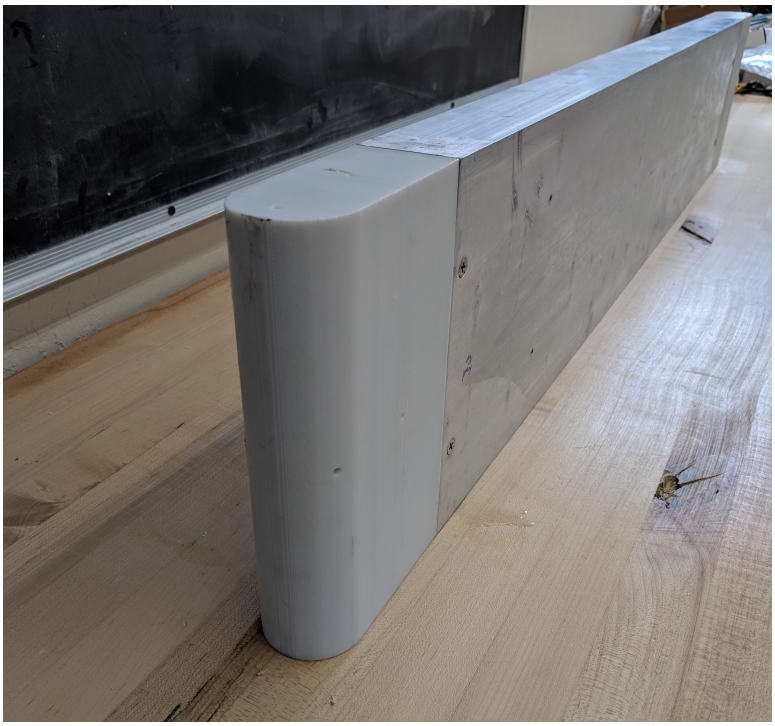

Figure 4.4. Rectangular Cross-Section Model in Vertical Orientation

CHAPTER 5:
Data Reduction

5.1 Chapter Introduction

This chapter describes the data reduction methods used in the research. The data reduction processes enabled accurate verification of the wave environments and determination of the measured force and moment amplitudes.

5.2 Curve-Fitting Function

While it is important to measure the wave heights and loads, it is not sufficient to simply take measurements. The measured signals are oscillatory with multiple frequency components. Additionally, the real data contains not only first-order components, but higher-order components and noise as well. Wave, force, and moment amplitudes cannot be determined by simply taking half the distance between maximum and minimum values. The collected data must be processed to extract useful information, specifically the wave amplitude and phase. This was achieved through least squares data regression.

The first consideration was to evaluate the wave independently of the phase component, which could have any value between zero and 2π depending on the moment the data collection started. This was done by applying the trigonometric identity of harmonic addition:

$$F\sin(kx - \omega t + \theta) + C = A\sin(kx - \omega t) + B\cos(kx - \omega t) + C. \tag{5.1}$$

Consider that for a series of data, the root-mean-square error in a curve fit can be expressed as shown in Equation 5.2 (Atkinson 1985, 258):

$$Error = \sqrt{\frac{1}{n}\sum_{i=1}^{n}[f(x_i) - \eta_i]^2}. \tag{5.2}$$

In the above equation, $f(x_i)$ is the predicted value at x_i based on the curve fit and η_i is the

measured value. By squaring all of those differences and taking the root of the average, the error can be quantified. The general objective for any curve fit is to minimize this error. This can be accomplished by minimizing the sum component of Equation 5.2. For this particular case, we can designate the curve fit to be a function of A, B, C, k, ω, x, and t where it takes the general form shown in Equation 5.1. Position x is constant for each Senix sensor and for the load cell. The frequency is determined by using a MATLAB function designed by Professor Klamo which converts a time-iterated data array into the frequency domain using the Fourier transform. The value with the peak signal is located and determined to be the primary wave frequency. These values invariably correlated with the desired frequency, but served as a verification for the generated waves. The third-order dispersion wave relationship for deep water as shown in Equation 2.3 is solved using the secant method to estimate the wavelength. The third-order expressions captures the effects of a finite wave amplitude on the wavelength.

The curve fit reduces to a function of the amplitude coefficients A, B, and C. The summation can then be written as

$$G(A, B, C) = \sum_{i=1}^{n} [A \sin(kx - \omega t_i) + B \cos(kx - \omega t_i) + C - \eta_i]^2. \tag{5.3}$$

According to Atkinson, the values of A, B, and C that minimize the error are those that satisfy the following constraints:

$$\frac{\partial G}{\partial A} = 0, \tag{5.4}$$

$$\frac{\partial G}{\partial B} = 0, \tag{5.5}$$

and

$$\frac{\partial G}{\partial C} = 0. \tag{5.6}$$

By taking the partial derivatives of G with regard to A, B, and C, the following results are obtained.

$$\begin{aligned} \frac{\partial G}{\partial A} = A \sum_{i=1}^{n} \left[\cos^2(kx - \omega t_i)\right] + B \sum_{i=1}^{n} [\sin(kx - \omega t_i) \cos(kx - \omega t_i)] \\ + C \sum_{i=1}^{n} [\cos(kx - \omega t_i)] - \sum_{i=1}^{n} [\eta_i \cos(kx - \omega t_i)] \end{aligned} \tag{5.7}$$

$$\frac{\partial G}{\partial B} = A\sum_{i=1}^{n}\left[\sin\left(kx-\omega t_i\right)\cos\left(kx-\omega t_i\right)\right] + B\sum_{i=1}^{n}\left[\sin^2\left(kx-\omega t_i\right)\right] + C\sum_{i=1}^{n}\left[\sin\left(kx-\omega t_i\right)\right] - \sum_{i=1}^{n}\left[\eta_i \sin\left(kx-\omega t_i\right)\right] \tag{5.8}$$

$$\frac{\partial G}{\partial C} = A\sum_{i=1}^{n}\left[\cos\left(kx-\omega t_i\right)\right] + B\sum_{i=1}^{n}\left[\sin\left(kx-\omega t_i\right)\right] + CN - \sum_{i=1}^{n}\left[\eta_i\right] \tag{5.9}$$

Setting each equal to zero as indicated above in Equations 5.4 - 5.6, they can be rearranged to the following form:

$$A\sum_{i=1}^{n}\left[\cos^2\left(kx-\omega t_i\right)\right] + B\sum_{i=1}^{n}\left[\sin\left(kx-\omega t_i\right)\cos\left(kx-\omega t_i\right)\right] + C\sum_{i=1}^{n}\left[\cos\left(kx-\omega t_i\right)\right] = \sum_{i=1}^{n}\left[\eta_i \cos\left(kx-\omega t_i\right)\right], \tag{5.10}$$

$$A\sum_{i=1}^{n}\left[\sin\left(kx-\omega t_i\right)\cos\left(kx-\omega t_i\right)\right] + B\sum_{i=1}^{n}\left[\sin^2\left(kx-\omega t_i\right)\right] + C\sum_{i=1}^{n}\left[\sin\left(kx-\omega t_i\right)\right] = \sum_{i=1}^{n}\left[\eta_i \sin\left(kx-\omega t_i\right)\right], \tag{5.11}$$

and

$$A\sum_{i=1}^{n}\left[\cos\left(kx-\omega t_i\right)\right] + B\sum_{i=1}^{n}\left[\sin\left(kx-\omega t_i\right)\right] + CN = \sum_{i=1}^{n}\left[\eta_i\right]. \tag{5.12}$$

If observed carefully, there is a pattern of an A term, a B term, and a C term in each equation. This allows the equations to be rewritten in matrix form as

$$\begin{bmatrix} \sum_{i=1}^{n}[\cos^2(kx-\omega t_i)] & \sum_{i=1}^{n}[\sin(kx-\omega t_i)\cos(kx-\omega t_i)] & \dots \\ \sum_{i=1}^{n}[\sin(kx-\omega t_i)\cos(kx-\omega t_i)] & \sum_{i=1}^{n}[\sin^2(kx-\omega t_i)] & \dots \\ \sum_{i=1}^{n}[\cos(kx-\omega t_i)] & \sum_{i=1}^{n}[\sin(kx-\omega t_i)] & \dots \end{bmatrix}$$
$$\begin{bmatrix} \dots & \sum_{i=1}^{n}[\cos(kx-\omega t_i)] \\ \dots & \sum_{i=1}^{n}[\sin(kx-\omega t_i)] \\ \dots & N \end{bmatrix} \begin{bmatrix} A \\ B \\ C \end{bmatrix} \tag{5.13}$$
$$= \begin{bmatrix} \sum_{i=1}^{n}[\eta_i \cos(kx-\omega t_i)] \\ \sum_{i=1}^{n}[\eta_i \sin(kx-\omega t_i)] \\ \sum_{i=1}^{n}[\eta_i] \end{bmatrix}.$$

The A, B, and C coefficients can then be solved by matrix division. In this case, the computations were conducted in MATLAB and are shown in Appendix C. For purposes of utility, the function shown in Appendix C was designed to accept a sinusoidal data set with any number of contributing, or superimposed, sine waves. The matrix dimensions are determined by the sizes of the k and ω vectors, repeating the pattern and expanding the matrices accordingly. This feature allows it to accept both simple and complex wave forms, as long as the wave numbers and frequencies are known. By determining the A and B coefficients, the amplitude of the wave can be calculated by

$$D = \sqrt{A^2 + B^2}. \tag{5.14}$$

Similarly, the phase can be calculated as

$$\theta = \tan^{-1}\left(\frac{B}{A}\right). \tag{5.15}$$

It is expected that offset constant C should be zero or near-zero for any single-component wave since it starts at and should be centered around the still-water surface. For the forces and moments, a part of the nonlinear second-order loads has a constant component so this would be captured by the offset term. The calculated amplitude enables verification of the wave height for each data run. Figure 5.1 shows an example of the curve-fitting function.

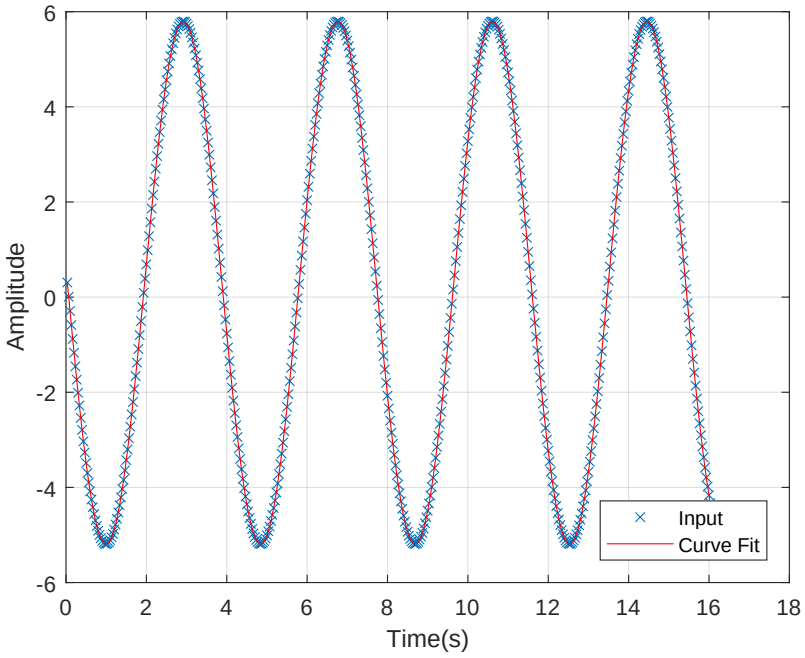

Figure 5.1. Example of Curve-Fitting Function with Synthetically Generated Sine-Wave Data

5.3 Sting Load Corrections

The loads measured by the load sensor include both those experienced by the model and those that are an inherent part of the test structure. The sting was subjected to the full range of test frequencies and depths without a test model attached and the loads recorded. The amplitudes and phases were calculated using Equations 5.14 and 5.15. Curve-fitted values for the longitudinal force, vertical force, and pitch moment are recorded in depth-specific lookup tables according to the test frequency. The values from these tables are used to subtract the sting-induced forces and moments from the measured values. The forces are subtracted as

$$F_{corrected} = F_{measured} - F_{sting} \tag{5.16}$$

and the sting corrections for the moments are made as

$$M_{sting-corrected} = M_{measured} - M_{sting}. \tag{5.17}$$

The measured amplitudes and phases from the sting are both used in these corrections, which accounts for phase differences between the loads.

5.4 Load Origin Movement

The load cell is vertically offset from the center of buoyancy of the test models, which the forces and moments are reported about. It is therefore necessary to translate the measured forces and moments to this desired origin. The application of these corrections assumes a rigid test structure, though there may be some flexibility in the U-channel and sting. The pitch moment must account for the longitudinal-force-induced pitching moment at the load cell. The corrected moment in this case subtracts the product of the moment arm and the measured longitudinal force from the measured moment according to

$$M_{corrected} = M_{sting-corrected} - F_{x,corrected}\,(MomentArmLength)\,. \tag{5.18}$$

5.5 Chapter Summary

This chapter described the primary curve-fitting method used for reducing measured data into amplitude and phase values. These describe the forces and moments experienced by

the models. Corrections for the forces and moments due to the sting were also discussed as well as translation of the measured forces and moments to the center of buoyancy for the test models. These methods enable comparison between different models used in this research.

THIS PAGE INTENTIONALLY LEFT BLANK

CHAPTER 6:
Test Process

6.1 Chapter Introduction

Chapter 6 discusses the test process and the test matrix.

6.2 Experimental Design

The experimental setup is designed to evaluate the various test models at varying depths. At each depth, the models are subjected to a wide array of wave frequencies. These frequencies were determined by referencing the circular model, in particular its length. It was desirable to test over a wide range of λ/L conditions. For the determined model length, the capability range of the wave maker corresponds to λ/L values between 0.5 and two. Taking these values, they were iterated by 0.125 up to 1.5, then 0.25 thereafter. From these λ/L values, the wavelengths and the wave frequencies were calculated using Equations 2.2 and 2.1. These served as the input frequencies for the wave maker. With a desired wave height of two inches, the wedge amplitude commands were determined using a previously-determined transfer function. Those amplitude commands were then verified and iterated until they met the desired amplitude as measured by the ultrasonic sensors. Over the course of testing, these values were generally within one-tenth of an inch from the desired amplitude and rarely exceeded two-tenths. The frequency and amplitude pairs are shown in Appendix D.

Instead of testing a single depth, there was also a desire to test multiple depths to explore how the forces and moments changed through the water column. The depths were defined by the ratio between center-line depth and diameter for the circular model. The depth ratios used are 1, 1.5, 2, and 3. An exception for this test construct is the vertically-oriented rectangular model at a depth ratio of one. At this condition, the center-line depth is 4.5 inches. With the long dimension of the rectangle at eight inches, the extension on one side is four. This leaves only a half-inch distance between the top of the model and the surface under still conditions. With the two-inch wave heights used here, or one-inch amplitudes, the trough of each wave would pass below the top surface of the model. This would have

created a situation where the model's buoyancy would be constantly changing and needed to be taken into account to determine only the hydrodynamic loads. Instead of the model solely being acted upon by the wave motion, the model would have actively interfered with the wave form. The elimination of the shallowest rectangle results in 15 viable test combinations of cross-sectional shape and depth.

In the actual test execution, the model was placed on the test setup for the appropriate test depth. Counter weights were used to balance the static pitch moment and the depth between the surface and the top of the model was verified. For each individual test run, the wedge of the wave maker was exercised down to its home or zero position then re-centered on the starting position. Each frequency was tested a minimum of three times, consisting of an initial test and two replicates, for each combination of model and depth. The order in which the frequencies were tested was continually randomized to minimize systemic bias. There is the potential for a slight bias in the data since all testing for a given model shape and depth was conducted consecutively. While adjusting the model height and swapping out models are relatively simple, they are both time-consuming and doing either of these between each individual run would have been excessively prohibitive. Making these continual adjustments to the test setup also would have severely increased the probability of inadvertently damaging the load cell. This was deemed an acceptable trade-off in the experimental design.

Through this testing construct, the full range of test frequencies and depths were evaluated for the different cross-sectional shapes under consideration. The experiment was designed to minimize error in creating the desired test conditions and in the data-collection processes. By collecting multiple test runs for each combination of frequency, depth, and model shape, greater confidence is achieved than with a single pass of each. The overall design is believed to provide a comprehensive look at the defined decision space and facilitate adequate analysis of the collected data.

6.3 Run Duration

An important consideration in the experimental design is the run duration. There are no real run-time restrictions for the wave maker barring malfunction or damage. The wave conditions also appear to reach steady-state rather quickly, seen both visually and in time-

history plots of the wave data. However, a practical run duration is necessary to achieve efficiency in the data collection.

To find this optimal duration, three data runs with the circular model were collected for each of three λ/L values, selected to be near the ends and middle of the tested range. These runs were each one minute in duration, a value selected as a practical upper limit. The wave period was then determined from the frequency using Equation 2.1. With the wave period, the one-minute data runs were analyzed using an increasing number of wave cycles each time. Figure E.1 shows a plot of the vertical forces for one λ/L condition. The three data styles represent three separate data runs. Since the value of interest is wave cycles, not simply run time, the data is plotted accordingly against the number of wave cycles. The vertical axis shows the amplitude determined by the previously-described curve fitting method and Equation 5.14. This plot represents the worst case for the vertical force among the frequencies considered here. Figure E.2 similarly shows data for the vertical force at λ/L of 1.25.

In theory, an infinitely-long data run would provide many, many wave cycles and allow for the most accurate curve fitting of the data. As previously mentioned, that is not practical or even possible. With increasing duration, however, it is expected that the curve fit should approach the true value in an asymptotic fashion as seen in Figures E.1 and E.2. The data suggests that a 60-second duration is adequate. This duration is used for all test runs regardless of shape, depth, or frequency.

6.4 Test Execution

Prior to conducting data runs, the model is attached to the test setup at the required depth and the water level above the hull is verified. A static reference run is conducted which is later subtracted from the measured values to account for the inherent forces and moments in the setup, such as the weight of the sting and U-channel and slight changes to the calm water depth. Prior to each data run, the wedge is homed and re-centered with new wave commands entered. The waves are allowed to run sufficiently long that they propagate past the model and sting and reach steady-state before beginning the data collection process. Once the collection process begins, the wave and load data is collected for 60 seconds at 50 Hz and stops automatically. The data is collected and written to a text file in comma-separated

format using MATLAB. The script also displays data to the user in real time, so that the wave and load data can be assessed for quality during the run. After the run is complete, a cleaning function is used to remove dropouts from the Senix probes, subtract the static reference, and apply the appropriate gains and orientation to convert the voltages from the sensors into physical units.

An analysis routine executes the curve-fitting function discussed previously for each ultrasonic sensor and for all six channels of the load cell. The calculated amplitudes and phases for each are written to a file in comma-separated value format along with identifying data for the run such as run number, test conditions, and model parameters. The results from the analysis routine are further processed to make corrections for the sting and test setup so that it can be accurately plotted.

6.5 Chapter Summary

This chapter explained the experimental design. In the research method, a wide range of frequencies were tested for each of four test depths and different cross-sectional shapes. All tests utilized a two-inch wave height. A discussion of the necessary run duration was also presented. The test process and design facilitate comparison between test shapes.

CHAPTER 7:
Results and Discussion

7.1 Chapter Introduction

This chapter presents the summary results of the research and provides an analytic discussion of the data. The selected data is structured to compare different depths for each test shape as well as comparisons of the different cross-sectional shapes at each test depth. Vertical forces and pitch moments compose the primary data presented. The longitudinal forces are also discussed.

7.2 Summary Data Curve-Fits

The vertical forces and pitch moments are curve-fit according to the theoretical expressions discussed previously. While the theoretical expression is specifically for a circular cross-section, it was applied to the non-circular shapes as well. This was done under the assumption that the theory should hold for nearly-circular cross-sections like the square. While the rectangle deviates more than the square, it is still interesting to compare whether it has similar behavior as the circle.

The force term was simplified to the form of

$$C_{F_z} = A \sin\left(B\frac{L}{\lambda}\right) e^{C\frac{L}{\lambda}} \tag{7.1}$$

where A, B, and C absorb the remaining terms. The curve-fit coefficients were determined by iterating values for these three variables and identifying the combination which resulted in the smallest residual. Plotting the coefficients sets qualitatively verified the fits as well. The moments were similarly fit to the form

$$C_{M_y} = A\frac{\lambda}{L}\left(\sin\left(B\frac{L}{\lambda}\right) + C\frac{L}{\lambda}\cos\left(D\frac{L}{\lambda}\right)\right) e^{E\frac{L}{\lambda}} \tag{7.2}$$

with coefficients A, B, C, D, and E. Note that this deviates slightly from the theoretical

expression in Equation 2.6 as it only accounts for a parallel mid-body with flat ends instead of the rounded ends actually considered. The difference between the flat and round ends are expected to be minimal and this simplifies the calculation. Flexibility in the five coefficients practically account for these differences. The resulting curves appear to fit the data closely over the range tested.

The error bars were determined by approximating the error between the curve fit and the actual data by a sum-of-squared error method. For each data point, the difference between the measured data and the predicted value from the curve fit is calculated and squared. These values are summed and the square root taken. This resultant value approximates one standard deviation. The error bars as plotted represent two standard deviations above and below the curve-fit prediction, encompassing approximately 95% confidence for the expected distribution of measured values assuming the error is distributed normally.

A limitation of the curve fits is that they are only calculated to a nominal λ/L range between 0.5 and two. As a result, they only capture the nuances of the behavior within that range and some do not wholly depict the theoretical behavior beyond it. Extrapolation of the curves beyond these limits may not be accurate and further testing over a broader range of λ/L ratios would improve the quality of and confidence in the fits.

7.3 Cummins' Theory Validation

Validating Cummins' theory is achieved by plotting the measured force and moment data for the circle with the theoretical values at all four depths. Figures 7.1 and 7.2 show the comparisons.

7.3.1 Vertical Forces

Figure 7.1 shows the vertical forces for the circular model at the four test depths. The theoretical curves are plotted with the measured data. The data follows the theoretical values closely for all depths 1.5 and greater. There is some difference between the data and the theory at depth of one, suggesting the theory does not fully capture the effects at the very-near-surface region. While the amplitudes are fairly similar, the experimental data does not appear to follow the theoretical form for higher λ/L values. Despite the error

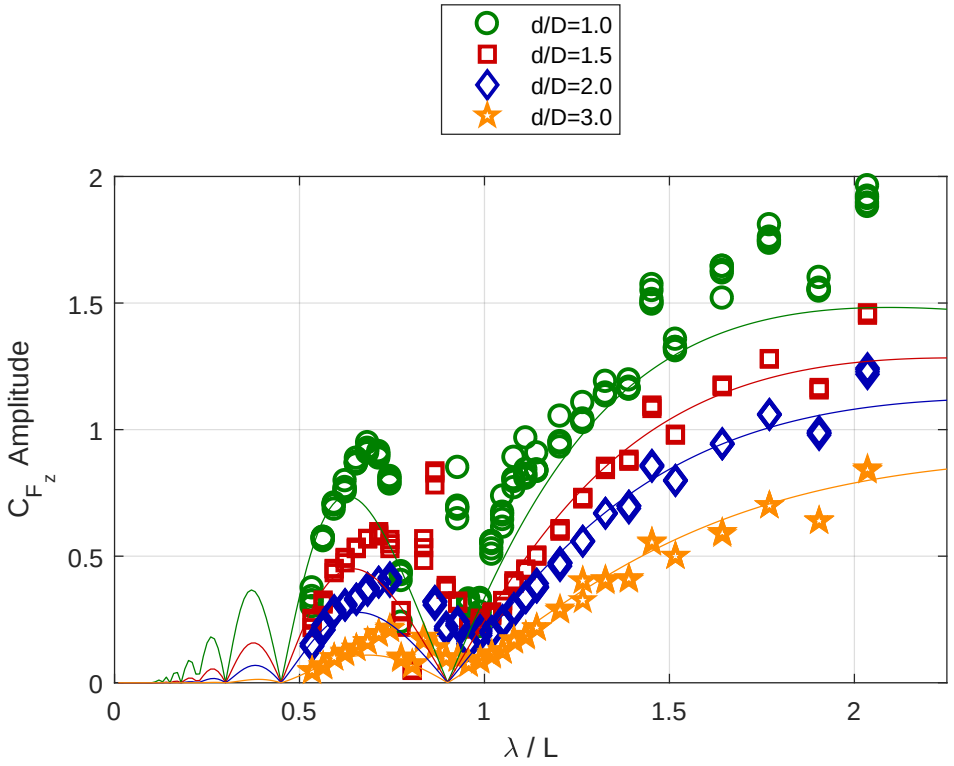

Figure 7.1. Non-dimensional Vertical Forces for the Circular Cross-Section Plotted with Theoretical Curves

for the very-near-surface depth, the theory appears to be reasonably accurate for predicting forces near-surface and deeper.

7.3.2 Pitch Moments

The theoretical moments are similarly compared against the measured circular data. The measured data follows the general form of the theory, but the magnitudes do not concur. This may be a result of the experimental setup since the moment data is corrected for the sting and for the longitudinal forces. Improving the test setup to use a load cell internal to the model would eliminate the need for these corrections and may reduce the difference between the theory and the measured data. It is also possible that the theory does not wholly describe the moments for a submerged body near the surface. The observed trend of good force predictions and less-good moment predictions is considered common for strip-theory-type theoretical results which have difficulty modeling the ends of vehicles.

Figure 7.2 shows that deepest depth has the closest comparison between the data and the theory. The difference increases as the depth decreases with the greatest disparity seen at a depth of one. The theory may accurately predict the moments at greater depths, but there appears to be opportunity for improving the theoretical expression for near-surface depths.

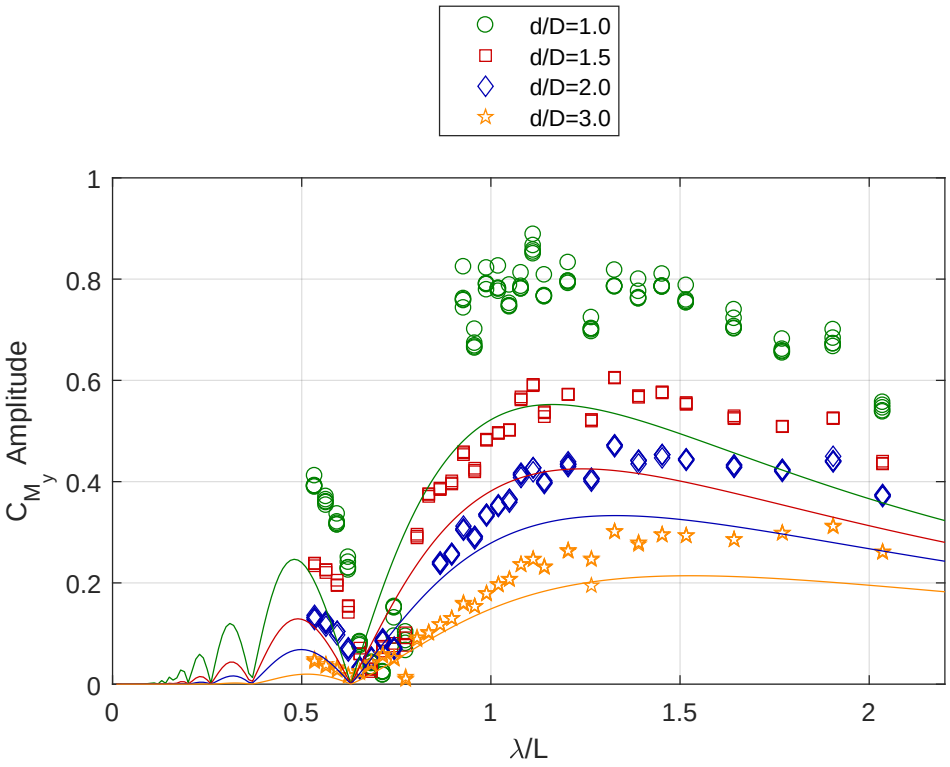

Figure 7.2. Non-dimensional Pitch Moments for the Circular Cross-Section Plotted with Theoretical Curves

7.3.3 Summary

Cummins' theory appears to accurately predict the vertical forces provided the depth is deeper than very-near-surface. However, the theory does not appear to match the shallowest test depth. The experimental moment data does not match the theoretical magnitudes but does appear to follow the theoretical form. This difference may be a result of the experimental setup but it is also possible that the theory does not adequately capture all effects of operating in the near-surface region. Regardless of the differences in amplitudes,

the general form appears to be a good fit. The theoretical expressions for forces and moments are believed to be accurate for curve-fitting purposes. These expressions are used to fit the data for depth and shape comparisons.

7.4 Geometry Effects

To analyze the effects of cross-sectional geometries, the results for each shape are plotted simultaneously for a single depth. This isolates the geometry as the only variable among data sets and allows clear comparison.

7.4.1 Longitudinal Forces

The longitudinal forces appear to remain fairly consistent among shapes for a given depth. This is especially true for the circle, square, and vertical-rectangle cross-sections. There are some differences for the horizontal rectangle, but these are relatively minimal. The force plot for depth 1.5 is shown here as an example. Longitudinal force results for the other depths are shown in Figures F.1, F.3, and F.5. For a characteristic depth of 1.5, the differences are small at λ/L values below 0.75, but increase to about 0.2 as λ/L increases. The horizontal rectangle appears to increase sharply compared to the other geometries at λ/L 0.5. The longitudinal forces are used to account for the artificial pitch moment created by the longitudinal force and the vertical separation between the test models and the load cell. The other needed component for that correction is the longitudinal-force phase.

The phases relative to the incoming wave have similar character as the forces. The measured phases for depth 1.5 are shown here with other depths recorded in Figures F.2, F.4, and F.6. According to the theory, the phases should be 270° at λ/L values below 0.4 and above 0.9 for a circular model with hemispheric end caps. Similarly, the expected values should be 90° at λ/L between 0.4 and 0.9. These theoretical values are shown on the phase plots by solid horizontal lines with the transitions indicated by vertical dotted lines. The measured data appears to follow this theory fairly well. The expected transition appears to occur closer to λ/L 1.1 instead of the expected 0.9. Phases for the circle, square, and vertical rectangle are similar across the frequency range tested, irrespective of depth. The horizontal rectangle, however, appears to deviate consistently from the other shapes and appears to increase almost linearly with λ/L until reaching the theoretical steady-state of

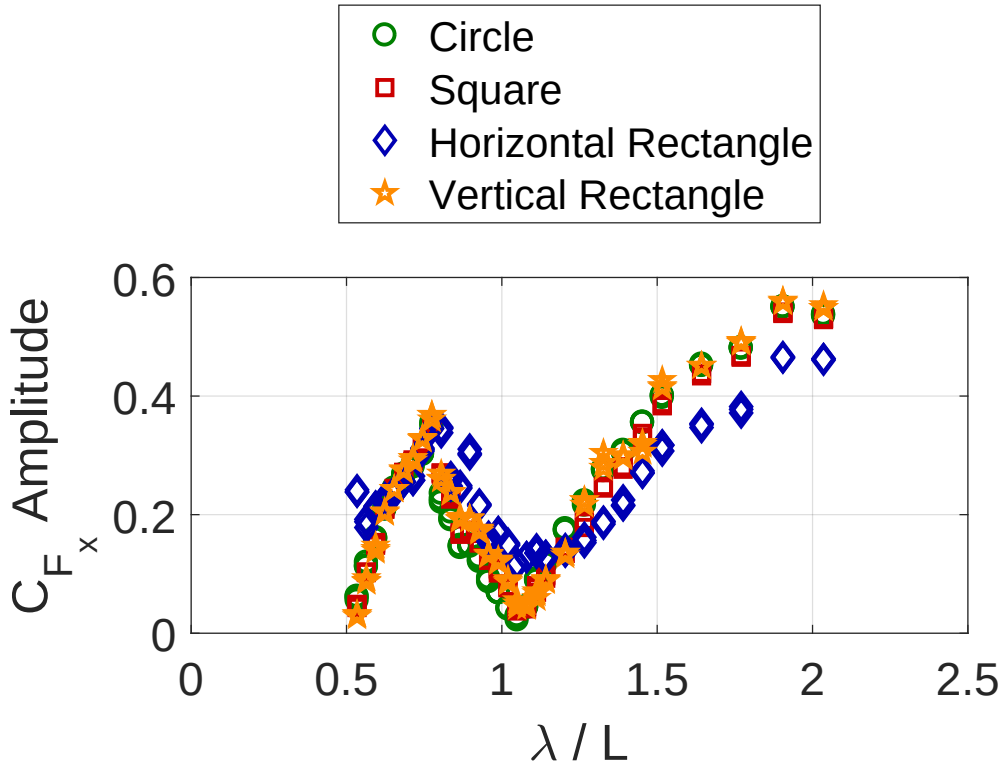

Figure 7.3. Non-dimensional Longitudinal Forces, $d/D = 1.5$

270° above 1.5. An exception to the behavior is seen among all shapes for characteristic depth of three. At this depth, the phase appears to undergo a transition from 270° to 90° at lower λ/L conditions. Regardless, similar results are seen among the three closely-related shapes with the horizontal rectangle differing. These phases are used with the measured forces to correct for the moment as discussed.

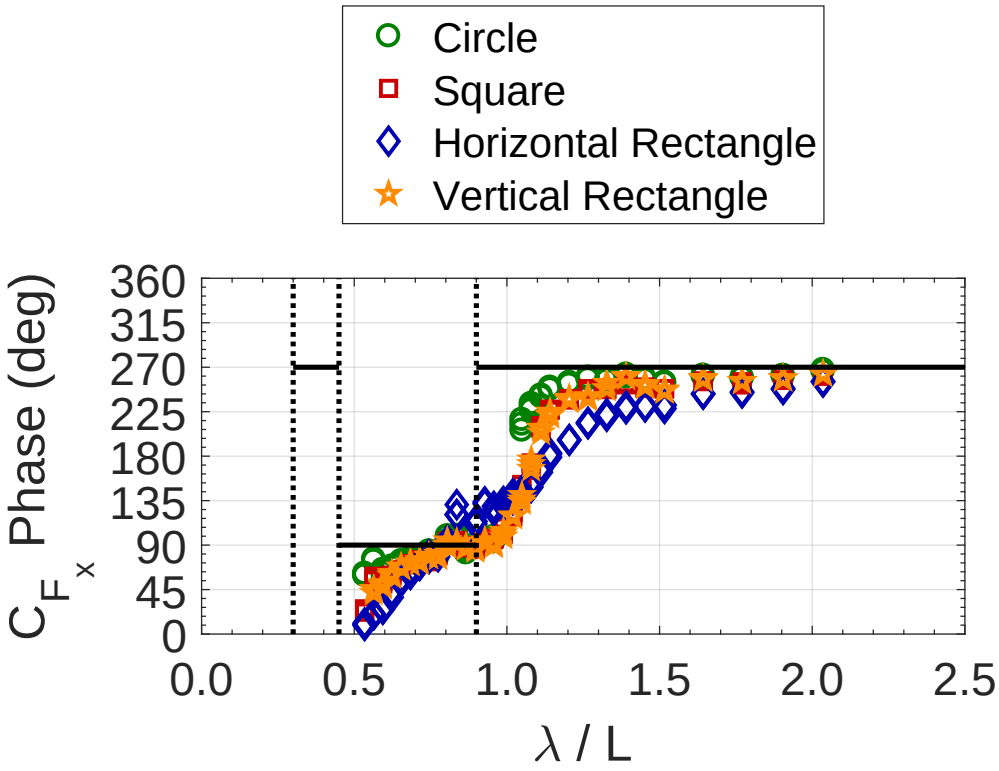

Figure 7.4. F_x Phase Relative to Incoming Wave, $d/D = 1.5$

7.4.2 Vertical Forces

Vertical forces measured during this research display similar behavior as the longitudinal forces. The data for the circular, square, and vertical-rectangular cross-sections are similar with that for the horizontal rectangle deviating significantly. Non-dimensional vertical forces at characteristic depth 1.5 are shown here with remaining depths shown in Appendix F. Figure 7.5 suggests that the horizontal rectangle experiences significantly different forces

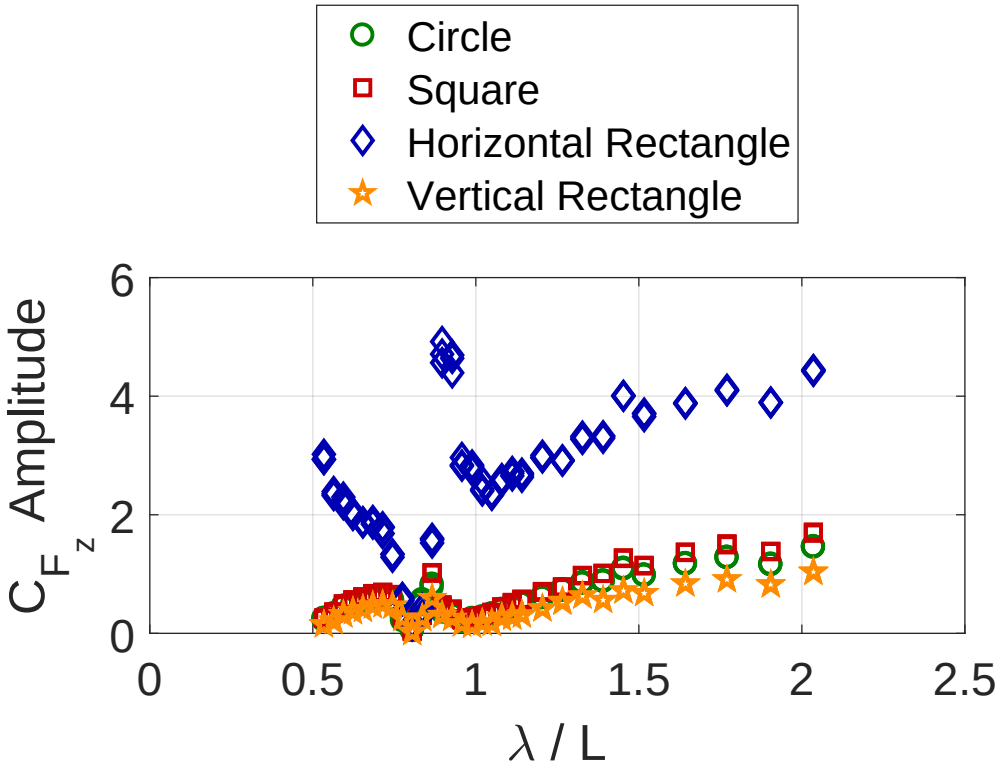

Figure 7.5. Non-dimensional Vertical Forces, $d/D = 1.5$

than the other shapes. The trend is similar in comparison, but with a noticeable difference near λ/L values between 0.5 and 0.7 where it increases sharply with decreasing λ/L instead of decreasing as the others do. This is seen for all depths. The circle, square, and vertical rectangle data were fit according to Equation 7.1 and the coefficients are recorded in Table H.1. The horizontal rectangle data was not fit as it appears to deviate too greatly from the theoretical expression. The curve-fit data at depth 1.5 is shown in Figure 7.6. As seen in the data, there is no significant different between the circle and square at any of the frequencies tested. The vertical rectangle also follows these two closely for most of the test

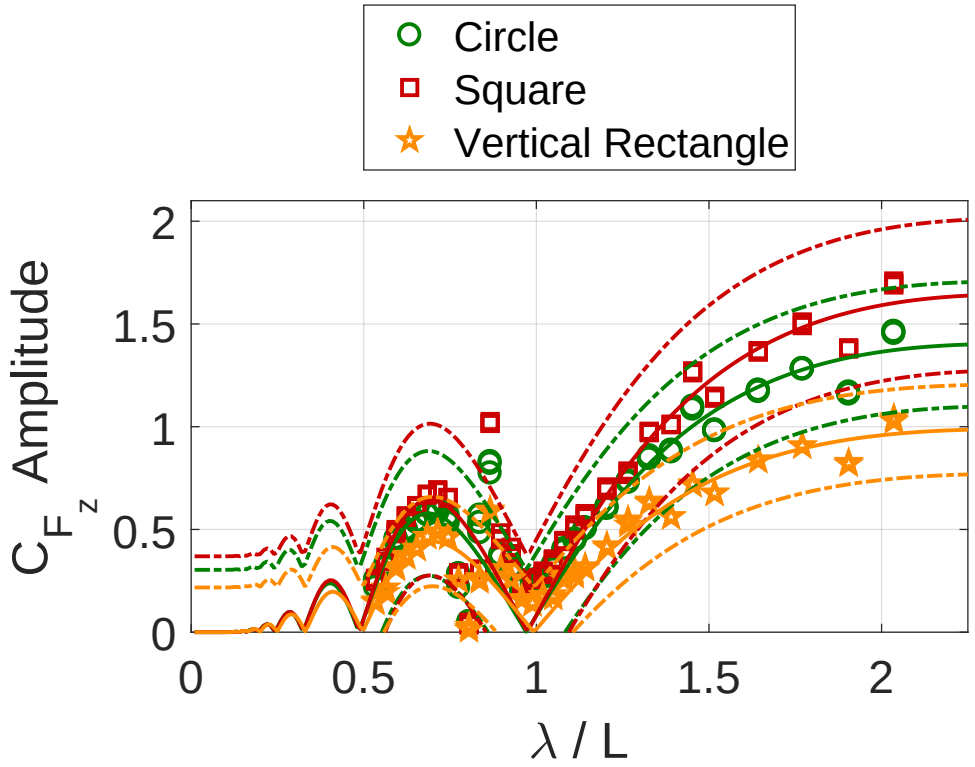

Figure 7.6. Select Non-dimensional Vertical Forces with Curve Fits, $d/D = 1.5$

range, but appears to be smaller at λ/L values above one. These relationships hold across all depths tested with the separation between the rectangle and other two increasing with depth. Looking at Figure F.12, beyond λ/L of 1.5 the vertical rectangular data is clearly less than the circle and sphere, but the predicted curve was not extended beyond what is shown. As the tested data only covers ratios between 0.5 and two, it cannot confidently predict values outside that range. A greater range of testing is necessary to determine behavior beyond the region explored here.

All shapes displayed some erratic behavior near λ/L=0.75 among all test depths. It is believed that this may be related to some resonant frequency within the test structure, though it is unclear. Further testing may be required to isolate and determine the cause for this behavior, but it does not appear to alter the general trend of the data outside the adjacent frequencies tested.

7.4.3 Pitch Moments

Plots of the pitch moment data suggest that there is little difference between the circle and square models. This is particularly noticeable for depth one, shown in Figure 7.7. The

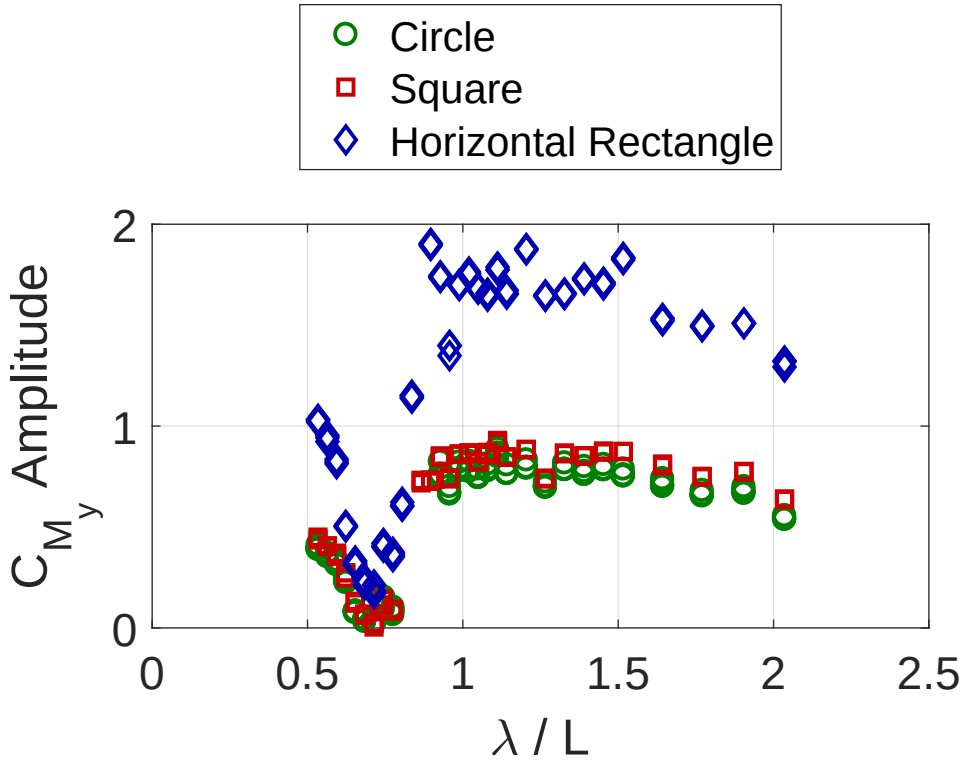

Figure 7.7. Non-dimensional Pitch Moments, $d/D = 1.0$

curve-fitted data for the circle and square test shapes are shown in Figure 7.8. Moment data for the other test depths is shown in Appendix F. The two follow closely and there is no separation between the two data sets for any depth less than three. At depth three, however, there is some separation at the far right end of the plot in Figure F.18. This is likely a result of the limited frequency range tested and not the true behavior. While the square predicted curve turns upward, it should in reality continue downward. This is also seen for both the circle and square at depth two in Figure F.16. The expectation is that as the wavelength becomes increasing long compared to the vehicle length such that the ratio approaches infinity, the surface above the vehicle would appear flat and there would effectively be no force variation along the model and it would experience no moment. This suggests that the predictive curve should continue down to zero.

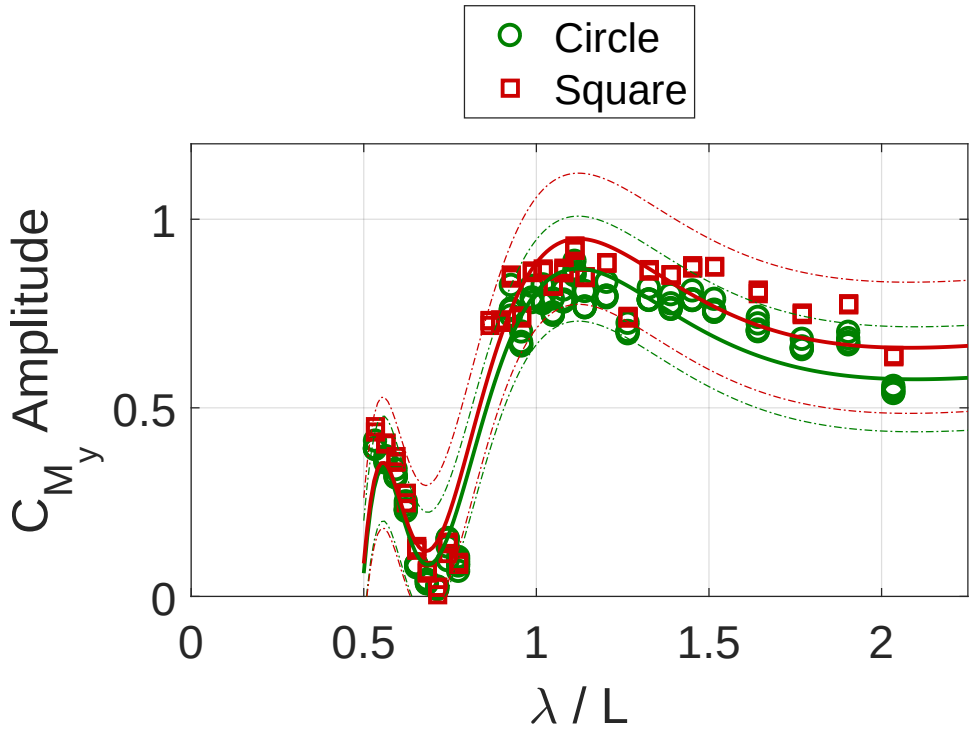

Figure 7.8. Select Non-dimensional Pitch Moments with Curve Fits, $d/D = 1.0$

Similar to vertical forces, the vertical rectangle data appears to separate with some significance from the circle and square. This is seen for depths two and three, particularly at λ/L ratios between one and 1.5. There is little difference among the measured data for the shapes at shorter wavelengths, though some difference in the predicted values is seen.

The horizontal rectangle appears to be significantly different from the other test shapes. Curve-fitting to this data was attempted, but proved impractical due to the severity with which it deviated from the theoretical expression. The observed moment amplitudes for this hull geometry are approximately double for all depths, particularly at λ/L ratios above one.

7.4.4 Summary of Geometry Effects

The data presented strongly suggests that cross-sectional geometry affects the magnitude of the loads experienced by an underwater vehicle. The magnitudes for the square geometry

are consistently greater than those of the circle, but they are still within the estimated 95% confidence band. Similarly, the vertical rectangle is consistently smaller than the circle with the difference being greater than the experimental uncertainty for λ/L greater than one. The horizontally-oriented rectangle has dramatically larger loads. The circle, square, and vertical rectangle are very similar for λ/L values less than one. The horizontal rectangle also appears to depart from the behavior of the other geometries at λ/L=0.5 with a sharp increase in magnitudes. Some geometries appear to provide similar results as the circular reference while some differ only slightly and others are dramatically different. Experienced load magnitudes are dependent on geometry.

7.5 Depth Effects

To evaluate the depth effects, the data is non-dimensionalized according to Equations 2.12 and 2.13. The data in this section is plotted according to test geometry with each data set varying by depth. This removes the depth effects from the presented data for each geometry to assess whether it scales according to the exponential-decay theory.

7.5.1 Vertical Forces

Figure 7.9 shows the vertical forces for the circular model. The data appears consistently larger at $d/D = 1$ compared to the other depths, although it is not greater than the expected uncertainty. The very-near-surface depth of one appears to be somewhat greater than the near-surface depths between 1.5 and 3.0. The square model shown in Figure G.1 displays similar behavior. There are several erratic observations near λ/L 0.75 and the expected causes are discussed earlier in this chapter.

With the horizontal rectangle, the non-dimensionalized values are considerably different at λ/Ls below 0.75, but quickly collapse upon each other at λ/L values beyond that. This is shown in Figure G.2. As with the circle and square, there is some separation between depth one and the other depths. It is worth noting that the values for this shape are approximately five times the amplitudes of the circle and square for λ/L ratios greater than one and between five and 20 times greater for ratios less than one. While the forces for this shape appear fairly consistent at the very-near-surface range, the forces are considerably larger than with the circle or square.

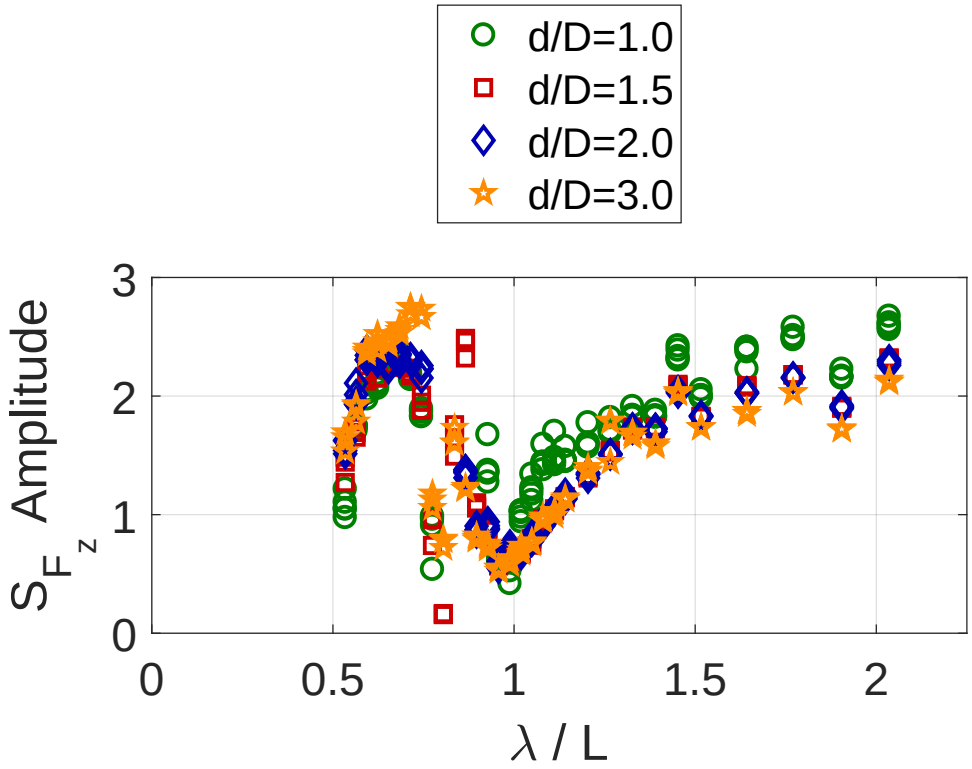

Figure 7.9. Non-dimensional Vertical Forces, Circular Model

Despite the depth-related differences for the horizontally-oriented rectangle, there is little difference among depths with the vertical orientation. The data sets appear to consolidate as seen in Figure G.3. These values are also similar to those observed for the circle and square models. However, this geometry was not tested at the very-near-surface depth of one and cannot be compared.

7.5.2 Pitch Moments

For the circular and square geometries, the moment data appears to consolidate in a fashion similar to what is seen in the forces. There is some separation between the near-surface depths and the very-near-surface. This is shown in Figures 7.10 and G.4.

As with the forces, the moments for the horizontal rectangle are considerably different at short wavelengths and very similar at longer wavelengths. The data for this shape is given in Figure G.5. While the moment coefficients are still within the same order of magnitude

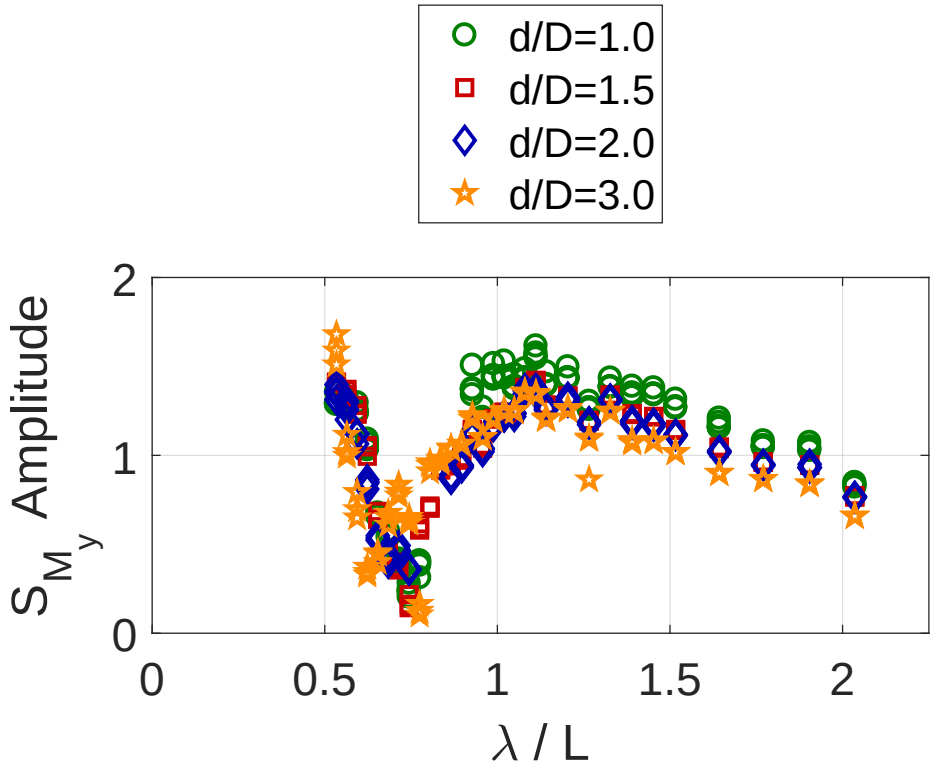

Figure 7.10. Non-dimensional Pitch Moments, Circular Model

as the other geometries, they are noticeably larger than either the circular or square data.

The vertical rectangle results show smaller coefficients than those of the square or circle, especially at the peak just beyond λ/L of one. The coefficients also seem to be similar for all depths, suggesting that the depth dependency follows Cummins' theory. As mentioned for the forces, the very-near-surface could not be tested for this geometry. Changing the model diameter or wave height may enable testing of this region in the future.

7.5.3 Depth Effects Summary

The effects of depth on the forces and moments appear to follow Cummins' theory at the near-surface depths between 1.5 and 3.0. However, the data suggests that it may not hold at shallower depths in the very-near-surface region. The geometry also appeared to affect the load amplitudes, regardless of depth. This is seen in the dramatic difference between forces and moments of the horizontal rectangle and the other test geometries. While there

is some difference depending on geometry, the S coefficients for force and moment are largely independent of depth. It appears that the coefficient adequately captures the effects of the geometry provided the depth is greater than the very-near-surface region. This suggests that it is unnecessary to test multiple depths in the near-surface region and that data for one depth, properly converted to non-dimensional form, can be used to predict loads at any depth provided it is not very-near-surface. More importantly, the data also suggests there is a difference when operating at the very-near-surface, but further research is needed to characterize the effects as the depth transitions between the near-surface and very-near-surface regions.

Plots of the remaining force and moment data organized by geometry are given in Appendix G.

7.6 Chapter Summary

This chapter provided analysis for the data collected in this research. The curve-fitting method for the summary data was described as well as the method for calculating and presenting the associated error. Notable similarities and differences were indicated in the longitudinal force, vertical force, and pitch moment data. Key insights comparing the cross-sectional shapes and depths were presented and the summary impressions of the data given. The content of this chapter provides the foundation for the conclusions and recommendations presented in the next chapter.

THIS PAGE INTENTIONALLY LEFT BLANK

CHAPTER 8:
Conclusion

8.1 Chapter Introduction

This chapter presents concluding thoughts regarding the data discussed in the previous chapter as well as recommendations for application of the material. Ideas for future research are also presented with discussion of how they relate to the present work.

8.2 Conclusion

The cross-sectional geometry of an underwater vehicle affects the loads experienced when operating near the surface. The data presented in the previous chapter suggest there is no significant difference between circular and square cross-sections. A vertically-oriented rectangle appears to experience similar loads at wavelengths shorter than the vehicle length. Conversely, it also experiences reduced loads at longer wavelengths. A horizontal rectangle, however, experiences significantly different force and moment amplitudes compared to the other geometries.

The loads experienced appear to decrease exponentially as depth increases, at least when operating in the near-surface region. Validating the theory promotes the concept that future testing for new hull designs can test a single depth and extrapolate the depth effects by the exponential decay relationship. There also seems, however, to be a difference in the very-near-surface region. Greater testing is necessary to characterize the behaviors unique to this operating region.

There are clear differences among cross-sectional geometries and the resulting wave-induced loads. While this research demonstrated a difference as a proof of concept, further testing is needed to characterize the transition between dimensional ratios for the cross-sectional geometry. There is also a depth-dependency when operating very near the surface. While the loads are predictable for near-surface depths, there is room for greater understanding of the effects at very-near-surface depths. A greater understanding of these areas can improve the early-stage design decisions for shallow-operating underwater vehicle systems.

While non-circular hull geometries can reduce wave-induced loading, there may be other design benefits in using flat versus rounded sides for the hull. Reducing the wave-induced effects can enable vehicle operation closer to the wave surface, thus expanding operational areas and revising operating concepts. The second-order considerations for these design changes are variations in systems architectures and how UUVs integrate as part of a system of systems. This may become increasingly important as trends continue to focus on littoral operations.

8.3 Areas for Further Research

This research effort presumes to contribute to the present field of study and is intended to foster further research. The items that follow are proposed considerations for continuing research efforts.

8.3.1 Dimensional Ratio

Further exploring the effects of dimensional ratio can help determine an ideal design parameter. This research only considered aspect ratios of 0.25 (horizontal rectangle), 1.0 (square and circle), and 4.0 (vertical rectangle). A noticeable difference is identified between the two extremes of the rectangle orientations, but it is not apparent at what ratio the differences become significant when compared to a circular cross-section. A finer treatment of the ratios could improve understanding of how the forces and moments change depending on this ratio.

8.3.2 Very-Near-Surface Depth Testing

Expanded study of the wave-induced effects when operating in the very-near-surface region can improve the understanding of these very-shallow depths. This is likely achieved by testing at characteristic depth ratios of 1.5 and less with finer iteration than what is exercised in this research. Improving the understanding of this area will not only allow for better characterization of the loads, but also provide a better indication of where the region transitions from the near-surface to the very-near-surface. Exponential decay governs the depth effects in the former but does not in the latter.

8.3.3 Yaw Angles

This research only considered waves oriented normal to the parallel mid-body of the model. While this is a simplified approach for testing purposes, a real system is exposed to waves from all bearings. Evaluating the effects from different yaw angles and comparison to these results could produce ideal operating conditions and determine whether the loads change significantly based on encounter angle. Cummins' theory predicts the effects of relative wave heading but they should be validated.

8.3.4 Complex Wave Environments

The waves generated in this research were all of a monochromatic nature. While this simplifies the wave environment, it is not wholly indicative of real-world conditions. Consideration of different cross-sectional shapes under complex wave environments would increase the understanding of whether the forces and moments can be predicted in complex wave fields and whether the shape-based relationships still hold.

8.3.5 Control System Development

Applying the predicted forces and moments for use in control algorithms that include external disturbances is another area for future research. These predictive loads can support sea-keeping and maneuvering research areas. The extent to which control surfaces and control algorithms are required for a given system are likely influenced by the shape of the vehicle and the expected loads.

8.3.6 System Architectures

If non-circular hulls are used to expand the range of operating depths for underwater vehicles, new system architectures may be available for consideration than those previously used. Shallower operating depths may result in different communications or mission options. A detailed analysis of this impact on system architectures, especially in a system of systems context, may improve operating concepts and early system-level design.

8.3.7 Expanded Frequency Testing

Testing a greater range of λ/L would give a better understanding of the design space. Given the test setup and equipment, this would be best accomplished by using shorter models. The same test frequencies and wavelengths used here would produce larger ratios given a smaller model length. This would provide a greater appreciation of the effects under different wavelengths.

8.3.8 Consideration of Second-Order Effects

The testing and analysis conducted in this work only considered first-order forces and moments. However, the second-order effects may contribute significantly to the experienced loads, particularly for larger vehicles. While undoubtedly present for the models tested here, the magnitudes were small. Testing with larger vehicles would serve to validate the scalability of the findings presented here as well as enable expanded measurement and analysis of the second-order effects.

8.3.9 Other Cross-Sections Considered

Other cross-sectional shapes were considered in addition to those selected. The other shape given the most consideration was the ellipse. An elliptical cross-section achieves the same non-unity aspect ratio as the rectangle while also having the rounded edges of a circle. However, this shape also presents several difficulties and uncertainties. Though the edges are rounded, they do not maintain a constant rate of curvature like a circle. The rectangle has an advantage in this aspect, presenting a uniformly-flat surface. It is uncertain how this varying curvature might have impacted the loads experienced. Manufacturing difficulties were also identified. Because elliptical extruded aluminum was not available, this shape would have to be completely 3D printed. The nose piece also introduced some design and manufacturing difficulties both in what the shape should actually be and how best to design it. While these other cross-sectional shapes were not tested during this research, the test method for evaluating them is established and these may be appropriate considerations for future work.

8.4 Chapter Summary

This chapter summarized the conclusions of the research presented in this thesis. Following recommendations, areas for further research were presented.

THIS PAGE INTENTIONALLY LEFT BLANK

APPENDIX A:
Ultrasonic Sensor Data

Table A.1. Ultrasonic Sensor Experimental Spacing Test Results

Run	Sensors	Separation(in)	Mean(in)	Standard Deviation(in)
1	2	14	17.517	0.0132
2	2	13	17.544	0.0081
3	2	12	17.538	0.0041
4	2	11	17.544	0.0056
5	2	10	17.544	0.0043
6	2	9	17.543	0.0033
7	2	8	17.539	0.0050
8	2	7	17.540	0.0045
9	2	6	17.545	0.0060
10	2	5	17.539	0.0071
11	2	4	17.549	0.0068
12	2	3	17.544	0.0063
13	3	3	17.542	0.0051
14	3	4	17.540	0.0049
15	3	5	*17.398*	*0.2040*
16	3	5	*15.113*	*0.4051*
17	3	5	*12.096*	*0.3958*
18	3	6	17.542	0.0038
19	3	6	17.538	0.0055
20	3	6	17.542	0.0052
21	3	7	17.547	0.0040
22	3	8	17.536	0.0063
23	3	8	17.539	0.0038
24	3	9	17.541	0.0061
25	3	9	17.538	0.0043
26	3	10	17.540	0.0041
27	3	10	17.534	0.0048

THIS PAGE INTENTIONALLY LEFT BLANK

APPENDIX B:
Load Cell Verification

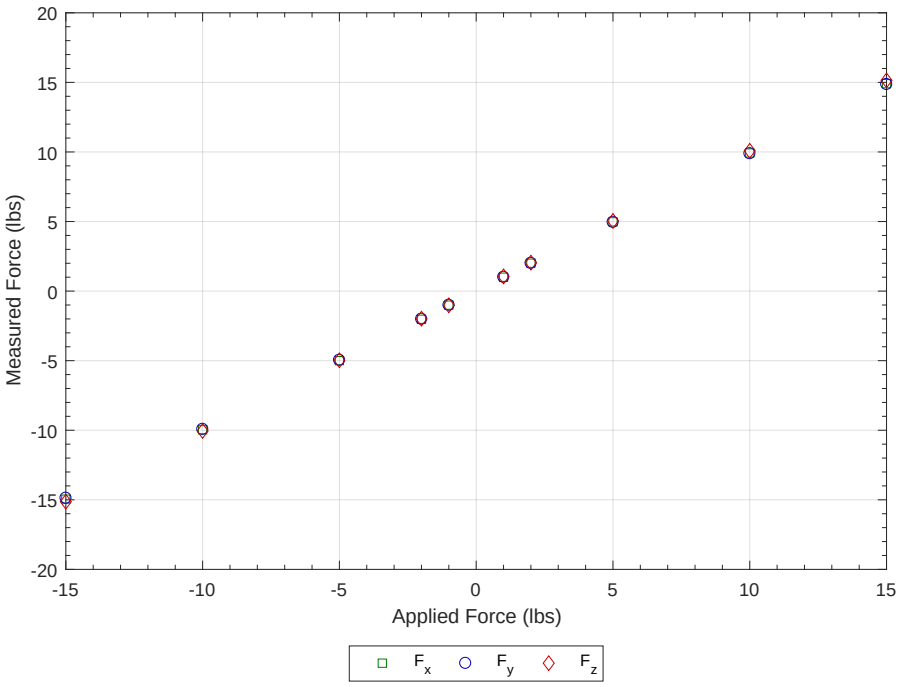

Figure B.1. Course Assessment of Measured Forces vs. Applied Forces

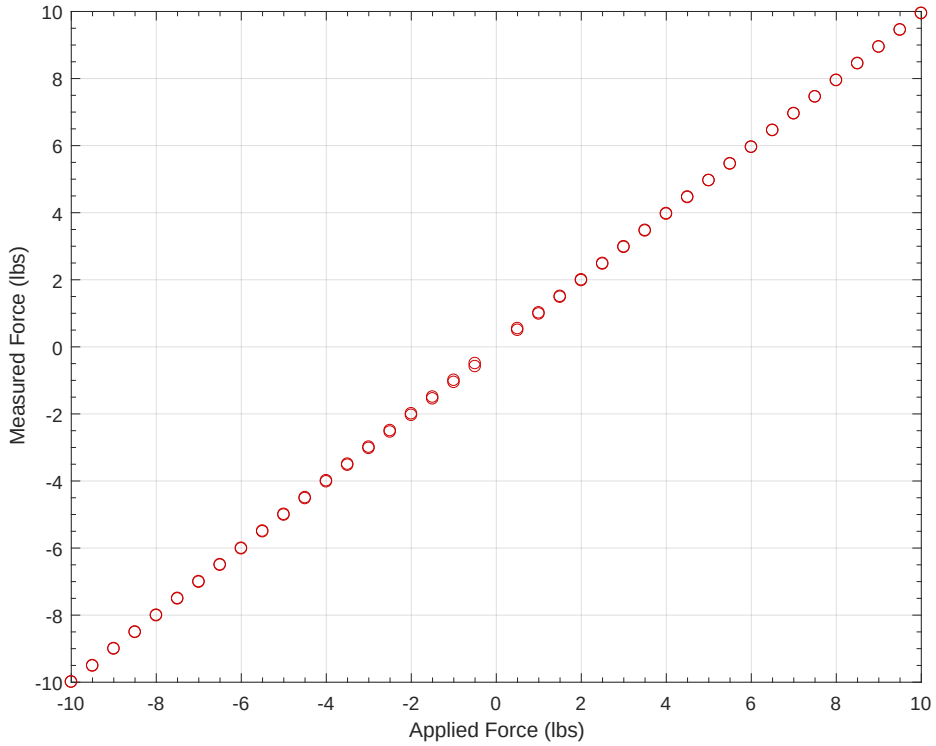

Figure B.2. Fine Assessment of Measured Horizontal Forces (F_x) vs. Applied Forces

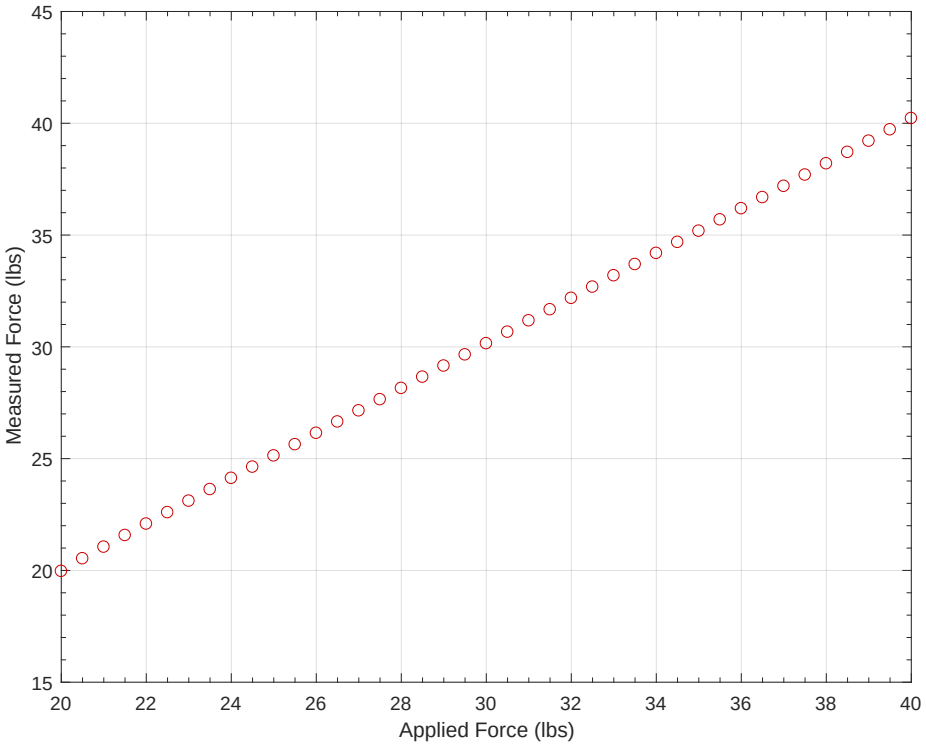

Figure B.3. Fine Assessment of Measured Vertical Forces (F_z) vs. Applied Forces

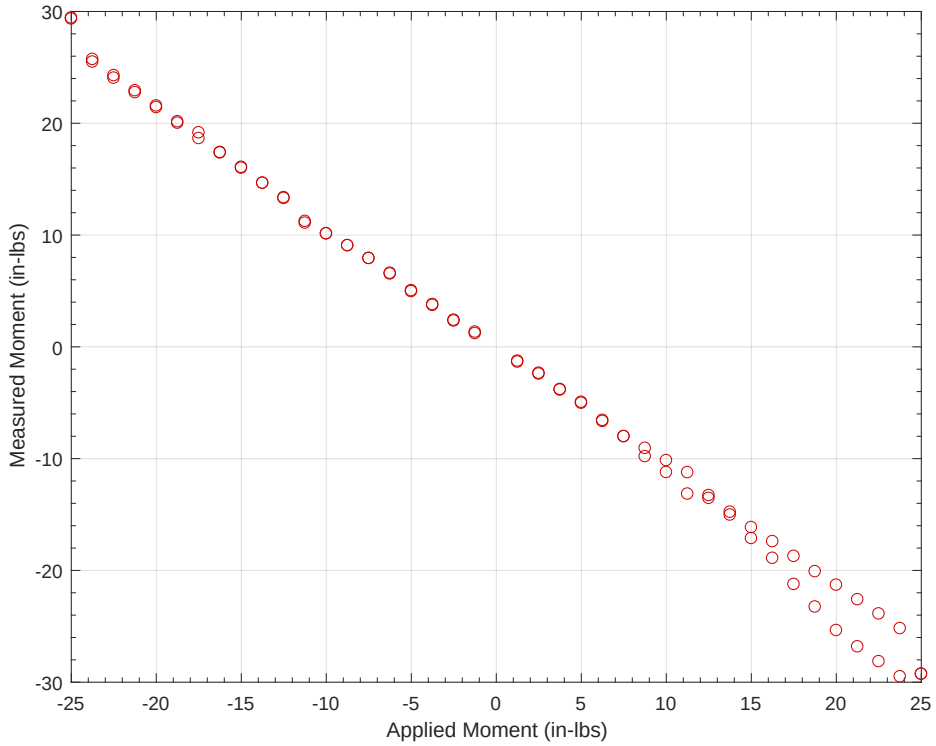

Figure B.4. Fine Assessment of Measured Pitch Moment (M_y) vs. Applied Moments

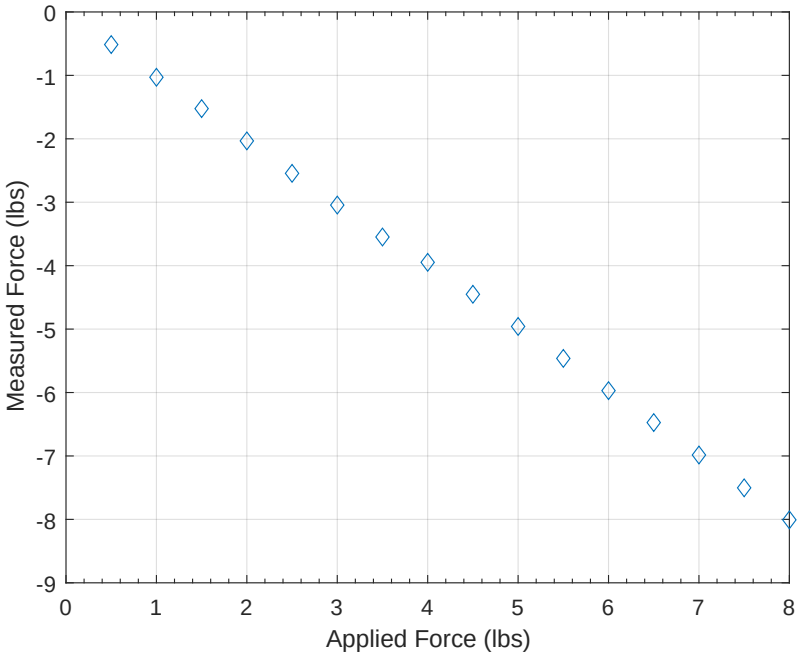

Figure B.5. Measured Vertical Forces (F_z) vs. Applied Forces

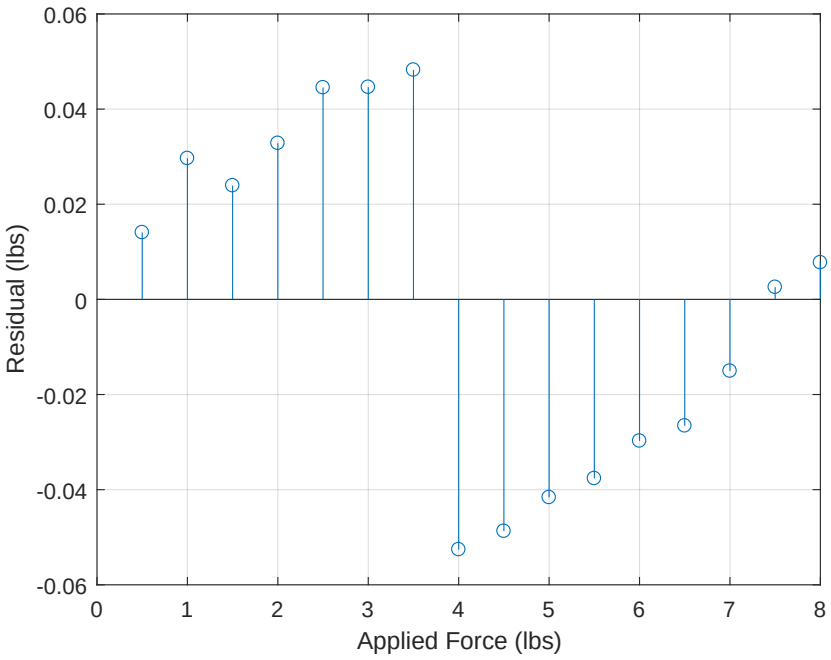

Figure B.6. Measured Vertical Force Residuals (F_z) vs. Applied Forces

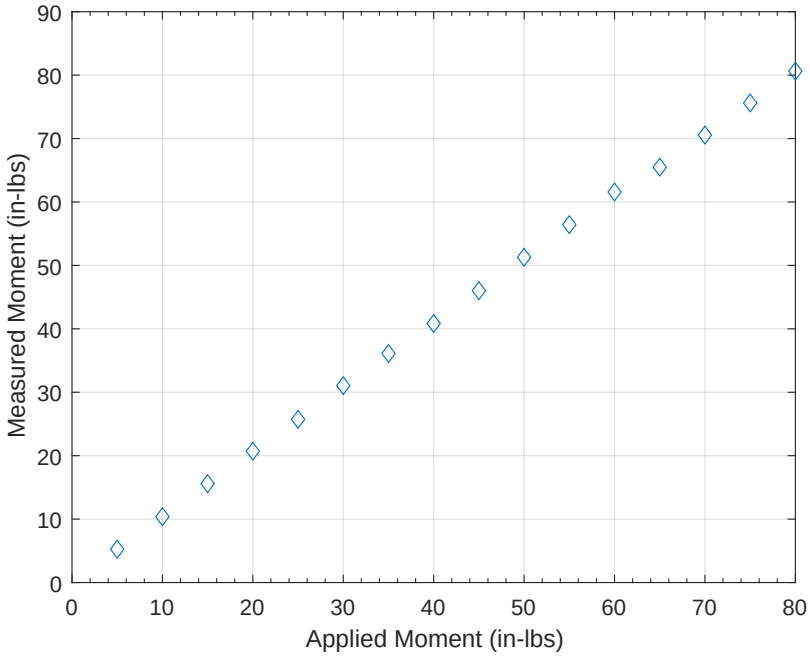

Figure B.7. Measured Moments (M_y) vs. Applied Moments with 10-inch Moment Arm

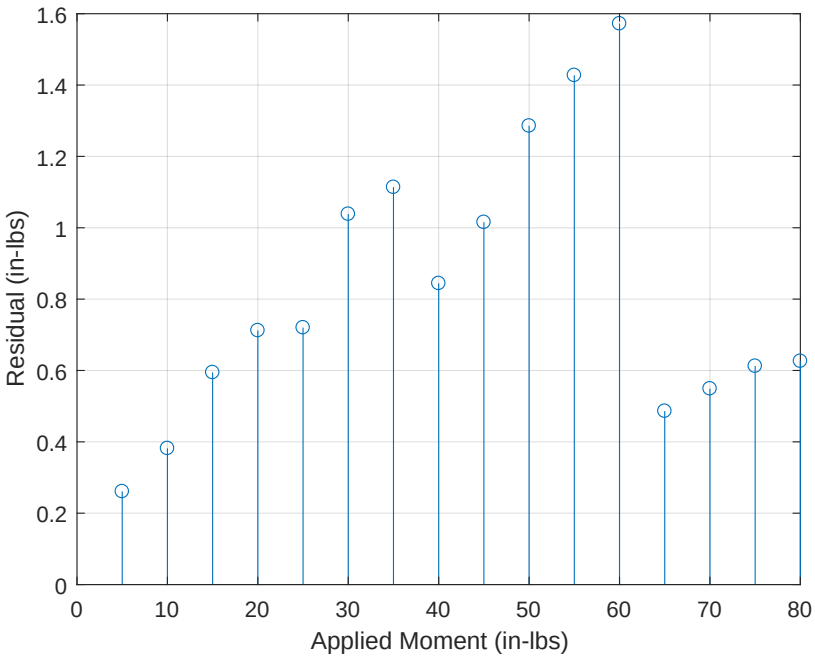

Figure B.8. Measured Moment Residuals (M_y) vs. Applied Moments with 10-inch Moment Arm

APPENDIX C:
Curve-Fitting Function

```
function Coefficients = CurveFitSingle(data, f, x, k)
    % This function takes a single time-history of a sinusoidal data set
    % and a corresponding frequency array. From those matrices it
    % determines the component amplitudes and non-zero offset.
    % Developed by LT Travis Turner, October 2017, with assistance and
    % guidance from Dr. Joseph Klamo.
    %
    % eta(x,t) = A1 cos(k1 x - omega1 t) + B1 sin(k1 x - omega1 t) +
    %            A2 cos(k2 x - omega2 t) + B2 sin(k2 x - omega2 t) +
    %            .... + C
    %
    % OUTPUT:
    % Coefficients(1) = A1
    % Coefficients(2) = B1
    % Coefficients(3) = A2
    % Coefficients(4) = B2
    % ....
    % Coefficients(2*length(f)+1) = C
    %
    % UPDATED
    % 2017-10-24
    % 1) fixed formula for k
    % 2) made k an input instead of an internal calculation; this allows
    % for k to be based on a corrected non-deep water wavelength
    % 2017-10-25
    % 1) fixed input checks
    % 2) cleaned notation to improve readability

    % Check inputs to ensure they do not exceed the input parameters.
    if (size(data,2) > 2)
        fprintf('The data array has too many columns. This function accepts a Nx2 data arr
ay.\n')
        return
    else
    end

    if (length(f) > length(k))
        fprintf('The arrays for frequency and k must be the same length.\n')
        return
    else
    end

    if (length(x) > 1)
        fprintf('The x input should be a single value.\n')
        return
    else
    end

    % input arguments
    t = data(:,1);
    w = 2*pi.*f;
    %k = 4*(pi^2).*(f.^2)./(32.174*12);

    % define the size of the M matrix
    M = zeros(2*length(w)+1,2*length(w)+1);
```

Figure C.1. Sinusoidal Curve-Fitting Function, Page 1

```
    % fill in the main part of the M vector
    for i = 1:length(w)
        for j = 1:length(w)
            M(2*i-1,2*j-1) = sum(cos(k(j).*x-w(j).*t).*cos(k(i).*x-w(i).*t));
            M(2*i-1,2*j) = sum(sin(k(j).*x-w(j).*t).*cos(k(i).*x-w(i).*t));
            M(2*i,2*j-1) = sum(cos(k(j).*x-w(j).*t).*sin(k(i).*x-w(i).*t));
            M(2*i,2*j) = sum(sin(k(j).*x-w(j).*t).*sin(k(i).*x-w(i).*t));
        end

            % this is the far right column
            M(2*i-1,2*length(w)+1) = sum(cos(k(i).*x-w(i).*t));
            M(2*i,2*length(w)+1) = sum(sin(k(i).*x-w(i).*t));
    end

    % fill in the bottom row
    i = 2*length(w)+1;
    for j = 1:length(w)
        M(i,2*j-1) = sum(cos(k(j).*x-w(j).*t));
        M(i,2*j) = sum(sin(k(j).*x-w(j).*t));
    end

    % fill in the bottom right corner
    M(i,2*length(w)+1) = size(data,1);

    % build the psi matrix
    Psi = zeros(2*length(w)+1,1);
    for i = 1:length(w)
        Psi(2*i-1) = sum(data(:,2).*cos(k(i).*x-w(i).*t));
        Psi(2*i) = sum(data(:,2).*sin(k(i).*x-w(i).*t));
    end

    Psi(2*length(w)+1) = sum(data(:,2));

    Coefficients = M\Psi;
end
```

Figure C.2. Sinusoidal Curve-Fitting Function, Page 2

APPENDIX D:
Test Matrix

Table D.1. Test Matrix of Commanded Frequencies and Wedge Amplitudes

λ/L	Frequency (Hz)	Wedge Command (mm)
0.5000	1.653	37.000
0.5313	1.603	38.750
0.5625	1.558	39.500
0.5938	1.517	40.500
0.6250	1.478	41.750
0.6563	1.442	42.750
0.6875	1.409	44.000
0.7188	1.378	46.000
0.7500	1.349	46.250
0.7813	1.322	44.500
0.8125	1.296	46.000
0.8438	1.272	48.500
0.8750	1.249	49.000
0.9063	1.227	53.000
0.9375	1.207	48.500
0.9688	1.187	53.250
1.0000	1.168	53.500
1.0313	1.151	54.000
1.0625	1.134	54.000
1.0938	1.117	57.000
1.1250	1.102	57.250
1.1875	1.072	59.500
1.2500	1.045	59.500
1.3125	1.020	62.750
1.3750	0.996	65.000
1.4375	0.974	66.500
1.5000	0.953	68.000
1.6250	0.915	73.000
1.7500	0.881	78.500
1.8750	0.849	85.000
2.0000	0.821	86.500

THIS PAGE INTENTIONALLY LEFT BLANK

APPENDIX E:
Run Duration Analysis

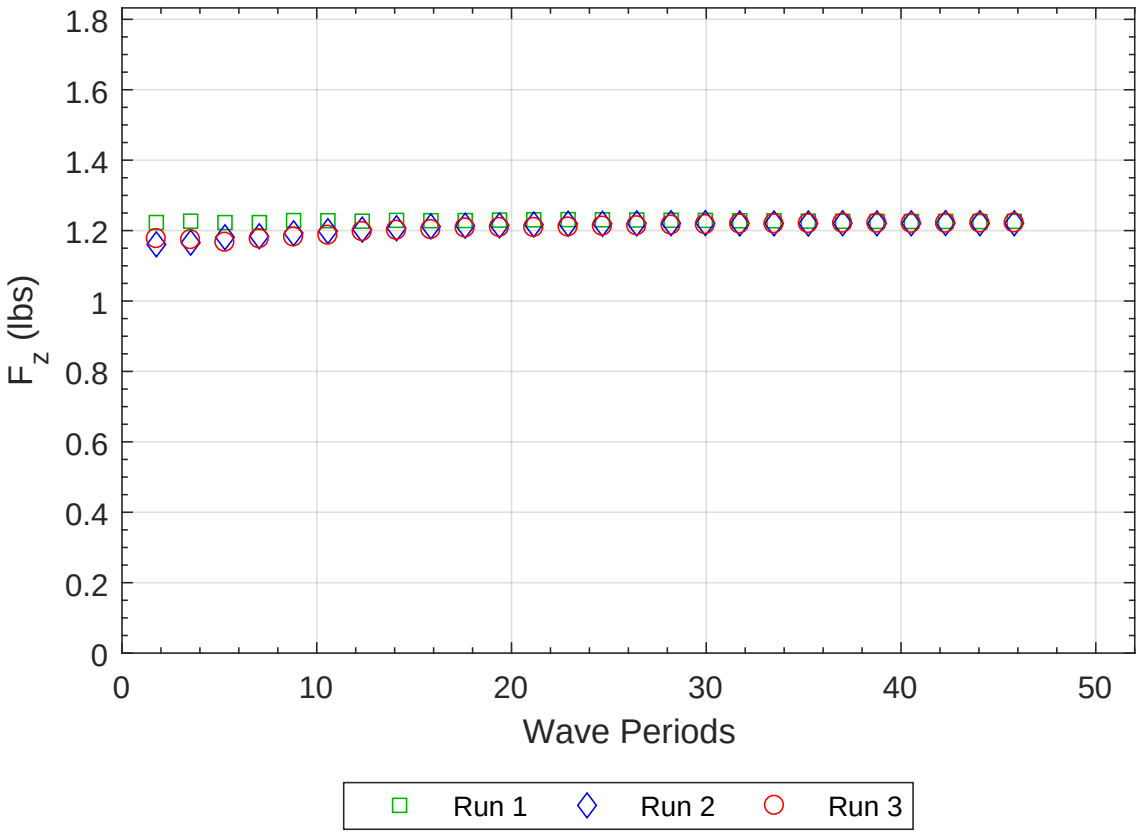

Figure E.1. Vertical Forces Evaluated as a Function of Measured Wave Cycles, $\lambda/L = 1.75$ and $d/D = 2$

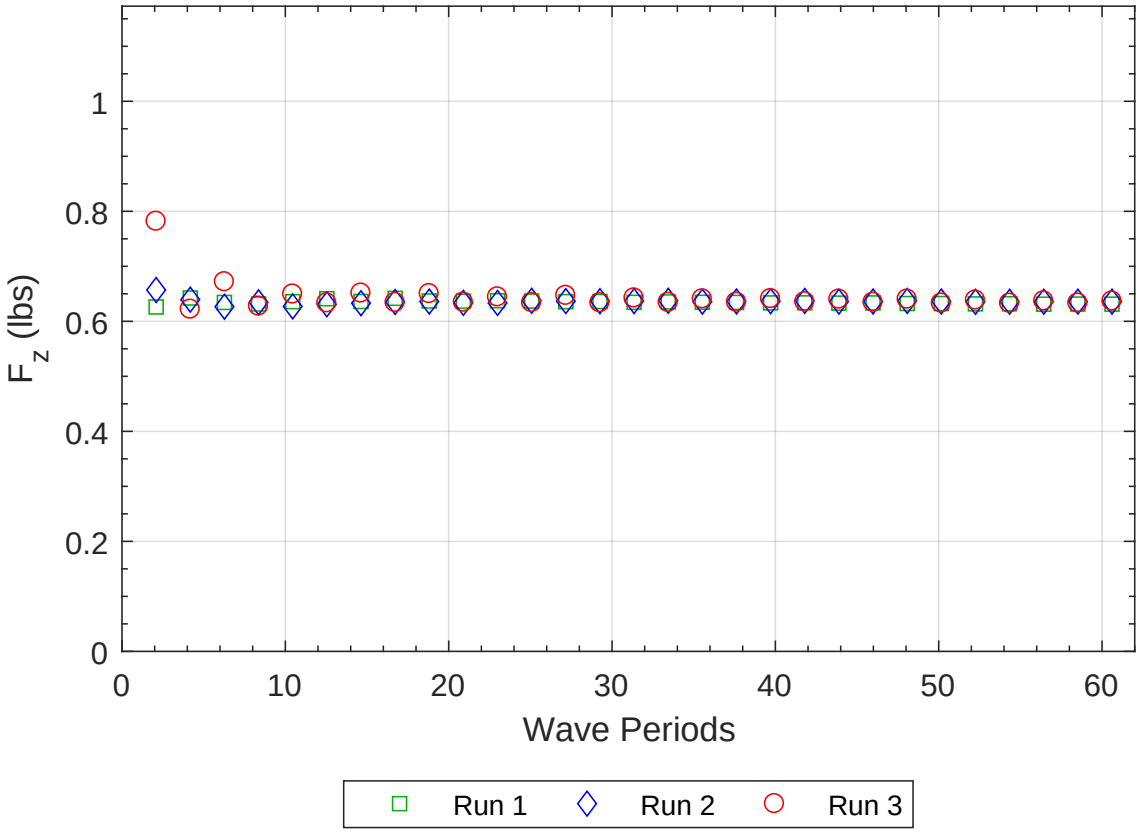

Figure E.2. Vertical Force Evaluated as a Function of Measured Wave Cycles, $\lambda/L = 1.25$ and $d/D = 2$

APPENDIX F:
Summary Data - Shape Comparisons

Coefficients for the curve fits seen in this Appendix are given in Appendix H and are of the forms shown in Equations 7.1 and 7.2.

F.1 Longitudinal Forces

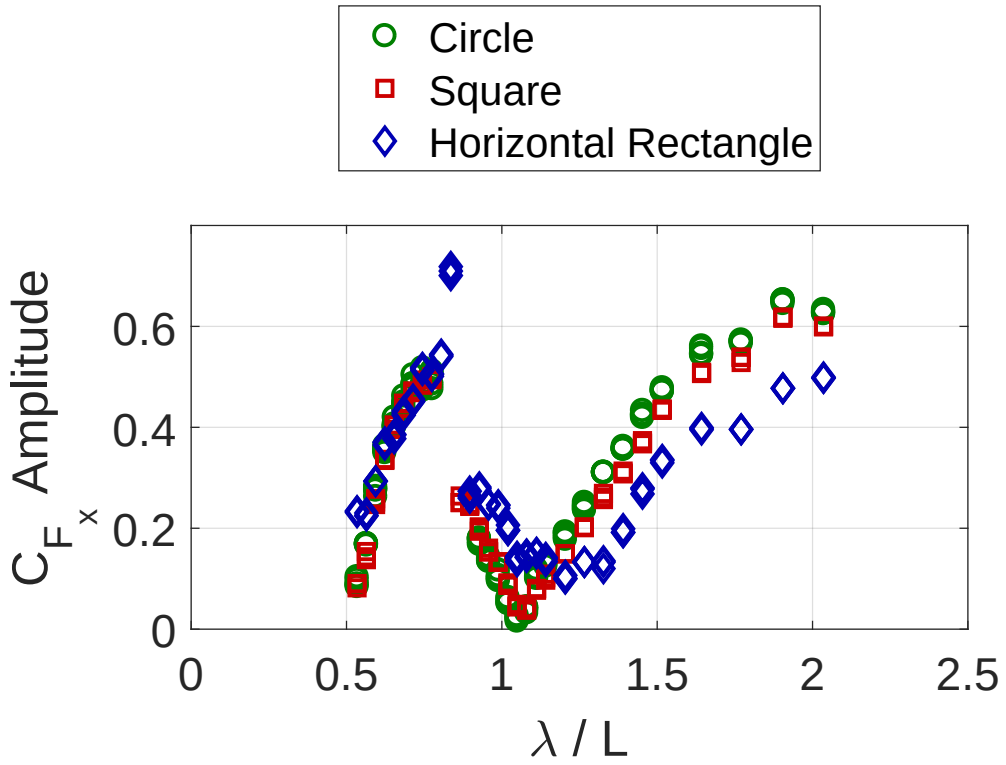

Figure F.1. Non-dimensional Longitudinal Forces, $d/D = 1.0$

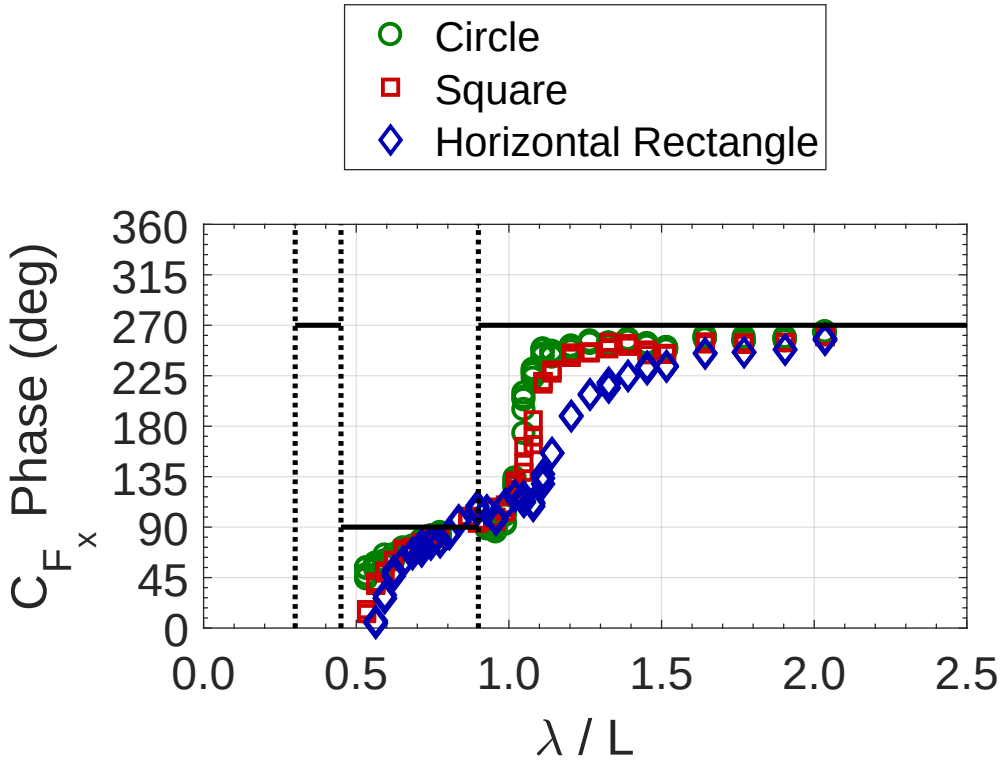

Figure F.2. F_x Phase Relative to Incoming Wave, $d/D = 1.0$

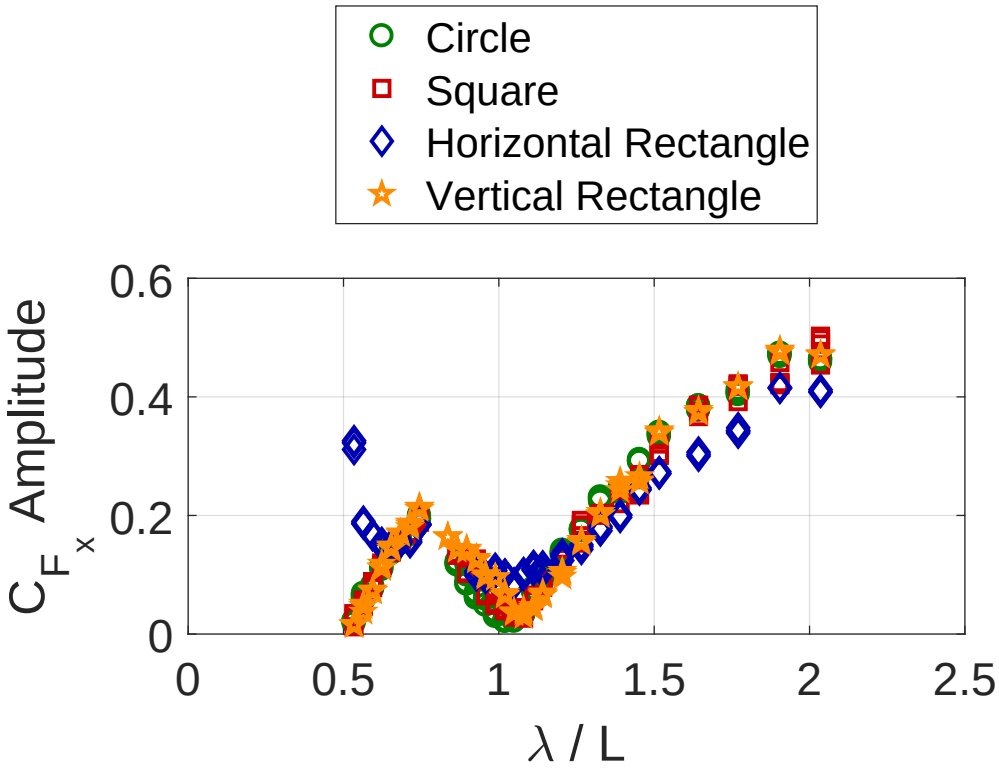

Figure F.3. Non-dimensional Longitudinal Forces, $d/D = 2.0$

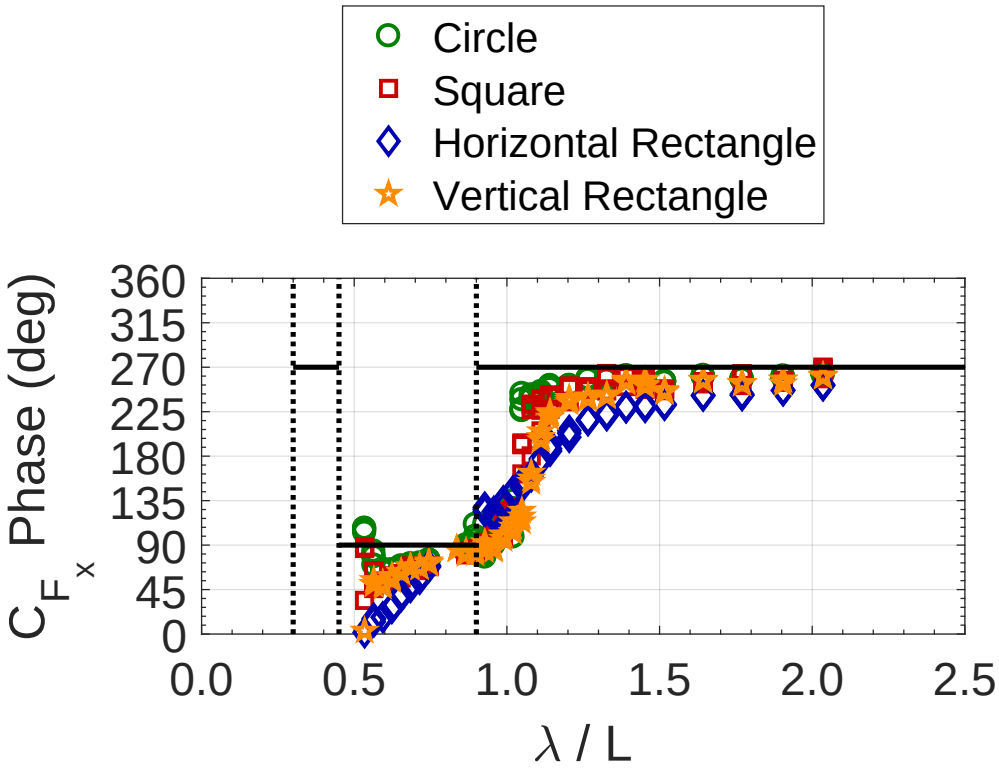

Figure F.4. F_x Phase Relative to Incoming Wave, $d/D = 2.0$

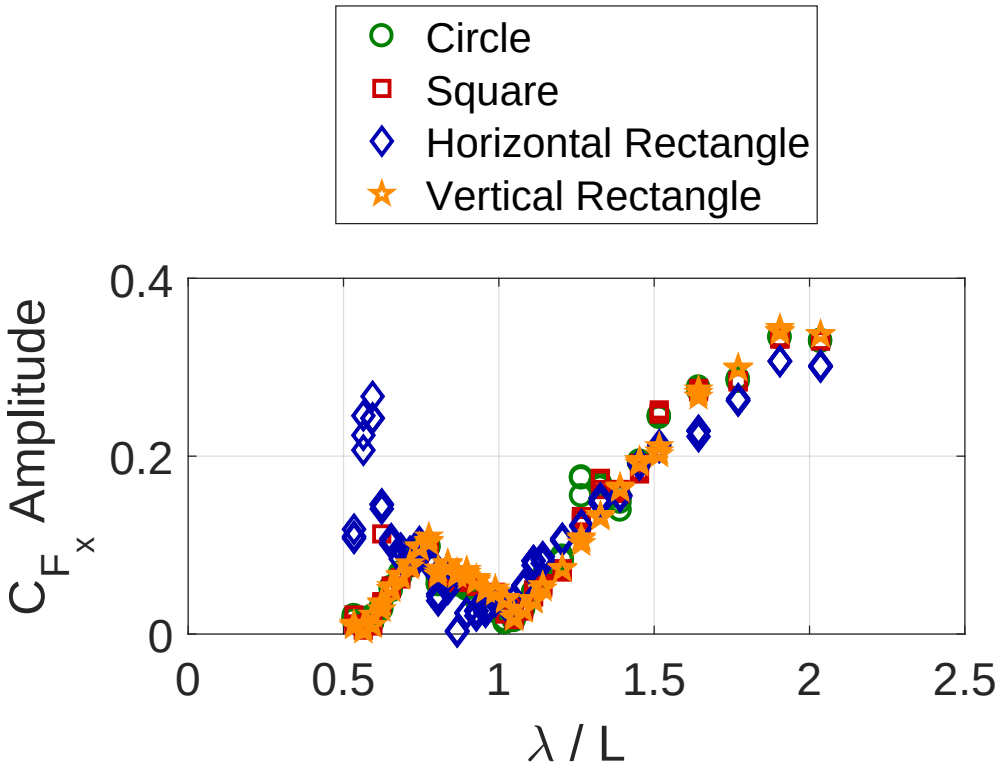

Figure F.5. Non-dimensional Longitudinal Forces, $d/D = 3.0$

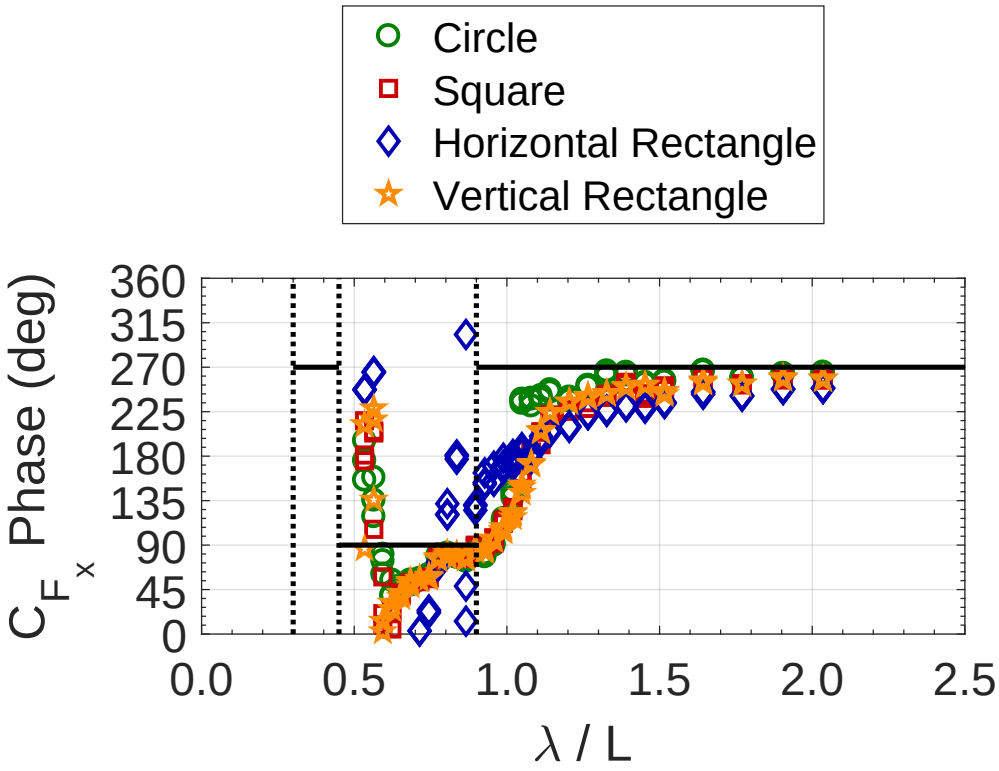

Figure F.6. F_x Phase Relative to Incoming Wave, $d/D = 3.0$

F.2 Vertical Forces

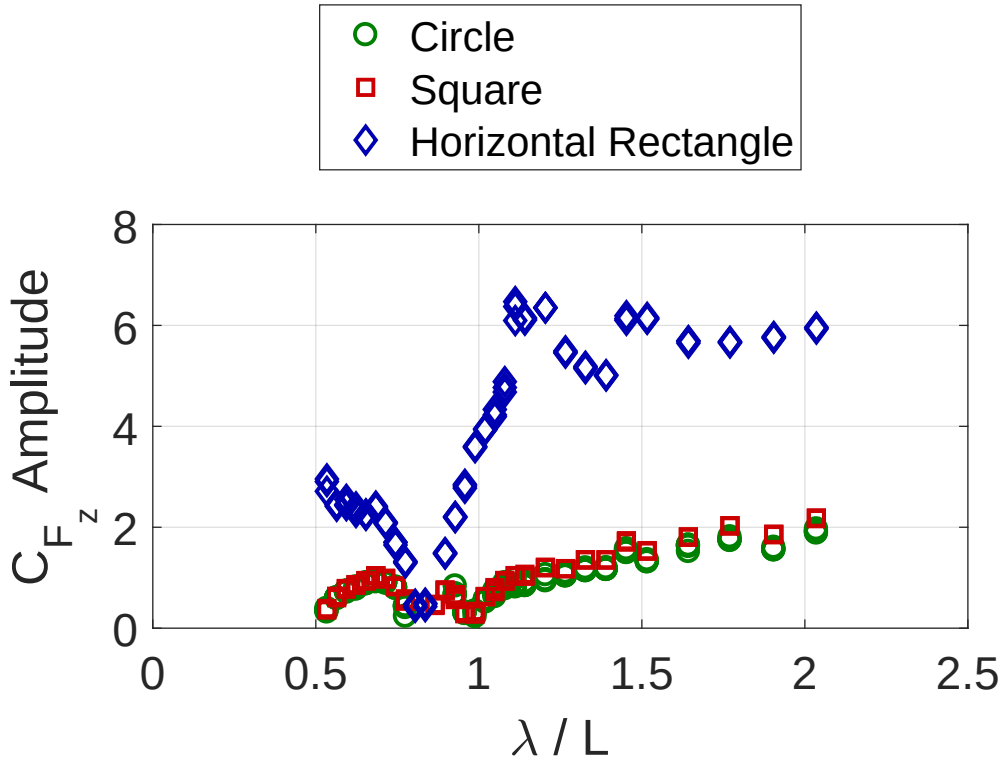

Figure F.7. Non-dimensional Vertical Forces, $d/D = 1.0$

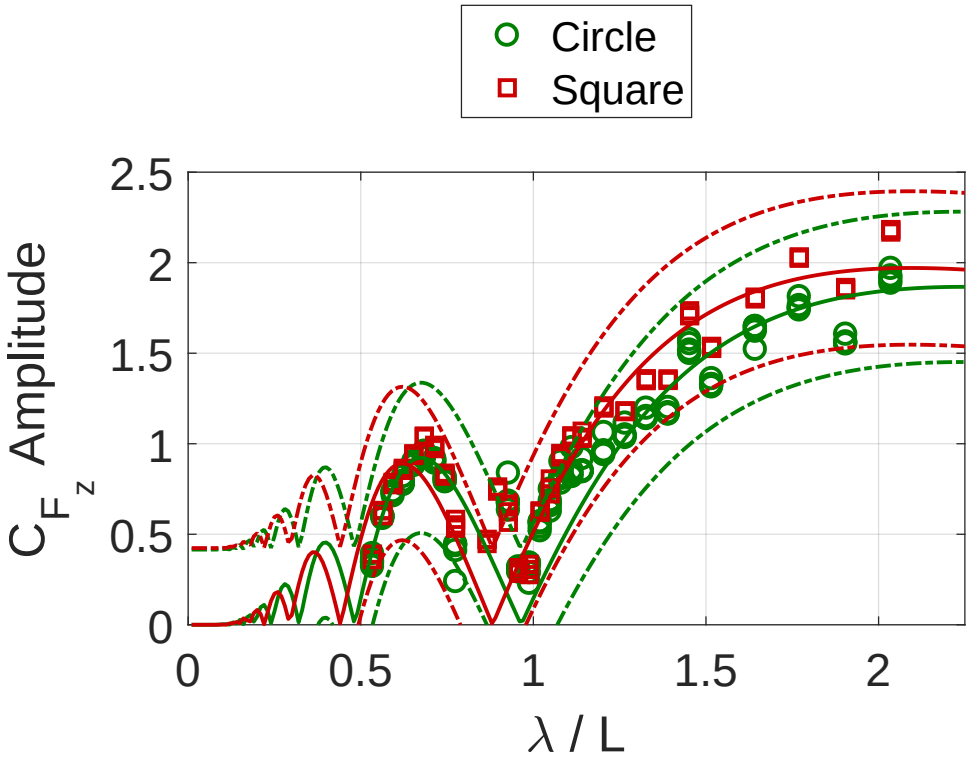

Figure F.8. Select Non-dimensional Vertical Forces with Curve Fits, $d/D = 1.0$

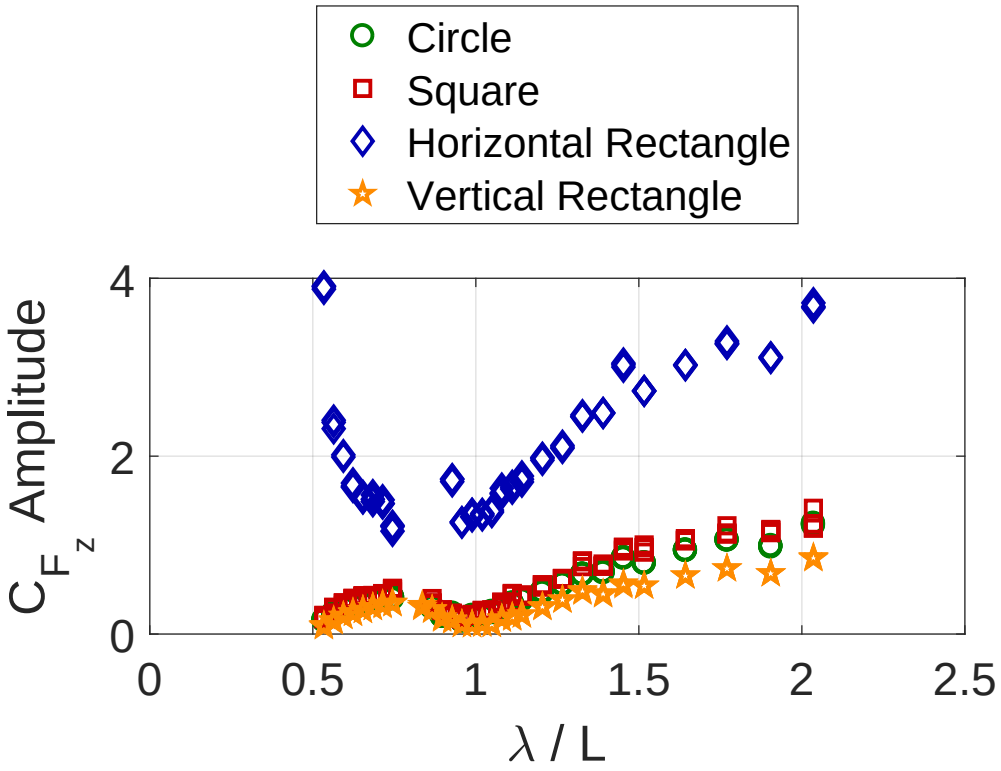

Figure F.9. Non-dimensional Vertical Forces, $d/D = 2.0$

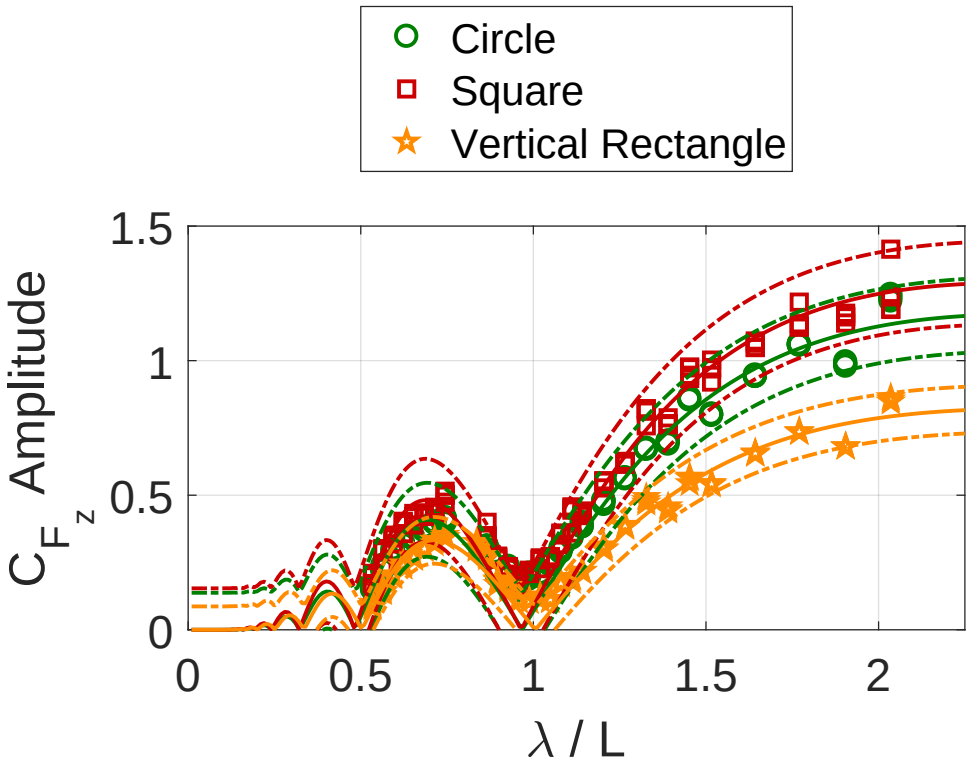

Figure F.10. Select Non-dimensional Vertical Forces with Curve Fits, d/D = 2.0

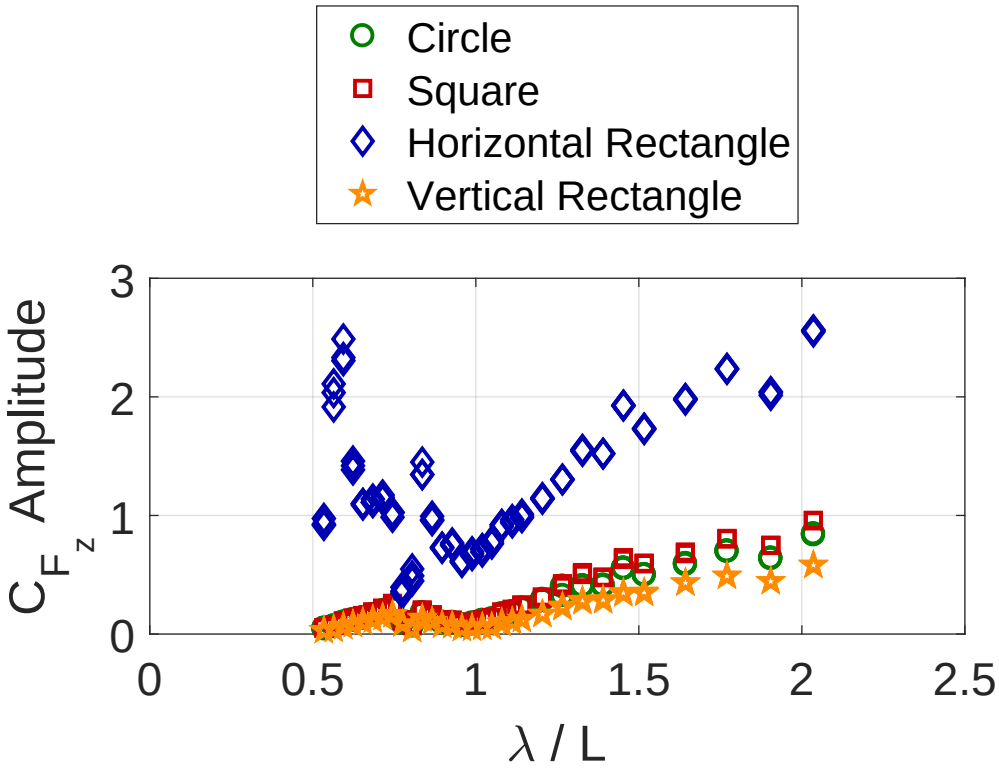

Figure F.11. Non-dimensional Vertical Forces, $d/D = 3.0$

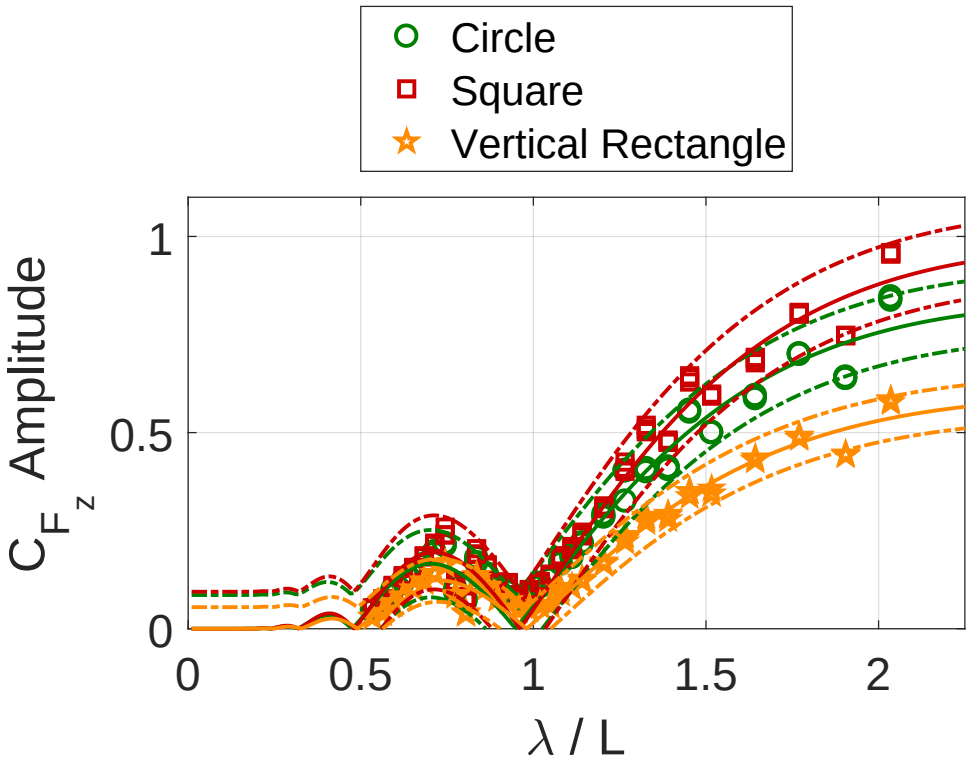

Figure F.12. Select Non-dimensional Vertical Forces with Curve Fits, d/D = 3.0

F.3 Pitch Moments

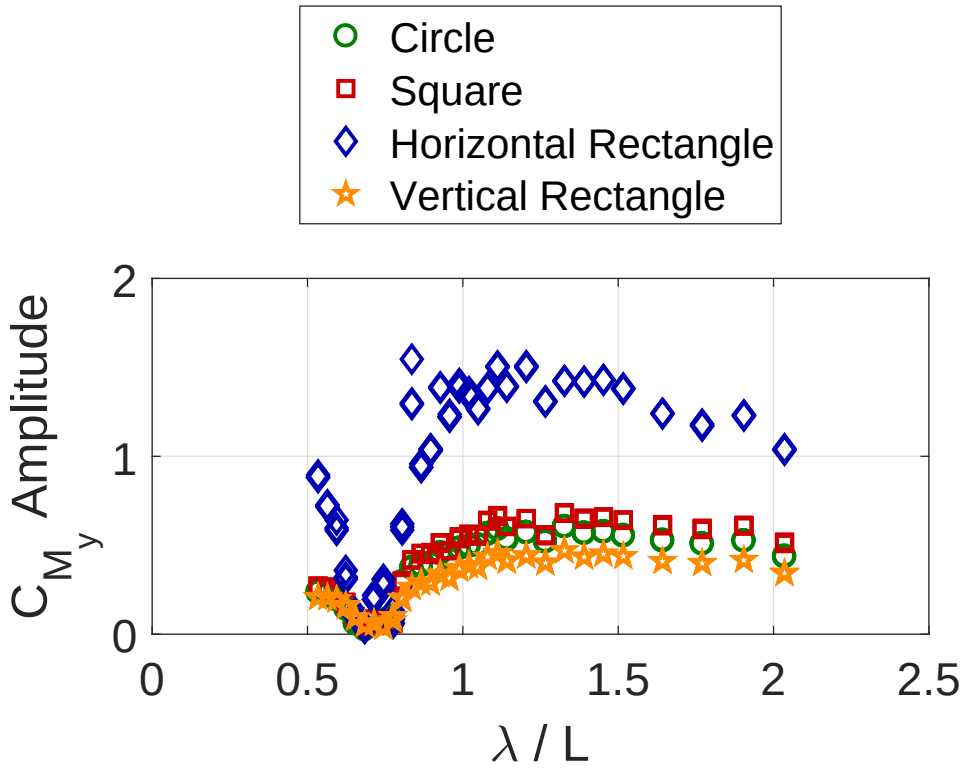

Figure F.13. Non-dimensional Pitch Moments, $d/D = 1.5$

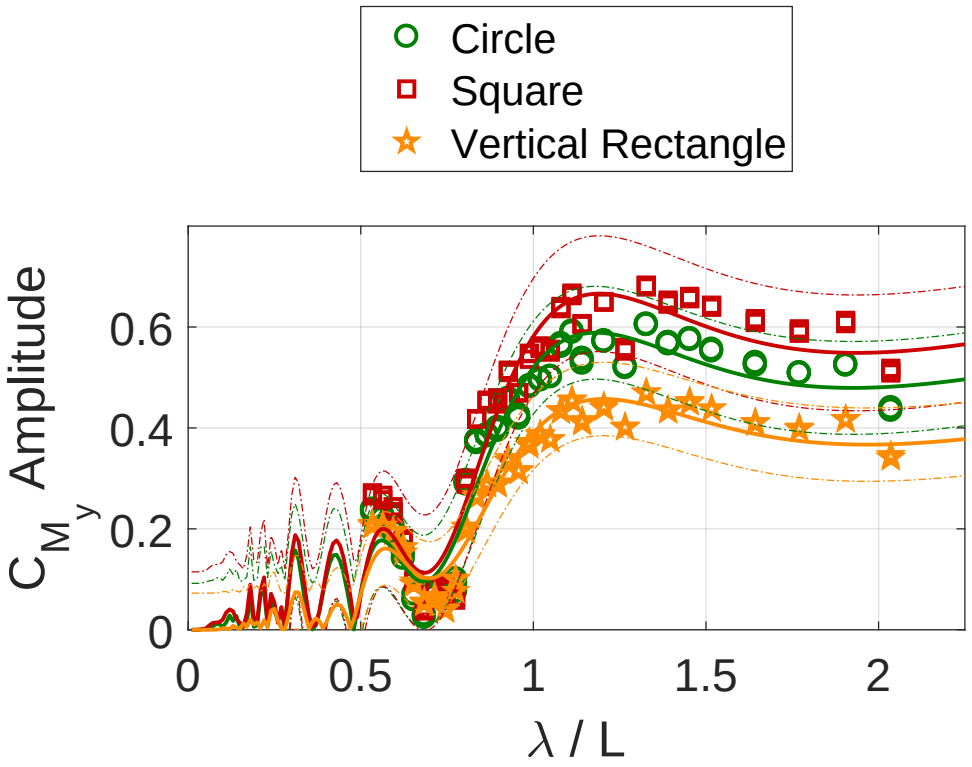

Figure F.14. Select Non-dimensional Pitch Moments with Curve Fits, d/D = 1.5

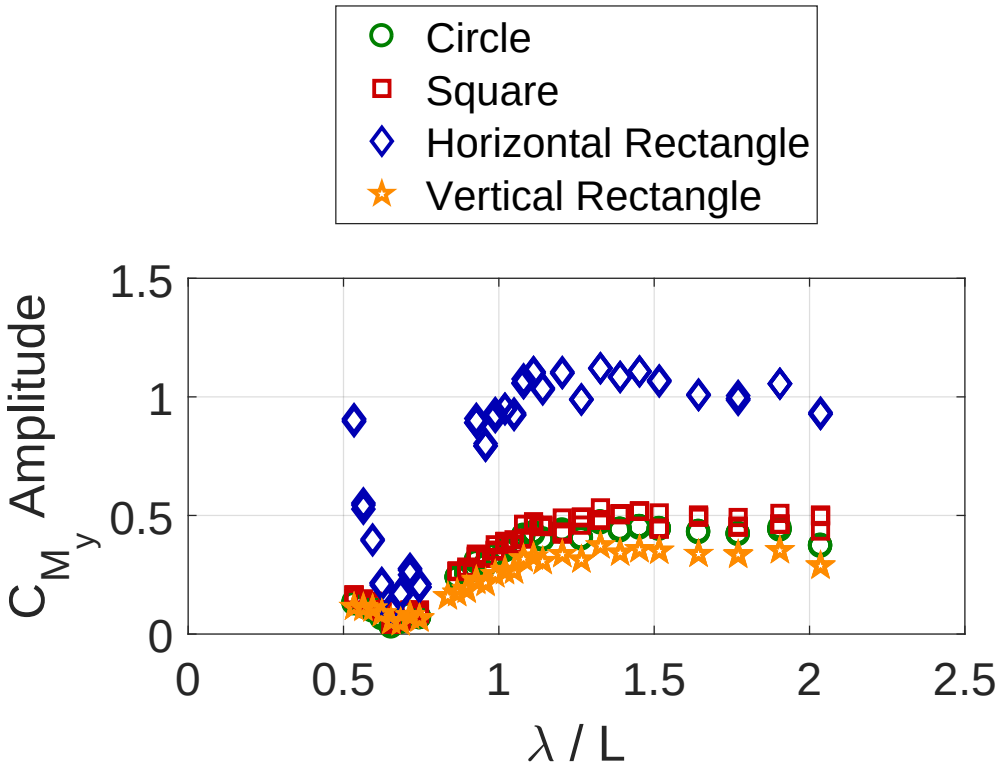

Figure F.15. Non-dimensional Pitch Moments, $d/D = 2.0$

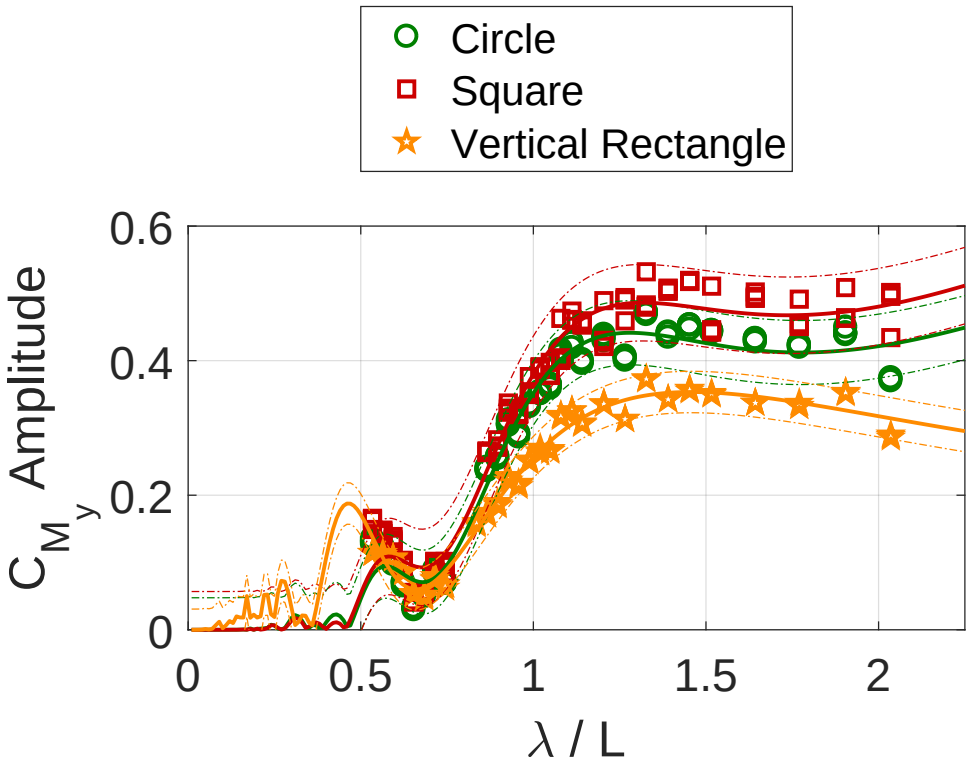

Figure F.16. Select Non-dimensional Pitch Moments with Curve Fits, d/D = 2.0

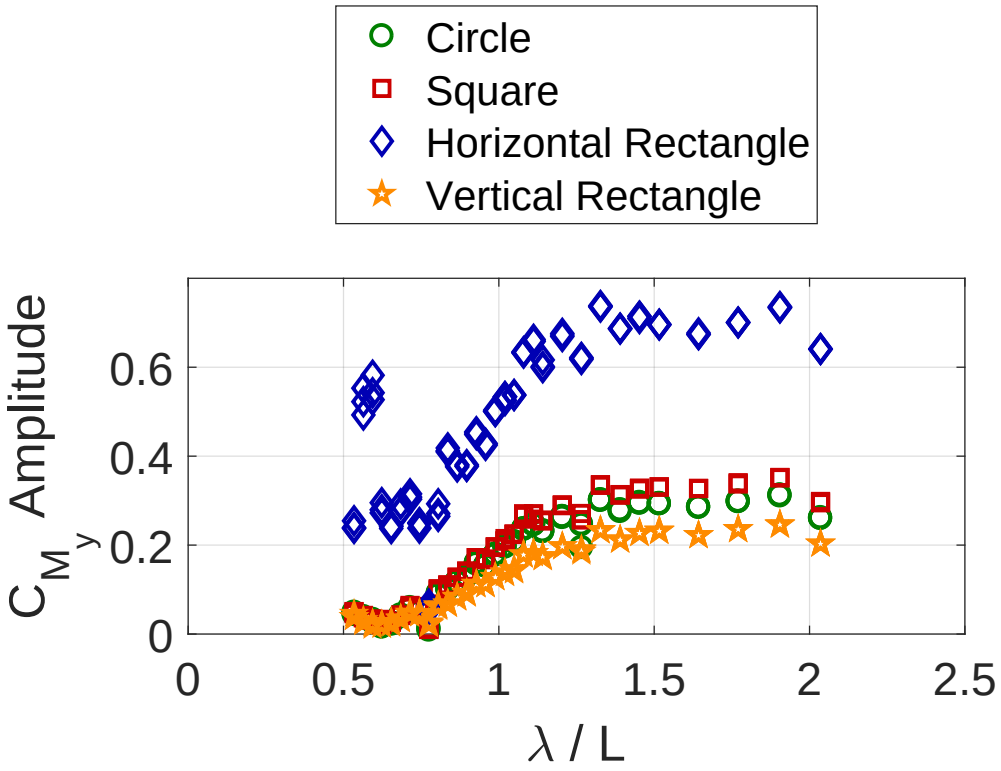

Figure F.17. Non-dimensional Pitch Moments, $d/D = 3.0$

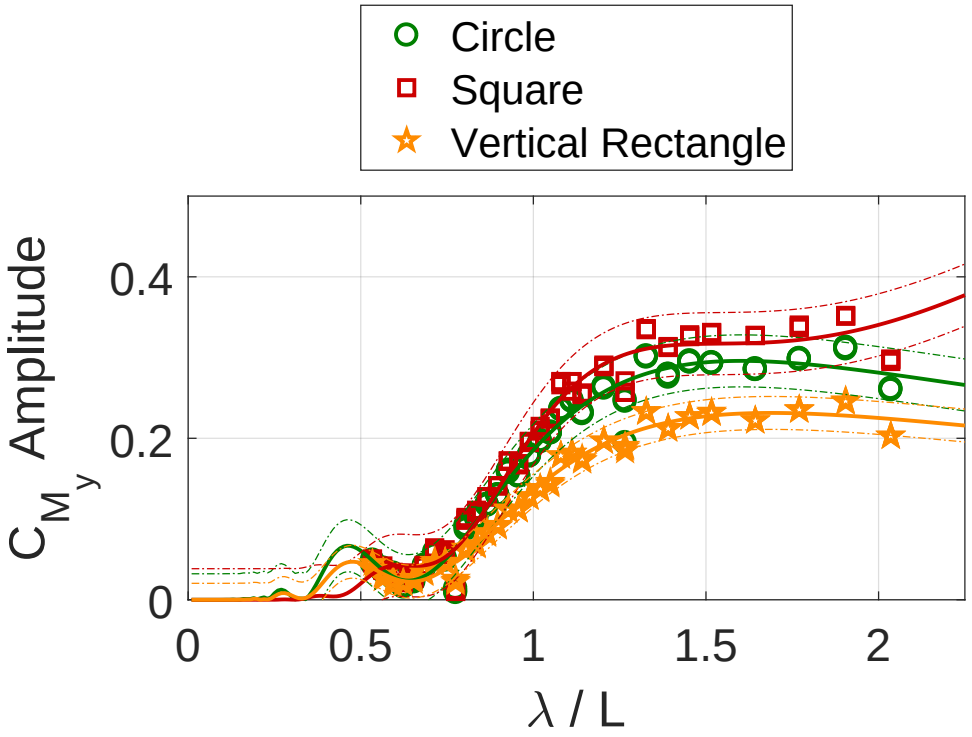

Figure F.18. Select Non-dimensional Pitch Moments with Curve Fits, d/D = 3.0

APPENDIX G:
Summary Data - Depth Comparisons

G.1 Vertical Forces

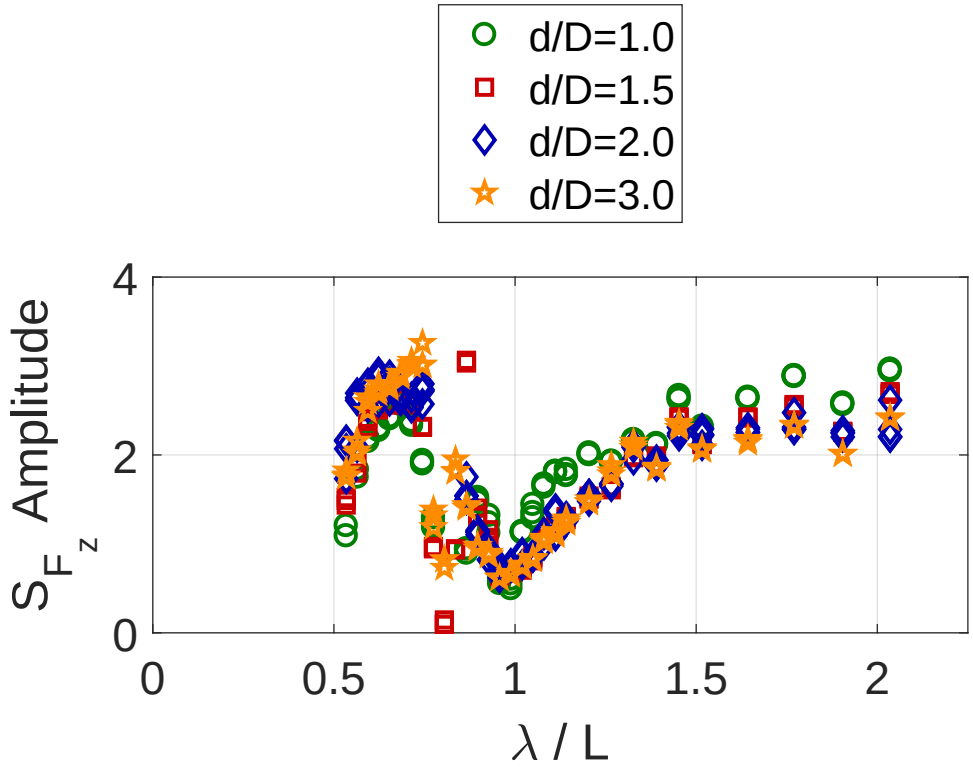

Figure G.1. Non-dimensional Vertical Forces, Square Model

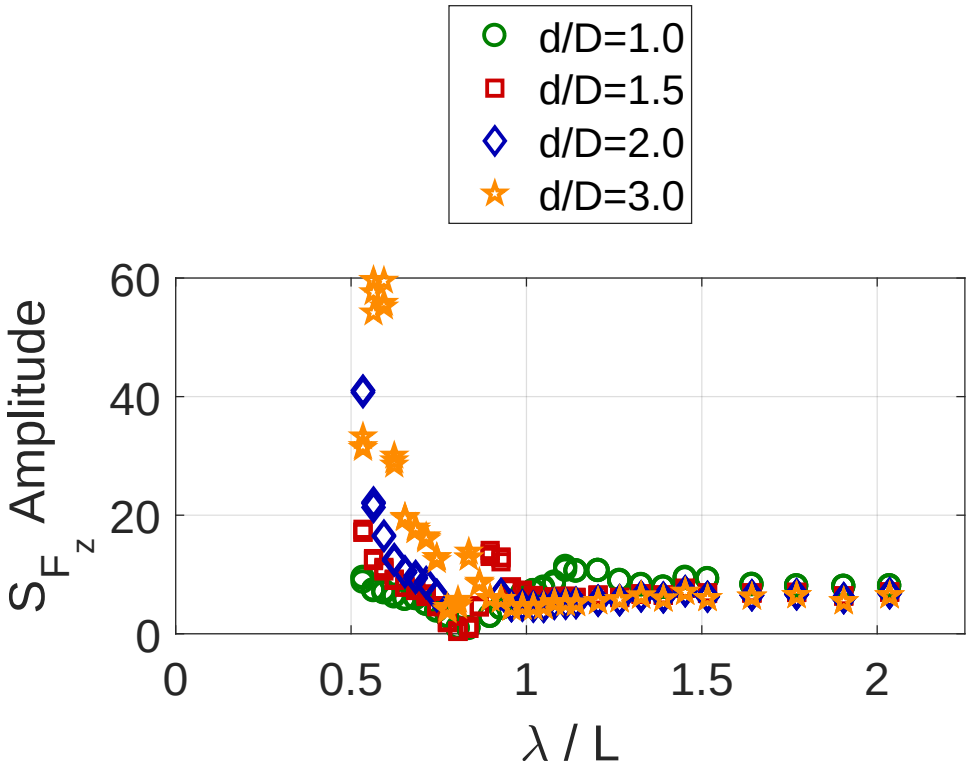

Figure G.2. Non-dimensional Vertical Forces, Rectangular Model (Horizontal Orientation)

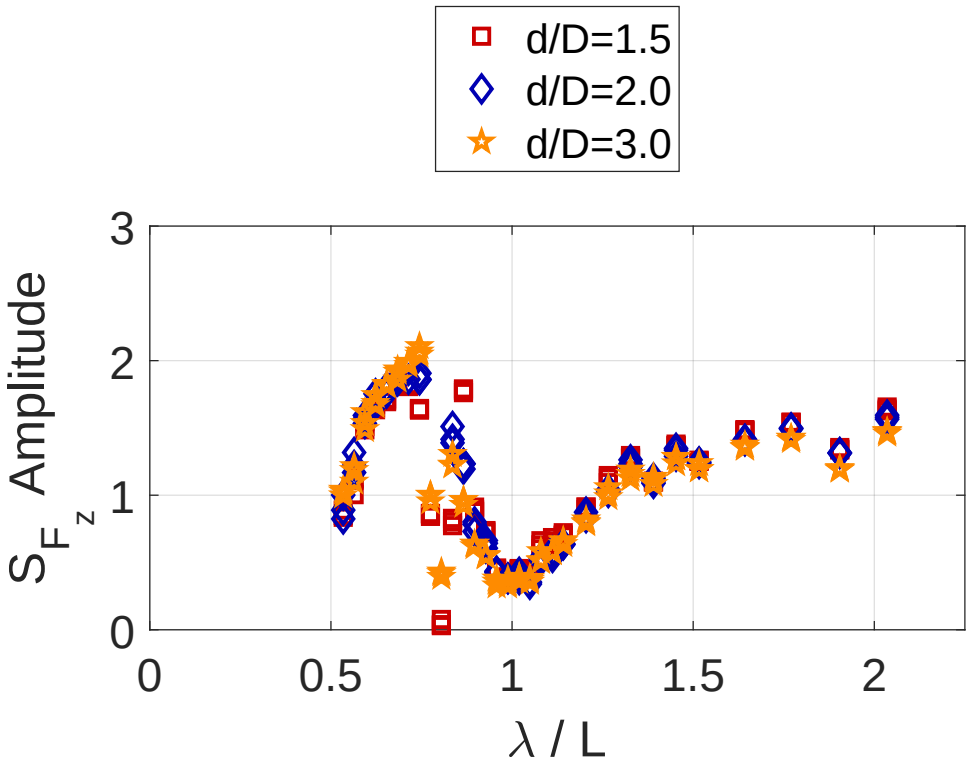

Figure G.3. Non-dimensional Vertical Forces, Rectangular Model (Vertical Orientation)

G.2 Pitch Moments

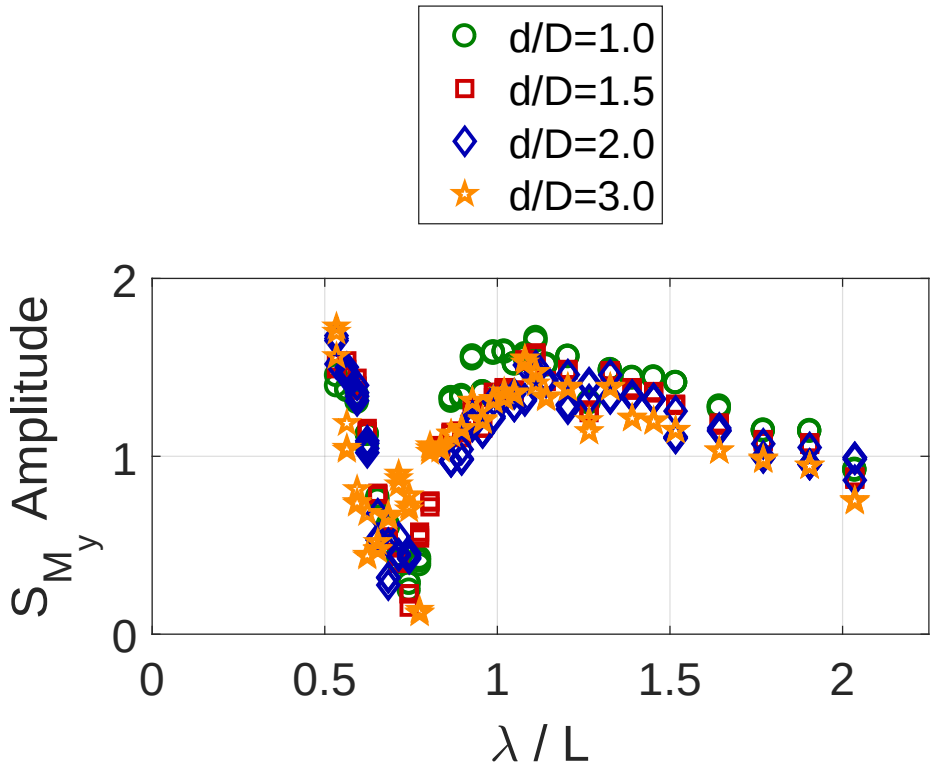

Figure G.4. Non-dimensional Pitch Moments, Square Model

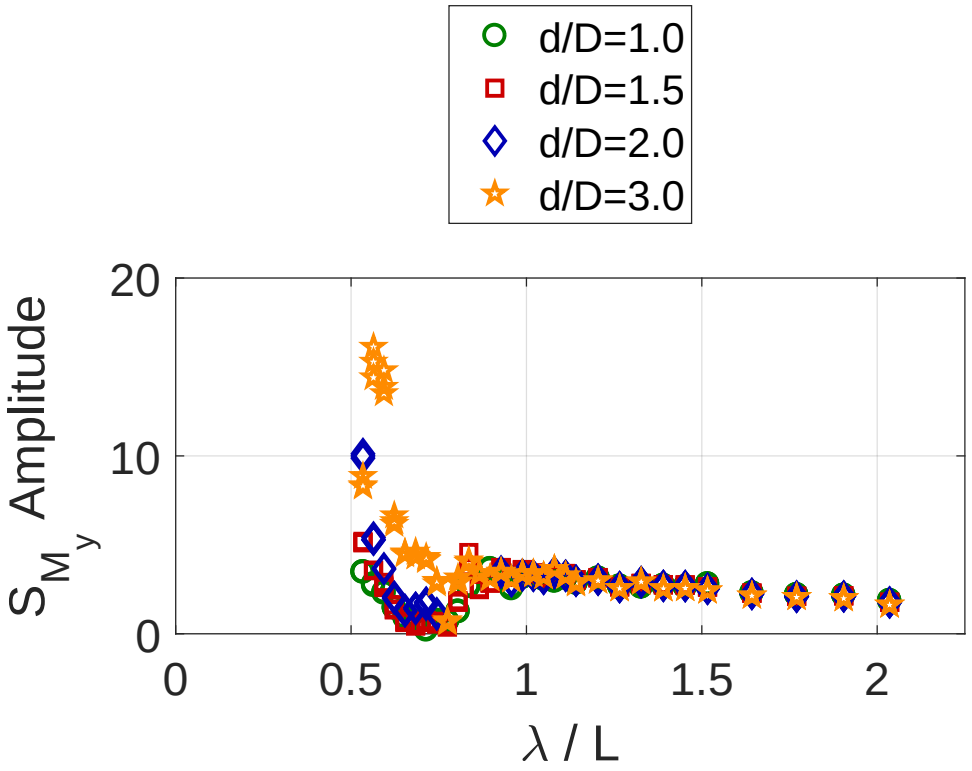

Figure G.5. Non-dimensional Pitch Moments, Rectangular Model (Horizontal Orientation)

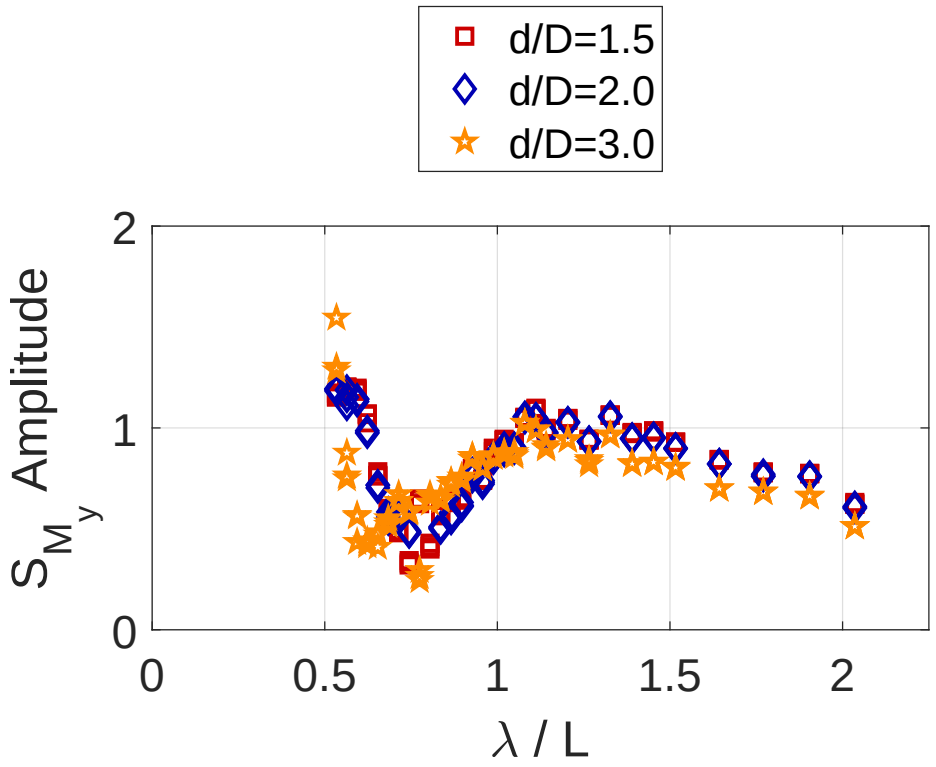

Figure G.6. Non-dimensional Pitch Moments, Rectangular Model (Vertical Orientation)

APPENDIX H:
Curve-Fit Coefficients

Table H.1. Non-dimensional Vertical Force Curve-Fit Coefficients

d/D	Cross-Sectional Shape	A	B	C
1.0	Circle	-2.59	3.03	-0.68
1.0	Square	-2.84	2.77	-0.70
1.5	Circle	-2.10	3.05	-0.86
1.5	Square	-2.51	3.06	-0.91
1.5	Vertical Rectangle	-1.43	3.12	-0.80
2.0	Circle	-1.88	3.04	-1.02
2.0	Square	-2.01	3.03	-0.95
2.0	Vertical Rectangle	-1.24	3.16	-0.91
3.0	Circle	-1.62	2.98	-1.52
3.0	Square	-1.90	3.02	-1.54
3.0	Vertical Rectangle	-1.14	3.08	-1.53

Table H.2. Non-dimensional Pitch Moment Curve-Fit Coefficients

d/D	Cross-Sectional Shape	A	B	C	D	E
1.0	Circle	0.41	1.69	0.36	6.80	0.41
1.0	Square	0.47	1.67	0.33	6.77	0.38
1.5	Circle	0.50	1.52	0.32	6.77	-0.21
1.5	Square	0.55	1.54	0.31	6.82	-0.18
1.5	Vertical Rectangle	0.48	1.33	0.31	6.90	-0.41
2.0	Circle	0.71	1.32	0.30	6.79	-0.91
2.0	Square	0.88	1.22	0.26	6.83	-0.99
2.0	Vertical Rectangle	0.38	0.76	-0.38	4.25	-0.24
3.0	Circle	0.57	0.60	-0.36	4.11	-0.86
3.0	Square	1.78	0.72	0.20	6.84	-1.97
3.0	Vertical Rectangle	0.58	0.50	-0.28	4.18	-0.98

THIS PAGE INTENTIONALLY LEFT BLANK

List of References

Advanced Mechanical Technology Incorporated. 2000. *Dynamometer Instructions: Single Element Multi-Component Dynamometer*. Watertown, MA: Advanced Mechanical Technology Incorporated.

Alvarez, A., V. Bertram, and L. Gualdesi. 2009. "Hull Hydrodynamic Optimization of Autonomous Underwater Vehicles Operating at Snorkeling Depth." *Ocean Engineering* 36:105–112.

Ananthakrishnan, P., and K-Q. Zhang. 1998. "AUV Motion in a Wave Field." In *IEEE Oceans '98 Conference*, 1059–1063. Nice, France: Institute of Electrical and Electronics Engineers.

Atkinson, Kendall. 1985. *Elementary Numerical Analysis*. 2nd ed. New York: John Wiley and Sons, Inc.

Cummins, W. E. 1953. *The Forces and Moments Acting on a Body Moving in an Arbitrary Potential Stream*. Technical Report 780. West Bethesda, MD: David Taylor Model Basin.

———. 1954a. *Forces and Moments Acting on a Submarine Moving Under Waves - Comparison of Theory with Experiment*. Technical Report 596. West Bethesda, MD: David Taylor Model Basin.

———. 1954b. *Hydrodynamic Forces and Moments Acting on a Slender Body of Revolution Moving Under a Regular Train of Waves*. Technical Report 910. West Bethesda, MD: David Taylor Model Basin.

———. 1961. *Preliminary Note on the Surface Suction Force Acting on a Submarine Hovering Under Waves*. Technical Report 033445. West Bethesda, MD: David Taylor Model Basin.

Jane's by IHS Markit. 2018. "REMUS 100." January 8, 2018. https://janes.ihs.com.libproxy.nps.edu/Janes/Display/juws2192-jumv.

Khalil, Gazi M. 2001. "Experimental Investigation of Wave Forces on Submerged Horizontal Cylinders." *Indian Journal of Engineering and Material Sciences* 8 (April): 59–65.

Kundu, K. P., and Ira M. Cohen. 2007. *Fluid Mechanics*. 4th ed. Burlington, MA: Academic Press.

Lee, C. M., and J. N. Newman. 1971. "The Vertical Mean Force and Moment of Submerged Bodies Under Waves." *Journal of Ship Research*, September, 231–245.

Lewis, E. V. 1989. *Principles of Naval Architecture Vol 3: Seakeeping and Controllability*. 2nd ed. Jersey City, NJ: Society of Naval Architects and Marine Engineers.

Pinkster, J. A. 1981. "Mean and Low Frequency Wave Forces on Semi-Submersibles." In *13th Annual Offshore Technology Conference*, 9–14. Houston, TX: Offshore Technology Conference.

Senix Corporation. 2016. *ToughSonic Series*. Hinesburg, VT: Senix Corporation.

Tucker, M.J., and E.G. Pitt. 2001. *Waves in Ocean Engineering*. Oxford, UK: Elsevier Science Ltd.

Turner, Travis M., Joseph T. Klamo, and Young W. Kwon. 2018. "Comparison of Wave-Induced Loads on a Near Surface Slender Body From Inviscid Flow Linear Solution and an Experimental Model Test." Forthcoming.

Initial Distribution List

1. Defense Technical Information Center
   Ft. Belvoir, Virginia

2. Dudley Knox Library
   Naval Postgraduate School
   Monterey, California